AWARD NUMBER: W81XWH-14-1-0228

TITLE: Biomechanical Modeling and Measurement of Blast Injury and Hearing Protection Mechanisms

PRINCIPAL INVESTIGATOR: Rong Gan, Ph.D.

CONTRACTING ORGANIZATION: University of Oklahoma
NORMAN, OK 73019

REPORT DATE: OCT 2018

TYPE OF REPORT: Annual

PREPARED FOR: U.S. Army Medical Research and Materiel Command
Fort Detrick, Maryland 21702-5012

DISTRIBUTION STATEMENT: Approved for Public Release;
Distribution Unlimited

REPORT DOCUMENTATION PAGE	*Form Approved* *OMB No. 0704-0188*

1. REPORT DATE OCT 2018	**2. REPORT TYPE** Annual Report	**3. DATES COVERED** 30 Sep 2017 – 29 Sep 2018

4. TITLE AND SUBTITLE Biomechanical Modeling and Measurement of Blast Injury and Hearing Protection Mechanisms	**5a. CONTRACT NUMBER** W81XWH-14-1-0228
	5b. GRANT NUMBER 13063031
	5c. PROGRAM ELEMENT NUMBER
6. AUTHOR(S) Rong Gan, Ph.D. E-Mail: rgan@ou.edu	**5d. PROJECT NUMBER**
	5e. TASK NUMBER
	5f. WORK UNIT NUMBER
7. PERFORMING ORGANIZATION NAME(S) AND ADDRESS(ES) University of Oklahoma, Norman, Oklahoma, 73019	**8. PERFORMING ORGANIZATION REPORT NUMBER**
9. SPONSORING / MONITORING AGENCY NAME(S) AND ADDRESS(ES) U.S. Army Medical Research and Materiel Command Fort Detrick, Maryland 21702-5012	**10. SPONSOR/MONITOR'S ACRONYM(S)**
	11. SPONSOR/MONITOR'S REPORT NUMBER(S)

12. DISTRIBUTION / AVAILABILITY STATEMENT

Approved for Public Release; Distribution Unlimited

13. SUPPLEMENTARY NOTES

14. ABSTRACT

Objectives of the project are to determine middle ear protective mechanisms and develop the finite element (FE) model of the human ear for simulating blast injury and assisting design/evaluation of HPDs. There are three aims: quantify middle ear injury in relation to blast overpressure (BOP) level and wave direction using cadaver ears; identify middle ear protection mechanisms and hearing damages in animals exposed to blast and measuring mechanical properties of ear tissues after exposure; develop FE model of human ear to predict BOP transmission through the ear and prevention mechanisms of acoustic injury for HPDs. Major findings include: 1) duel laser setup with cadaver ears to monitor tympanic membrane (TM) or HPDs (earplugs) movements during blast exposure; 2) identified hearing damage and cochlear injury caused by repetitive blast exposures at low BOP or single blast at high BOP level (mild or moderate TBI) in animals; 3) hearing and cochlear damages measured in protected ears with earplugs during blast exposure; 4) 3D FE model of the entire ear for modeling blast waves transmitted from the ear canal to cochlea; 5) 3D printed human temporal bone/ear and its application for HPDs evaluation. Results demonstrate biomechanical responses of the ear to blast overpressure and the limited protective mechanism of HPDs for blast exposure.

15. SUBJECT TERMS

Blast overpressure transmission, ear biomechanics, tympanic membrane rupture, middle ear muscle reflex, finite element modeling of human ear, hearing protection devices

16. SECURITY CLASSIFICATION OF:			**17. LIMITATION OF ABSTRACT**	**18. NUMBER OF PAGES**	**19a. NAME OF RESPONSIBLE PERSON** USAMRMC
a. REPORT Unclassified	**b. ABSTRACT** Unclassified	**c. THIS PAGE** Unclassified	Unclassified	95	**19b. TELEPHONE NUMBER** *(include area code)*

Table of Contents

Page

1. INTRODUCTION

The objectives of this research project are to determine middle ear protective mechanisms in the conductive path of impulse noise or blast wave into cochlea and to develop the finite element model of the human ear for simulating blast injury and assisting the design and evaluation of personal hearing protection devices (HPDs). To our knowledge this state-of-the-art approach has not been experimentally applied to evaluating the mechanical basis for middle and inner ear damage relevant to high intensity sound or blast exposure. Our **long-term goal** is to understand middle ear biomechanics in response to blast overpressure and impulse noise and to provide the prevention mechanism of acoustic injury for development of effective personal HPDs. To reach the objectives and long-term goal, we have a series of tasks under three specific aims to test our **general hypothesis**: the biomechanical response of the middle ear and inner ear (or cochlea) to impulse noise or blast exposure can be characterized in our 3D comprehensive finite element model of the human ear.

2. KEYWORDS

Blast overpressure transmission, ear biomechanics, tympanic membrane rupture, middle ear muscle reflex, finite element modeling of human ear, hearing protection devices

3. ACCOMPLISHMENTS

● What were the major goals of the project?

The project has three specific aims with 7 tasks over 4 years of funding period.
Aim 1: To quantify middle ear injury in relation to blast overpressure level and impulse wave direction using human cadaver ears or temporal bones.
Task 1-1. To identify blast-induced damage of the tympanic membrane and middle ear ossicles when the ear is exposed to different blast overpressure levels at several incident wave directions.
Task 1-2. To characterize the transfer functions of the ear canal and middle ear in response to impulse sound or blast overpressure applied at the ear canal entrance.

Aim 2: To identify middle ear protection mechanisms using the chinchilla model and the dynamic properties of ear tissues.
Task 2-1. To detect the middle ear muscle reflex in awake chinchillas during the blast exposure.
Task 2-2. To identify changes of mechanical properties of middle ear tissues after high impulse noise/blast exposure in human temporal bones.

Aim 3: To continue the development of our 3-dimensional (3D) finite element (FE) model of the human ear with militarily relevant applications.
Task 3-1. To improve the current 3D FE model of the human ear by including middle ear nonlinearities.
Task 3-2. To develop the active FE model of the ear associated with middle ear muscle functions.

Task 3-3. To provide prevention mechanisms of acoustic injury for personal hearing protection devices (HPDs, passive and active) by using our 3D FE model of the human ear.

● **What was accomplished under these goals?**

Key Research Accomplishments:

Aim 1:
♦ Development of new methodology of using dual laser Doppler vibrometers (LDVs) to measure the movement of tympanic membrane (TM) induced by blast exposure
♦ Using the TM motion measurements to validate the 3D finite element (FE) model of the human ear in response to blast overpressure (BOP)
♦ Characterization of the TM surface motion change after blast exposure using experimental measurement and FE simulation

Aim 2:
♦ Measurement of hearing damage induced by repetitive blast exposure in chinchilla model as the changes of hearing threshold (e.g., auditory brainstem response (ABR)), and cochlear function (e.g., distortion product otoacoustic emission (DPOAE))
♦ Effects of number of blasts and the intensity level of BOP on hearing damage over the time course after multiple blast exposures
♦ Detecting damages in central auditory system after blast exposure with immunohistochemistry and immunofluorescence techniques
♦ SEM images of chinchilla cochlear hair cells before and after blast exposure to determine hair cell damage in relation to BOP level
♦ Initiative chinchilla helmet study to separate the hearing damage in peripheral auditory system (PAS) and central auditory system (CAS)
♦ Measurement of TM mechanical properties with biaxial tension test system

Aim 3:
♦ Improving the 3D FE model of the entire ear including the ear canal, middle ear, and cochlea for computational modeling of blast overpressure transmission through the ear
♦ Prediction of injury threshold of the PAS when exposed to blast overpressure using the FE model
♦ Simulation of active middle ear muscle function in the 3D FE model of the human ear
♦ Improving the 3D printed human temporal bone or ossicular chain for function calibration
----

(1) In this 4th year of the project, the <u>major activities</u> under <u>Aim 1</u> include:
1) Conducting data analysis of the completed experiments in human cadaver temporal bones and preparing journal manuscript;
2) Developing new methodology to measure the movement of TM during blast exposure in human cadaver ears;
3) Using the measured TM motion in response to BOP to validate the 3D FE model of the human ear.

The results from those studies are included in a PhD Dissertation (S. Jiang: Mechanical Properties of Human Incudostapedial Joint and Tympanic Membrane in Normal and Blast-damaged Ears. *PhD Dissertation at University of Oklahoma*, May 2018).

A journal paper entitled "Dual-Laser Measurement and Finite Element Modeling of Human Tympanic Membrane Motion under Blast Exposure" was submitted to Hearing Research and is currently under the 2nd review.

The **specific objectives** are: 1) to quantify human ear response to blast overpressure as the blast induced TM motion with the BOP transmission through the ear; 2) to develop new techniques for measuring blast pressure induced movement of the TM and determining the TM tissue damage in relation to TM movement and BOP level.

(1-1) Movement of tympanic membrane during blast exposure – transfer function of the middle ear

Figure 1 shows the schematic and real pictures of experimental setup with two laser Doppler vibrometers: LDV1 and scanning LDV2, aiming at the head block and the TM, respectively. The laser beams are transmitted through a window onto the targets inside the blast test chamber. Vibration of the head block measured by LDV1 serves as the baseline reference and the TM vibration at the umbo measured by LDV2 includes both the TM movement and the head block movement. The P0 and P1 sensors record the BOP at the entrance of the ear canal (outside of the ear) and the pressure near the TM in the ear canal, respectively. The blast wave direction is along the front of the face (e.g. the front setup). The BOP or P0 pressure level is designed to be around 34 kPa or 5 psi.

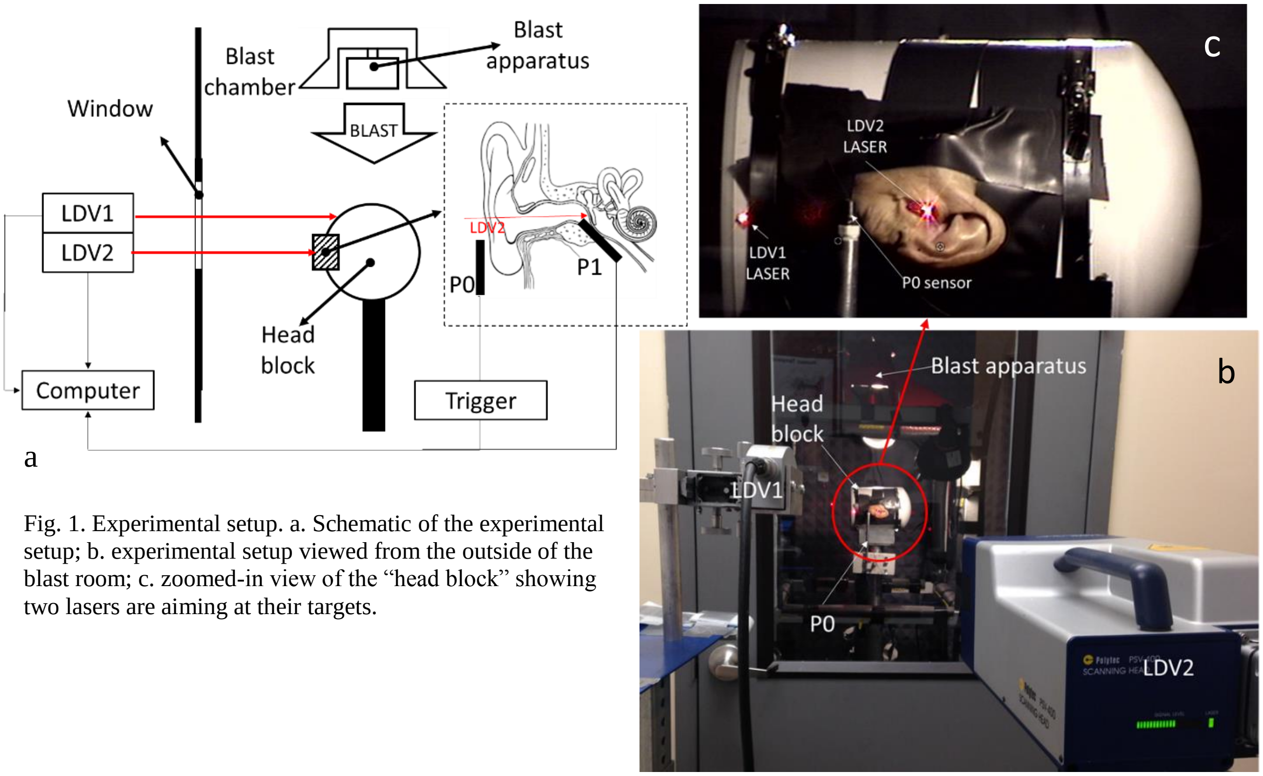

Fig. 1. Experimental setup. a. Schematic of the experimental setup; b. experimental setup viewed from the outside of the blast room; c. zoomed-in view of the "head block" showing two lasers are aiming at their targets.

We have used 5 human temporal bones (TBs) to characterize the movement of the TM when the ear was exposed to blast. The recorded waveforms of pressure (P0 and P1) and velocity (TM and head block) from sample #5 are shown in Figs. 2A and 2B. The red P1 curve shows a higher peak pressure level of 69 kPa (10 psi). The P1 peak value is higher than P0 which demonstrates the amplification function of the ear canal. Both P0 and P1 are attenuated quickly (within 1 ms). P1 curve shows more high-frequency fluctuations comparing to the P0 curve.

Figure 2B shows the velocity data measured from the LDV1 and LDV2. Negative values in velocity curves indicate the TM velocity is in the direction into the middle ear cavity. It is clearly observed that the movement of the TM is far more significant than the movement of the head block in the direction perpendicular to the TM annulus.

The velocity obtained after subtracting the head block vibration is shown in Fig. 2C. The TM velocity does not reach its maximum value at the very beginning, but at the second cycle after the blast. The displacement of TM calculated by integrating the velocity over time is plotted in the Fig. 2D. The displacement curve indicates that the TM moves into the middle ear cavity at the beginning in response to the blast overpressure, then vibrates at an amplitude of 0.4 mm for two cycles and the amplitude diminishes after 1 ms.

The peak pressure amplitude of P0 and P1 are recorded as the input (Fig. 2A). The maximum values of the peak to peak velocity and displacement are recorded as the TM's response (Figs. 2C and 2D). The results of five samples are listed in Table 1. To evaluate the function of the ear under blast overpressure, the displacement is normalized by the input peak pressure P0. Therefore, it suggests that at a P0 level of 34.3 ± 5.2 kPa, the BOP results in a P1 of 61.1 ± 23.0 kPa, a ΔV of 12.62 ± 3.63 m/s and a ΔD of 0.78 ± 0.26 mm which equals to a normalized displacement of 22.9 ± 6.6 μm/kPa.

Table 1. Experimental results obtained from 5 cadaver ears with two LDVs to measure TM movement in response to BOP.

Sample number	P0 (kPa)	P1 (kPa)	ΔV (m/s)	ΔD(mm)	ΔD/P0 (μm/kPa)
#1	31.0	35.9	8.44	0.55	17.6
#2	31.0	96.5	9.32	0.73	23.6
#3	40.0	53.1	13.20	0.59	14.8
#4	40.0	51.0	15.81	1.20	30.0
#5	30.0	69.0	16.32	0.84	28.4
Mean ± SD	34.3 ± 5.2	61.1 ± 23.0	12.62 ± 3.63	0.78 ± 0.26	22.9 ± 6.6

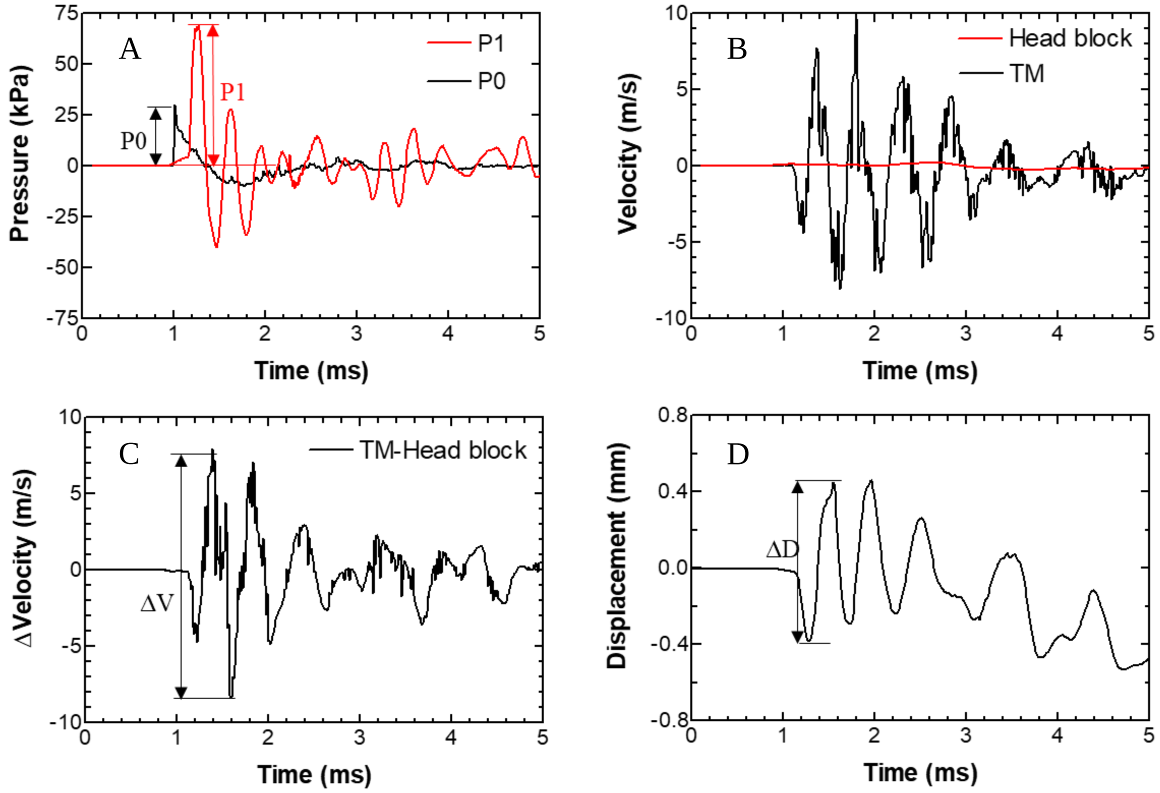

Fig. 2. Waveform results from sample #5: A. Pressure curves; B. raw velocity data from LDV1 and LDV2; C. TM velocity after the subtraction; D. TM displacement.

Considering the fact that the result focuses on the transient response of the TM and the experimental environment involved many possible interferences on the results, the consistency of the experiment was examined by repeating the blast test on the same sample for five times at the same blast level to observe the differences among the output. Figure 3 illustrates the velocity-time curves of the TM measured from LDV2 in TB #1 during 5 repeated tests under the same blast overpressure level. The data recorded from each test were plotted in different color. It could be observed that curves obtained from five individual tests overlapped each other over the entire period of 20 ms with some fluctuations after 5 ms. Prominent positive and negative peaks could be observed at the time of 2 ms which indicated the large velocity initiated by the blast wave reached the TM. The major peaks and valleys generally remained unchanged in 5 tests while small-scale random vibrations were captured in signals after 5 ms. The other 4 TBs exhibited similar repeatable results as shown in Fig. 3, which suggested the experimental setup was reliable.

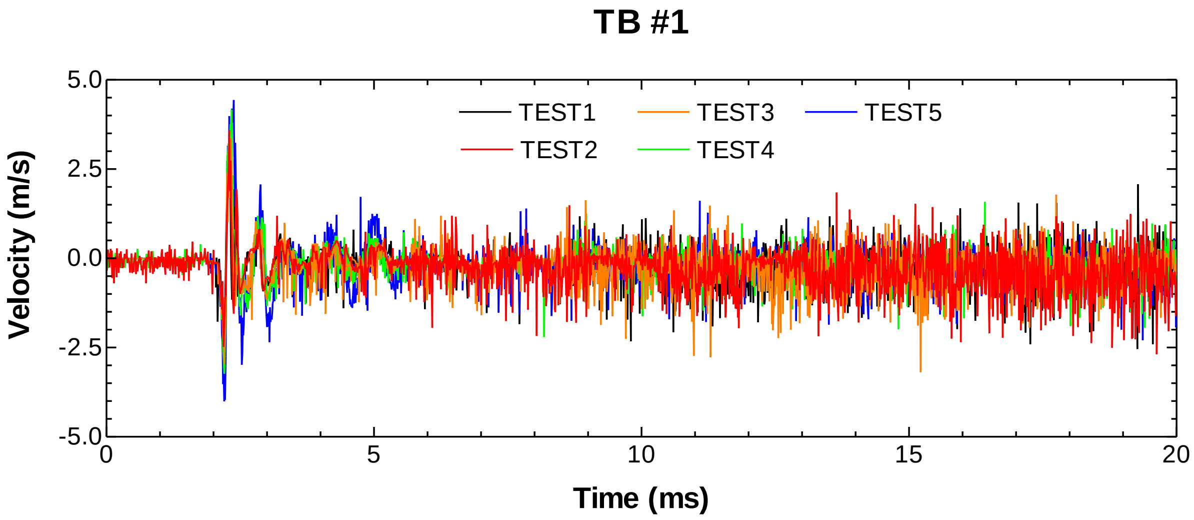

Fig. 3. Velocity-time curves obtained by 5 repeated blast tests on TB Sample #1.

The P0, P1, and displacement signals measured from TB #5 were synchronized and plotted on the same time axis in Fig. 4. Note that the signals were trimmed into 1 ms-long to focus on the duration when the blast overpressure reached and started interacting with the TM. The left y-axis represents pressure while the right y-axis represents displacement. The time point at which P0 reaches its first peak was marked as t_1. Similarly, t_2 was the time point for P1 and t_3 was the time point for the TM displacement. The time delay between P0 and P1 was calculated as t_2-t_1, and the time delay between the first peaks of P1 and displacement was calculated as t_3-t_2.

Figure 4 demonstrates the delayed response of the ear when exposed to blast overpressure. The time delay between the t_1 and t_2 was 0.25 ms, which indicated that the front of the blast overpressure took 0.25 ms to propagate through the ear canal and reach the TM. The time delay between t_2 and t_3 was 0.02 ms, which suggested the TM reached its maximum deformation soon after the maximum pressure applied to its surface. Figure 4 also indicated that the displacement and P1 were in opposite phase at the starting point and then the phase delay quickly decreased within 1 ms.

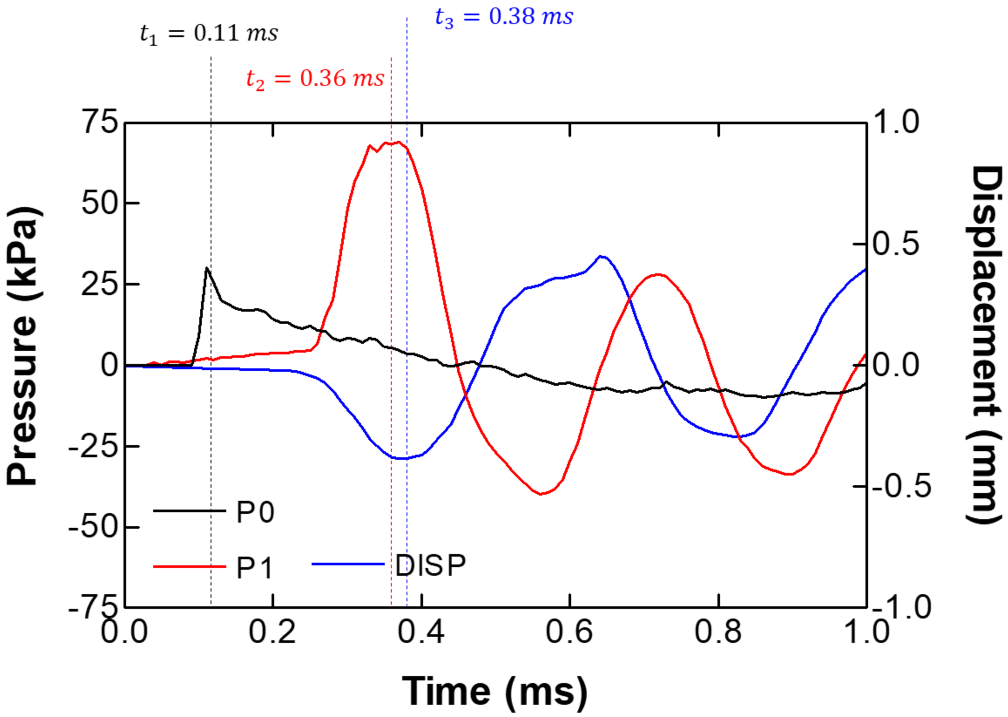

Fig. 4. Time delay between P0, P1 and displacement signals.

Figure 5 illustrates the frequency spectra of velocity and displacement signals obtained from 5 TBs with the mean and SD. The velocity spectra of 5 TBs and their mean curves are plotted in Fig. 5a. Most of the frequency components concentrated between 700 Hz and 3 kHz. A prominent major peak could be observed around 2 kHz and the maximum point on the mean curve was located at 2.15 kHz with a value of 0.21 m/s. A secondary peak appeared around 700 Hz. The velocity amplitudes at the frequencies below 700 Hz or above 3 kHz were generally lower than 0.1m/s. Figure 5b exhibits the frequency spectra of the displacement signals obtained from 5 TBs with their mean values. The displacement amplitude decreased with the frequency exponentially over the entire frequency range from 100 Hz to 50 kHz. The mean values of the displacement were 490 µm at 100 Hz, 44 µm at 1 kHz, 4 µm at 10 kHz, and 0.7 µm at 50 kHz. The shape of the displacement curve of 5 TBs over the frequency range was similar to each other.

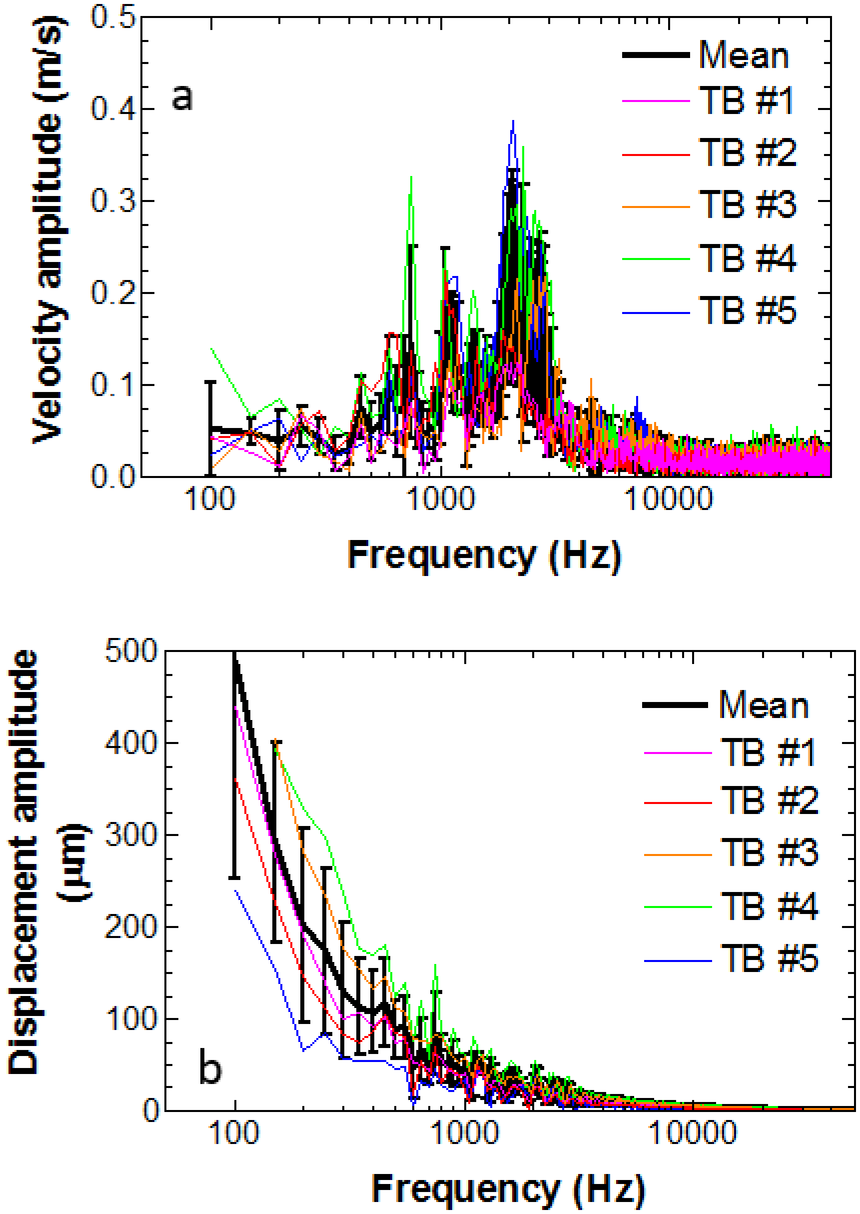

Fig. 5. Frequency domain analysis: (a) Amplitude spectrum of the umbo velocity after subtraction; (b) Amplitude spectrum of the umbo displacement.

The experimental data obtained from human cadaver ears were used to validate the output of the FE model of the human ear in TM movement during blast exposure. Figure 6 shows the FE model developed in this project to simulate BOP transduction through the ear. The P0 waveform in Fig. 4 was applied at the entrance of the ear canal in the model as the input pressure. The P1 and TM displacement signals at the umbo were calculated from the FE model and plotted in Fig. 7. The P1, ΔD (DISP), t2 and t3 values predicted by the model are compared with the experimental results in Table 2.

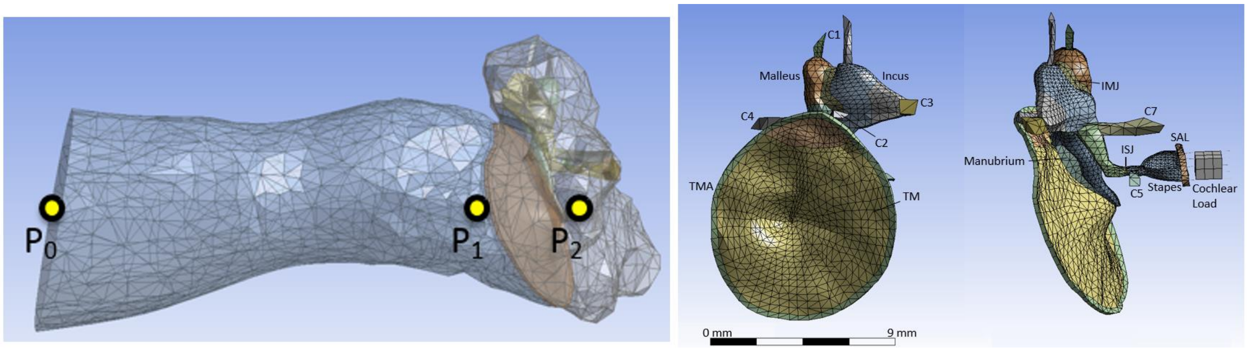

Fig. 6. (Left) FE model of the human ear comprised of the ear canal, TM, middle ear ossicles, and middle ear cavity. The locations for pressure monitoring points are designated as P0, P1, and P2. (Right) Structural mesh of the model, showing the TM, TMA (TM annulus), middle ear ossicles, IMJ, ISJ, suspensory ligaments/muscle tendons (all Cs and SAL), and cochlear load.

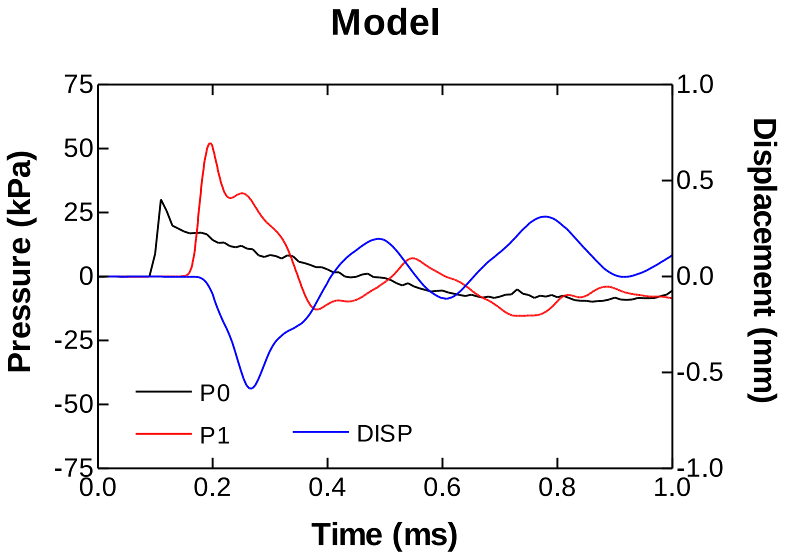

Fig. 7. Time delay between P0, P1 and displacement signals calculated from the FE model.

Table 2. Modeling results compared with the experimental data.

	P0 (kPa)	P1 (kPa)	ΔD (mm)	t_1 (ms)	t_2 (ms)	t_3 (ms)
Experiment	29.7	69.0	0.84	0.11	0.36	0.38
Model	29.7	52.4	0.77	0.11	0.20	0.27

The P1 predicted by the model is lower than the experimental data, but the ΔD is very close to that obtained from the experiments. The model-predicted time delay between the P1 and P0 (e.g. t2-t1) is shorter, but the delay between the displacement and P1 (e.g. t3-t2) is longer than the experimental data. Comparing the waveform in Figs. 4 and 7, the order and the peak values of FE model-derived P1 and displacement curves agree with the experimental data. However, the experimental cures are smoother than the model-predicted curves.

In conclusions, it is the first time that the movement of the TM under blast overpressure measured by the dual-laser setup. The method developed in this study provides a new methodology to conduct quantitative characterization on the response of the ear under blast, which extend the LDV measurement for sound transmission in the ear to a new area, the time domain measurement on the transient response of the ear. The dual-laser measurement based on the relative motion to eliminate the vibration of the head block from the movement of the TM provides a novel idea to isolate the key data from the extensive and complicated interferences in blast-related research.

Results obtained from the dual-laser measurements provide a direct description of the impact of the blast overpressure on the ear. Movement of the TM represents the transfer function of the middle ear and reflects the input into the cochlea, which can be used as the evidence to assess the conductive hearing loss induced by blast exposure. The transient response of the TM within a few milliseconds after blast helps us to understand the mechanism of the TM injury formation, such as rupture or microstructural damage in the TM. Finally, the experimentally-measured TM movement is a critical parameter to validate the FE model for blast-related analysis. Quantitative data such as P1, ΔD, t2, and t3 measured by the experiments are useful for calibration of the FE model.

(1-2) Data analysis on TM surface motion after blast exposure measured by scanning LDV (SLDV)

The surface motion of the human TM before and after blast exposure was measured by SLDV in cadaver ears or temporal bones. The locations and frequency range where a major maximum displacement appeared on the TM surface were identified. However, the results were made based on observations of the displacement distribution on the TM surface. A more quantitative analysis is necessary to investigate the location and frequency of the damage. Therefore, the TM was divided into four quadrants (Q1-Q4) as shown in Fig. 8. The center of each quadrant was marked and the displacement-frequency curves at the umbo and 4 quadrants were selected.

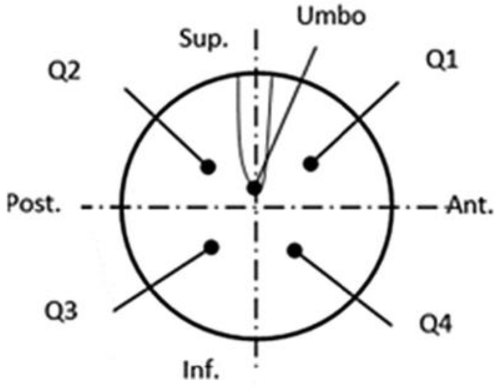

Fig. 8. Schematic for the TM with locations of the umbo and the centers of four quadrants: Q1-Q4.

We have introduced "transmissibility" which is a damage detection algorithm used in structural health monitoring systems. It is a passive technique because no information about the load function is required (Kess & Adams, 2007). The transmissibility is defined as the ratio of two frequency response functions, H_{qk} and H_{uk}, given the same sound stimuli and two output locations: the center of each quadrant and the umbo. Given the equation below, the ratio ($TR_{qu(k)}$) is equivalent to the ratio of two responses measurements, X_q and X_u, the displacement in the frequency domain,

$$TR_{qu(k)}(\omega) = \frac{H_{qk}(\omega)}{H_{uk}(\omega)} = \frac{X_q(\omega)/F_k(\omega)}{X_u(\omega)/F_k(\omega)} = \frac{X_q(\omega)}{X_u(\omega)} \qquad (1)$$

where q is the center of the quadrant, u is the umbo, ω is the frequency and k is the degree-of-freedom. If the damage exists along the path connecting these two points (q and u), the value of the transmissibility will change. Therefore, we normalized the displacement by the sound stimulus level (μm/Pa) and used as the responses measurements. The responses at the centers of four quadrants were divided by the responses at the umbo to calculate the transmissibility. The results of transmissibility from tested two temporal bones are shown in Figs. 9 and 10. The black curves represent the results obtained from the pre-exposure, normal temporal bones and the red curves are the results from temporal bones after blast exposure.

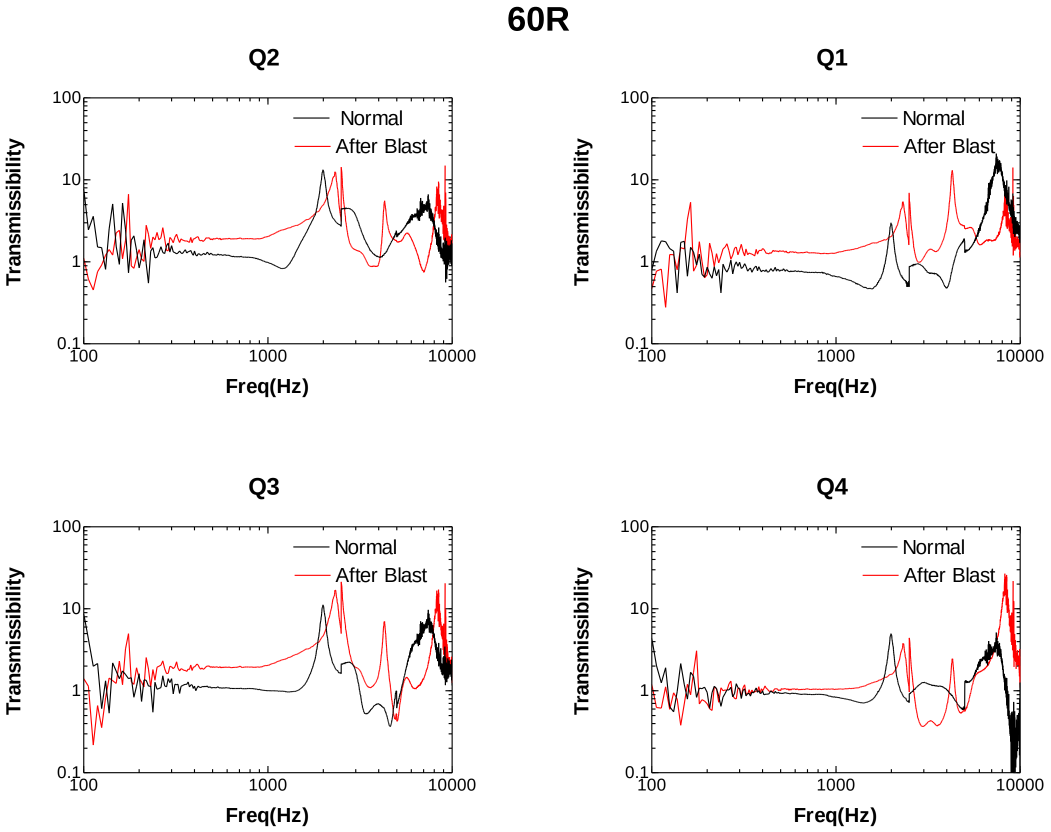

Fig. 9. Comparison of the transmissibility-frequency curves at the centers of four quadrants in the TM (TB 60R) post blast with the normal/pre-blast.

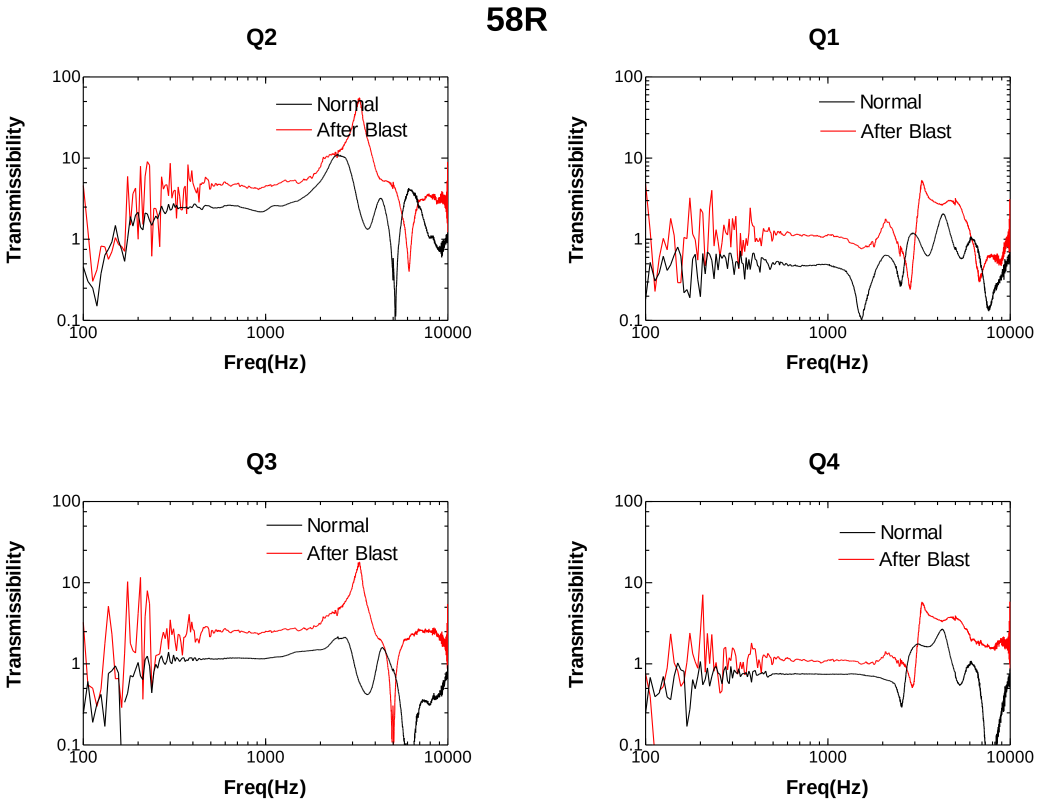

Fig. 10. Comparison of the transmissibility-frequency curves at the centers of four quadrants in the TM (TB 58R) post blast with the normal/pre-blast.

Sample TB 60R exhibits difference in transmissibility in 4 quadrants. Both curves exhibit a flat region at the frequency range between 0.5 to 1 kHz at values close to 1. Then, there is a major peak around 2k Hz and a few fluctuations at higher frequencies. The shape of the curves before and after the blast exposure is similar at 4 quadrants, but the values after blast is higher than the normal in Q1, Q2, and Q3. The curves in Q4 are close to each other. The curve shapes obtained from TB 58R provide the same information as TB 60R. The least difference also appears in Q4. It is found that the post-blast curves generally show higher transmissibility than the normal curves with similar shape over the frequency range. The difference mostly exhibits at the frequency range of 1-3 kHz. Q4 shows the least difference while Q3 shows the most difference in all samples. In conclusions, the frequency range in which the transmissibility shows major difference (1-3 kHz) between the normal and blasted TMs is consistent with the range which shows the increased maximum displacement observed in both experiment and modeling results.

(2) In this 4th year of the project, the <u>major activities</u> under <u>Aim 2</u> include:

1) Determining the hearing damage (ABR threshold and DPOAE level changes) and CAS damage (immunohistochemistry study) in chinchillas after repetitive 2 blasts and 3 blasts on Day 1 at the mild BOP level or mild TBI – G2 group animals both ears inserted with foam earplugs and observed for 7 days (2 blast animals) and 14 days (3 blast animals);
2) Determining the hearing damage (ABR threshold and DPOAE level changes) in chinchillas after repetitive 3 blasts on Day 1 at the low BOP (below mTBI) level – G1 group animals observed for 7 days;
3) Studies on SEM images of chinchilla cochlear hair cells and stereocilia before and after blast exposure;
4) Preliminary study on chinchillas with 3D printed helmet to examine the blast exposure induced hearing damage either from the PAS mechanical damage or the CAS damage.

The **<u>specific objectives</u>** are: 1) to determine hearing damage in relation to numbers of blast exposure and the BOP level over the time course; 2) to evaluate the protective mechanism of hearing protection devices (HPDs, e.g. earplugs) for multiple exposures at low BOP or mild BOP; 3) to assess the cochlear hair cell damage caused by different BOP levels; 4) to conduct the feasibility study on the hearing damage between the PAS and CAS injuries using the chinchilla helmet study.

(2-1) Hearing damage in relation to number of blast exposure at **G2 mild BOP level**

The animals (n=12) were divided into two groups to expose blast at an average peak pressure of 15-20 psi or 103-138 kPa. The first group were exposed to two consecutive blasts on Day 0, named as 2-Blast group. The second group were exposed to three consecutive blasts on Day 0, named as 3-Blast group. The hearing function of the animals was measured before and after exposures using ABR and DPOAE. The 2-Blast group's hearing function was tested the day of the blast (before and after the exposure) or Day 0 (D0), then Day 1, 4, and 7 (D1, D4, and D7). The 3-Blast group's hearing function was tested on D0, D4, D7, and D14. In all tests, both ears were plugged with foam earplugs to prevent the tympanic membrane from rupturing.

Figure 11 shows the recorded BOP waveforms. The ABR results are summarized in Fig. 12. The left panel are the hearing results for the 2-Blast group. There is a huge increase of post-blast on D0, particularly at higher frequencies (f>2 kHz). Following the greatest threshold increase at the post-blast (D0), the ABR threshold shift decreased on each tested day. On D7, the threshold was almost the same as the pre-blast on D0. The right panel in Fig. 12 are the ABR results for the 3-Blast group. There is a greater increase of post-blast on D0 than that of 2-Blast group. Following the greatest threshold increase at the post-blast on D0, the ABR threshold shift decreased on each tested day, but it was almost stable after the large decrease on D4. After the large shift decrease on D4, each subsequent shift decreases less and there is little difference in the threshold shifts between D4, D7, and D14. On Day14, there were an ABR threshold shift of 20 dB at 500 Hz and 40 dB shifts at 8 kHz in this group of animals.

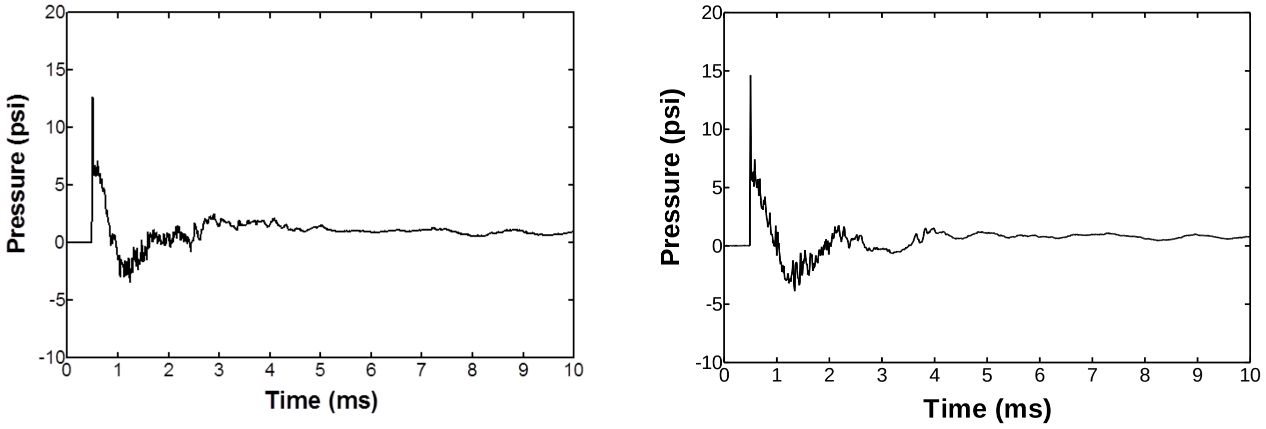

Fig. 11A. A recorded P0 waveform from one animal test.

(B) The P0 waveform recorded from another animal test.

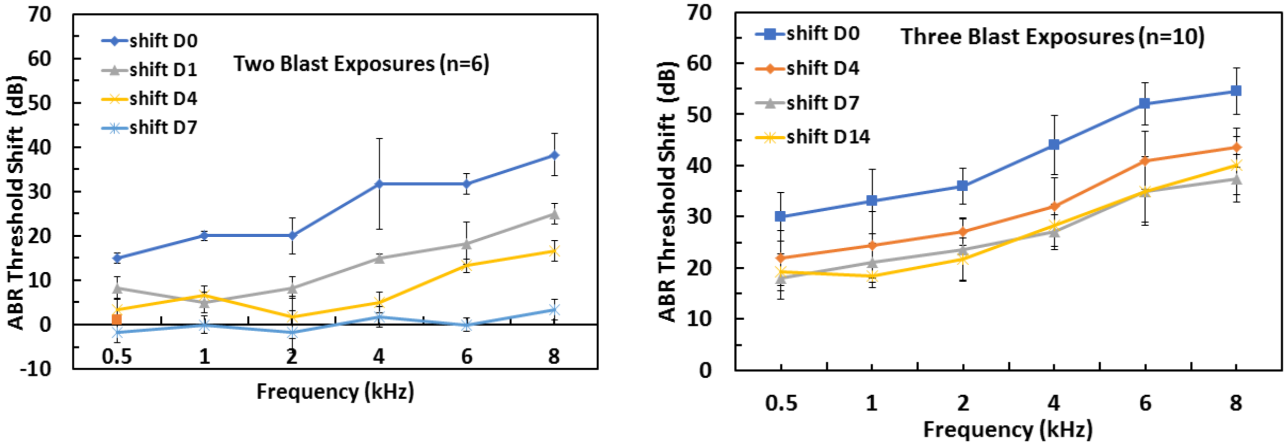

Fig. 12A. Mean and SD of ABR threshold shifts measured from 2-Blast group.

(B) Mean and SD of ABR threshold shifts measured from 3-Blast group.

The DPOAE results are summarized in Fig. 13. The left panel is the DPOAE results for the 2-Blast group and the right panel is for 3-Blast group. After 2 blasts, the DPOAE level was decreased from pre- to post-blast on D0, then the level had a big increase (reduction of shift) on D1 across the frequencies and a continual increase on D4 at high frequencies. On D4 and D7, the DPOAE level came back to the pre-blast on D0. The greatest shift occurs on D0 after blast and an insignificant shift appears for D4 and D7. For 3-Blast group (the right panel), there was no much difference between D4 and D7 or D14, but the DPOAE level shift clearly indicates that the level did not come to the normal after 14 days and there was 14 dB shift at 1 kHz and 28 dB at 11-12 kHz. There was no obvious difference on DPOAE recover between 4D, 7D, and 14D.

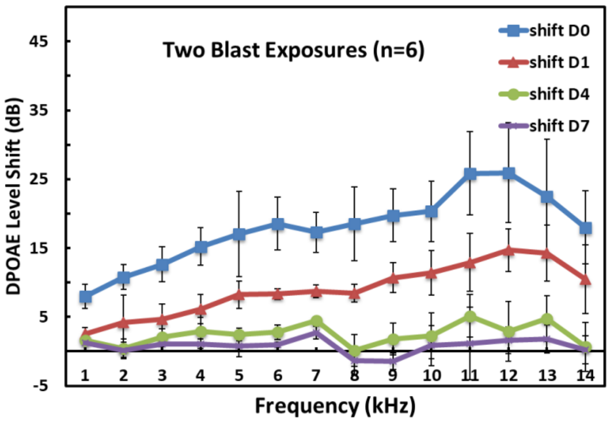

Fig. 13A. Mean and SD of DPOAE level shifts measured from 2-Blast group.

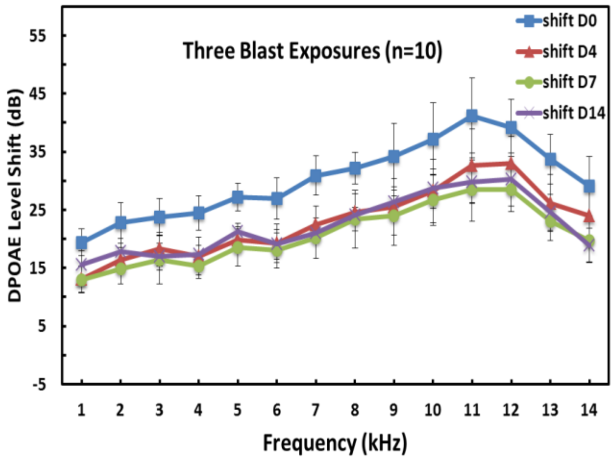

(B) Mean and SD of DPOAE level shifts measured from 3-Blast group.

In addition of hearing function tests, we have initiated some preliminary study on detecting the central auditory system damage in the above two groups of animals (2-Blast and 3-Blast) using biochemistry methodologies, such as the immunohistochemically (IHC) staining and the immunofluorescence staining on chinchilla brain sections.

Figure 14 shows the Hoechst staining in chinchilla auditory cortex in control, 2-Blast, and 3-Blast animals. The apoptosis cells shown in the right-panel of Fig. 14 were on Day 14 after 3 blast exposures on Day 0, compared with the 2-Blast animal on Day 7 – the final day of the experiment and the control animal. Nuclear condensation and/or fragmentation represent cell apoptosis. Arrows marked the apoptotic cells for representing nuclear condensation/fragmentation.

Figure 15 shows the immunofluorescence staining of PI3K protein in chinchilla auditory cortex in control (top three figures), 2-Blast (middle three figures) and 3-Blast animals (bottom three figures). The expression of PI3-kinase (p85α) decreased after three blast exposures comparing with the control and 2-Blast exposure animals in auditory cortex. PI3K/Akt pathway is an antiapoptotic pathway which is important in cell growth, metabolism, survival, and proliferation. Blast-induced PI3K decreasing can result in neuron cell apoptosis.

These preliminary results demonstrate that the auditory cortex neurons are damaged after multiple blast exposures, resulting in neuron cells apoptosis through reducing the expression of PI3K. We will work on more biomarkers of the PI3K/AKT signal pathway in the future study.

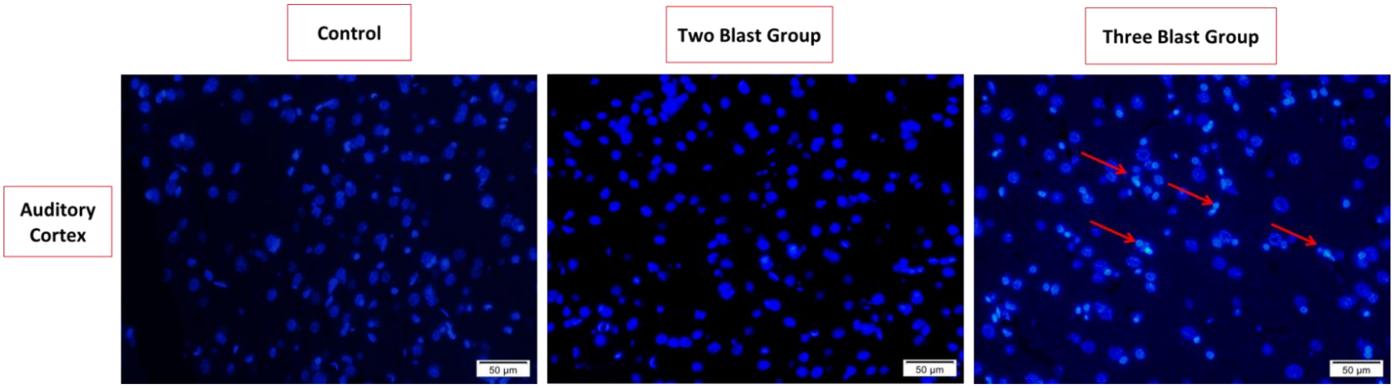

Fig. 14. The Hoechst staining in chinchilla auditory cortex in control (left), 2-Blast (middle) and 3-Blast (right) animals. Images were taken at a magnification of 100×. Arrows marked the apoptotic cells for representing nuclear condensation/fragmentation.

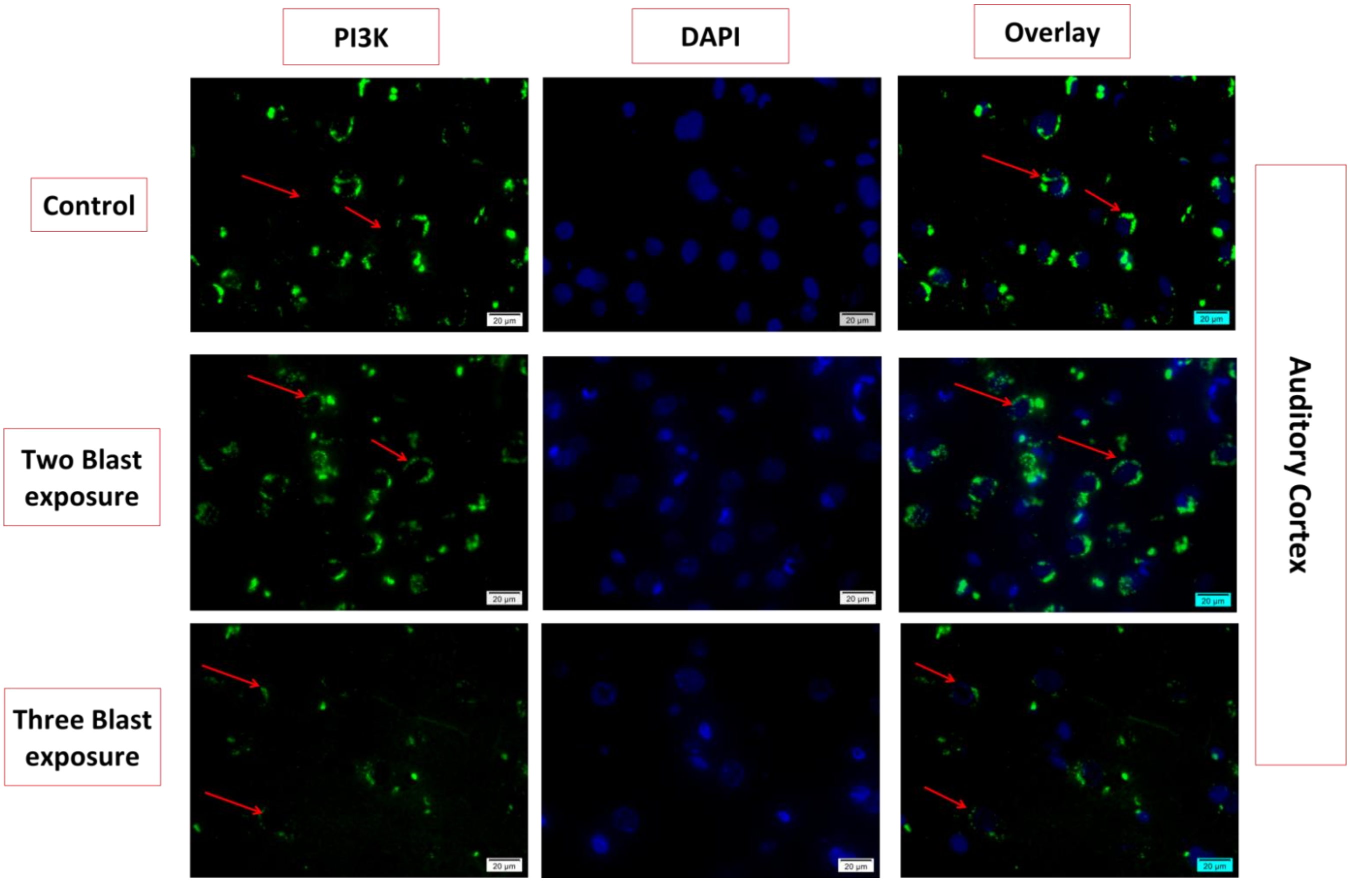

Fig. 15. The immunofluorescence staining of PI3K in chinchilla auditory cortex in control, 2-Blast and 3-Blast animals. The top three figures are from the auditory cortex in control animals; the middle three figures from the auditory cortex in 2-Blast animal on Day 7; the bottom three figures from the auditory cortex in 3-Blast animal on Day 14. Images were taken at a magnification of 400×. Arrows marked the p85α expression in auditory cortex. The nuclear counter stain is DAPI (blue).

(2-2) Hearing damage after repetitive exposure at **G1 low BOP level**

Six chinchillas were used in this study with 3 blasts on Day 1 and observed for 7 days. In 4 animals, the left ear was inserted with an earplug and the right ear was open. In two animals, the both ears were plugged. Animals were blasted three times on Day 1 with 10 minutes interval between blasts at the BOP level of 3-5 psi (21-35 kPa) or below the mild TBI monitored by a pressure sensor (P0) at the entrance of the ear canal. Another sensor was inserted into the ear canal near the tympanic membrane as P1 pressure in the ears with and without earplug. The ABR threshold and DPOAE level of each ear were measured at pre- and post-blast on Day 1 and on Day 4 and Day 7. Figure 16 shows the recorded P0 waveform from two animals.

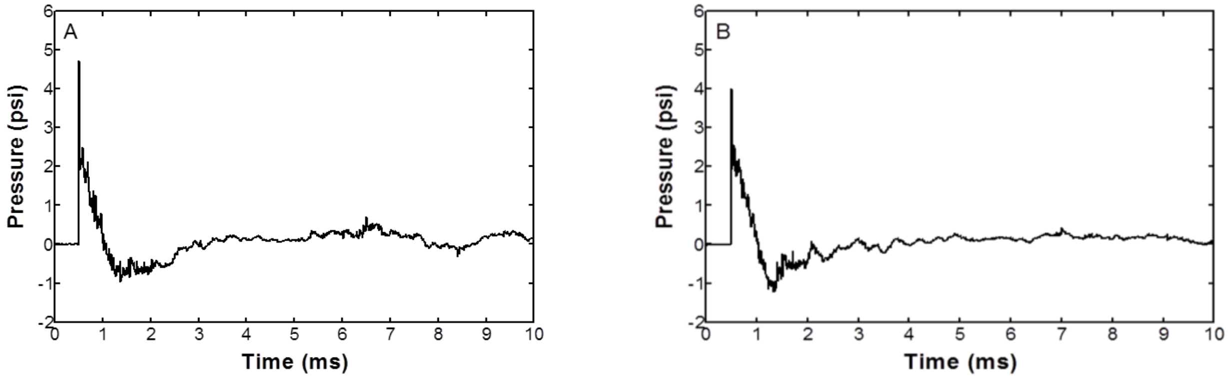

Fig. 16. A recorded P0 waveform from one animal test. (B) The P0 waveform recorded from another animal test.

Figure 17A shows the ABR threshold shift or increase after blast exposure obtained by subtracting the pre-blast threshold from the post-blast threshold in the ears with earplug on Days 1, 4, and 7 (N=4). Figure 17B shows the ABR threshold shift measured from open ears without protection on Days 1, 4, and 7. Day 1 data shows the acute response after multiple blasts with the greatest threshold shift. Day 4 is the shift on the 4th day and Day 7 on the 7th day.

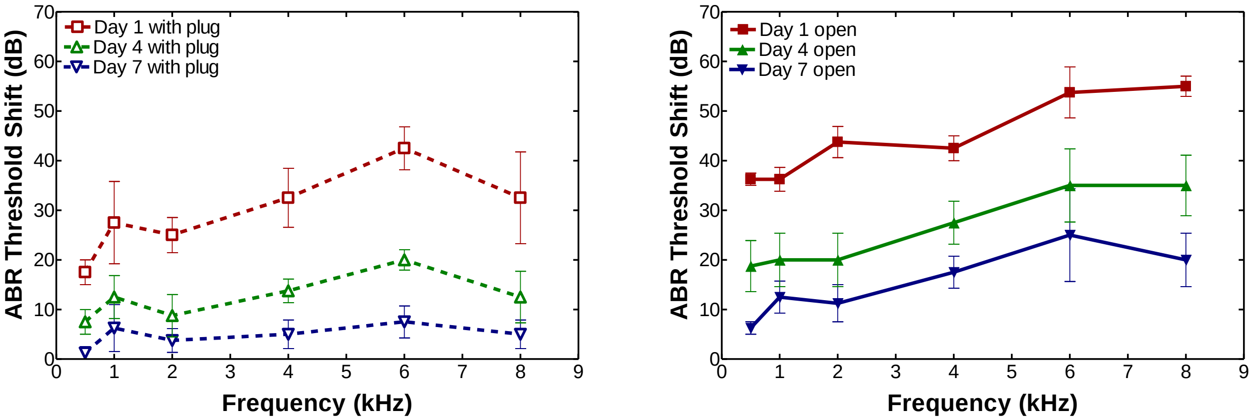

Fig. 17A. Mean and SD of ABR threshold shifts measured from protected ears with earplug (n=4).

(B) Mean and SD of ABR threshold shifts measured from open ears without earplug (n=4).

The results show that hearing damage of ABR threshold shift or increase was observed in both ears, open and protected, after blast exposure on Day 1 in all tested animals, especially at higher frequencies. The ABR threshold shift was greater for open ears than the protected ears: 35-50 dB vs 20-40 dB after 3 blasts. The most protection from the earplug was found at low frequencies (f<4 kHz). After 7 days, the protected ears regained most of their hearing function, shown in the decrease of ABR shift. However, after 7 days in the open ears, the ABR threshold was still elevated by 7-20 dB from 1 to 8 kHz, which indicated the possible permanent hearing damage.

Figure 18A displays the combined ABR threshold shift data measured from the open ears (solid lines) and the protected ears (broken lines), as a comparison of hearing damages in the open and protected ears on Day 1, Day 4, and Day 7. The open ears show a much higher threshold shift on every measured day over all frequencies. The open ears of Day 7 have a higher threshold shift than the Day 4 threshold shift in protected ears. The greatest threshold shift on Day 7 in the open ears occurs at 6 kHz.

The DPOAE results obtained in protected ears are summarized in Fig. 18B. The reduction or shift of DPOAE value measured in post-blast ear compared to the pre-blast ear represents the cochlear outer hair cell function damage after blast exposure. As shown in Fig. 18B, there was a huge DPOAE shift or reduction on Day 1, representing the acute cochlear damage, especially at higher frequencies (f>6 kHz). The most protection with the earplug was found at low frequencies (f<4 kHz). After 7 days, the protected ears regained most of their hearing function, shown in both the DPOAE shift and ABR shift.

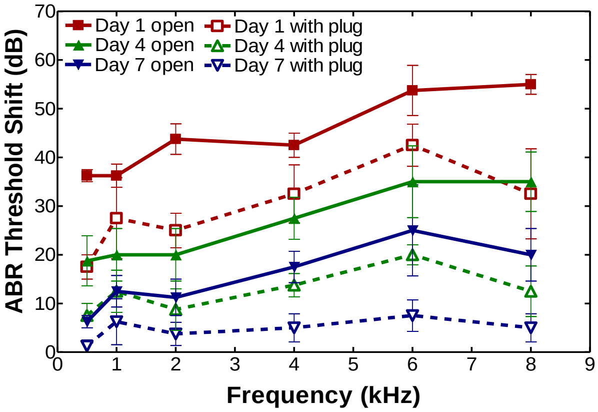

Fig. 18A. Comparison of ABR threshold shifts between open and plugged ears on Days 1, 4, and 7.

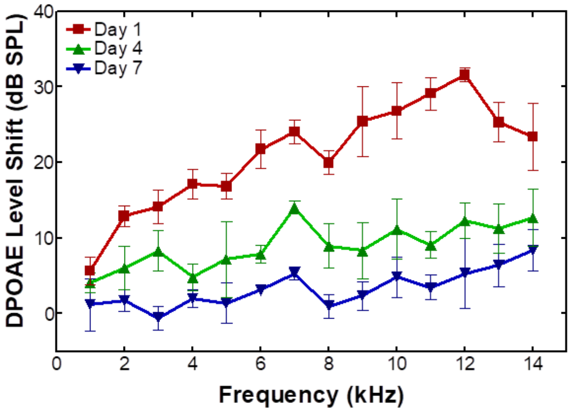

(B) Comparison of DPOAE level shifts after blast on Days 1, 4 and 7 in protected ears.

In summary, hearing damage (both ABR and DEOAE) was induced in both ears after blast exposure on Day 1 in all tested animals, especially at higher frequencies. After 7 days, the protected ears regained most of their hearing function, shown in both the DPOAE shift and ABR shift. After 7 days in the open ears, the ABR threshold was still elevated by 7-20 dB from 1 to 8 kHz, which may indicate the permanent hearing damage. However, more animal studies should be conducted in future work along two directions: 1) longer time course to explore progressive hearing damage after blast exposures, for example, 3 blasts for every two weeks over 6 or 10 weeks of observation; 2) measuring the blast pressure transmission in ears with and without earplug to determine the earplug protection function in attenuation of blast pressure.

(2-3) SEM imaging of chinchilla cochlear hair cells and stereocilia damages after blast exposure

Study #1 – Presented at 2018 ARO meeting:

Some preliminary results from this project were presented with a poster at the ARO 41st Annual Midwinter Meeting in February 2018. Figures 19 and 20 below show some sample SEM images of chinchilla cochlear hair cells presented at the conference. Here is a brief description of the methods used and the conclusions from the study:

Methods:

● Seven chinchillas in two groups were included in this study and were exposed to multiple blast exposures at levels ranging from 15 – 20 psi (see Section 2-1, G2 BOP level). One group was exposed to two blasts while the other group was exposed to three, and the animals were allowed to rest for 7 and 14 days, respectively.

● Hearing function tests were performed before and after blast exposure and at regular intervals during the resting period. The animals were euthanized after the last hearing function test.

● The cochlea was harvested immediately after euthanizing and were fixated overnight in 4% paraformaldehyde in 0.1M PBS containing 5% sucrose. Standard SEM preparation techniques were performed thereafter.

● The samples were imaged using scanning election microscopes (JEOL 840a and Zeiss NEON).

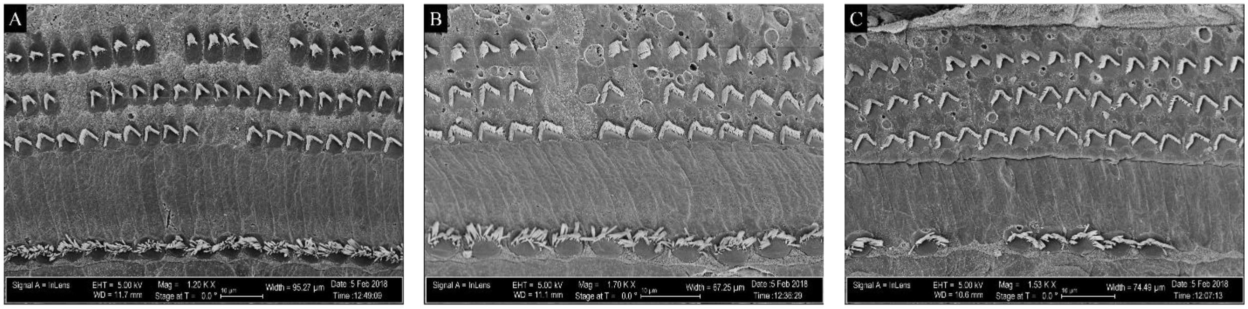

Fig. 19. SEM images of outer and inner hair cells 7 days after being exposed to 2 blasts. (A) Apical turn (~0.5 kHz), (B) middle turn (~4 kHz), and (C) basal turn (~6 kHz). (#17-5-6R)

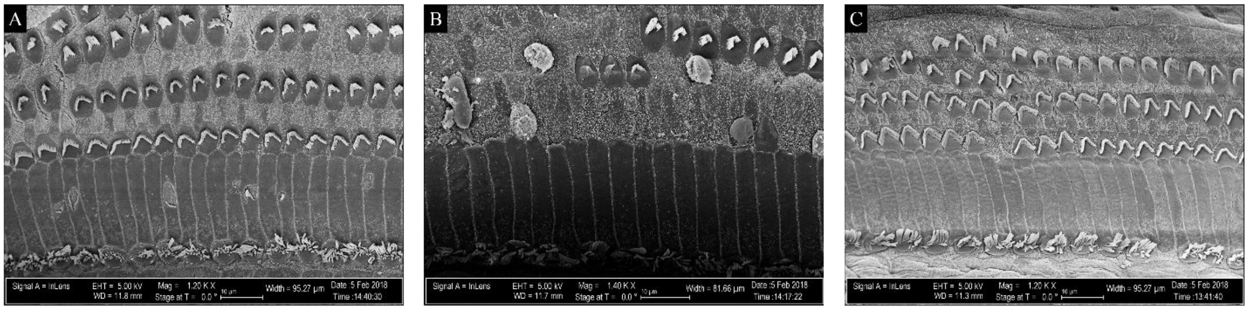

Fig. 20. SEM images of outer and inner hair cells 14 days after being exposed to 3 blasts. (A) Apical turn (~0.5 kHz), (B) middle turn (~4 kHz), and (C) basal turn (~6 kHz). (#17-5-21R)

Conclusions:

- ● BOPs showed to damage hair cells and caused the stereocilia to be disrupted even after 14 days of post-exposure. The damage was more prevalent and longer lasting in the animals that were exposed to 3 blasts when compared to the animals exposed to two.
- ● The loss of hair cells and formation of scars in the Organ of Corti occurred more often in the 3-blast group than in the 2-blast group. The difference was far more prevailing in the middle turn closer to the basal turn (~2 – 8 kHz regions).
- ● Hearing function testing revealed a near full recovery from blast exposure for the 2-blast animal group after 7 days; however, the 3-blast animal group did not fully recover hearing function after 14 days which suggested long-term hearing loss. This agreed with the greater amount of hair cell loss in this group.

Study #2 – Presented at 2018 MEMRO Symposium:

A recent study was conducted to evaluate the effect three consecutive G2 level blasts have on the brain and cochlea. This study included SEM imaging of some of the specimens. The animals were euthanized on the day 1 and day 7 after blast exposure where the previous study looked at cochleae on the 14th day after exposure. Both studies put earplugs in both ears of the test animals. Overall, due to the lack of increased cochlea damage to the test samples from blast exposure, it can be hypothesized that the earplugs were adequate in protecting the cochlea from high pressure fluctuations from the stapes movement. However, there was still recorded hearing loss in the ears with earplugs supporting the conclusion that the blast overpressure exposures can cause hearing loss through other pathways aside from the middle ear transfer function. Also, hair cell loss was not significant in the 7 day time period and was far greater at day 14. This suggests that it takes longer than 7 days after blast exposure for hair cell death to occur. More details on the study and figures can be found below:

Figure 21 (A-F) shows the SEM images of stereocilia from the hair cells in the apical turn (~0.5 kHz) in control and 7--days post blast. The apical region (Figs. 21, A & D) showed little to no signs of hair cell death which was seen throughout most of the cochlea. However, there were some signs of scarring on the Organ of Corti in the middle turn, but only a few cells were found to be lost at 7 days post injury (Figs. 21, B & E). Many areas of the basal turn not adjacent to the oval round window showed little to no disruption to the hair cells based on the SEM images (Figs. 21, C & F).

Despite the Organ of Corti showing signs of being affected by blast overpressures, the current results do not explain the hearing loss over all frequencies as shown in the DPOAE and ABR data. The 7-day SEM images shown in Fig. 21 were from plugged ears, and due to the lack of increased cochlea damage to the test samples from blast exposure, it can be hypothesized that the earplugs were adequate in protecting the cochlea from high pressure fluctuations from the stapes movement. However, there was still recorded hearing loss in the ears with earplugs supporting the conclusion that the blast overpressure exposures can cause hearing loss through other pathways aside from the middle ear transfer function. The hearing loss experienced by the chinchillas may be less affected by the disruption of the hair cells' stereocilia and more affected by the physiological response of the hair cells, their afferent nerves, the central auditory system, and the brain. This response may lead to the eventual hair cell death seen in the long term. Cochlear damage and associated post-traumatic hearing loss have also been reported in individuals with mild to moderate TBI. Together our results strongly indicate that blast TBI causes damage to PAS.

Conclusions:

- The preparation of the cochlea for SEM imaging has improved and consequently, the quality of the finished samples has improved. Some of the improvements implemented were improved handling and mounting of samples and the purchase finer dissection and handling tools.
- Glutaraldehyde has been added to the fixative solution to improve the fixation of the sensitive structures, such as the stereocilia. The resulting solution is now 2.5% glutaraldehyde, 2% paraformaldehyde, and 5% sucrose in PBS.
- The method for extracting the basilar membrane has improved. The basilar membrane is now removed in whole from the outer shell of the cochlea after fixation and decalcification. Removing the outer shell before drying reduce the extent of damage from handling. Improvements here are ongoing.
- The improvements have almost increased the consistency of the results to where the images will be able to accurately depict the cochlea's disturbance by the blasts. Improvements to the procedure continue to be implemented.

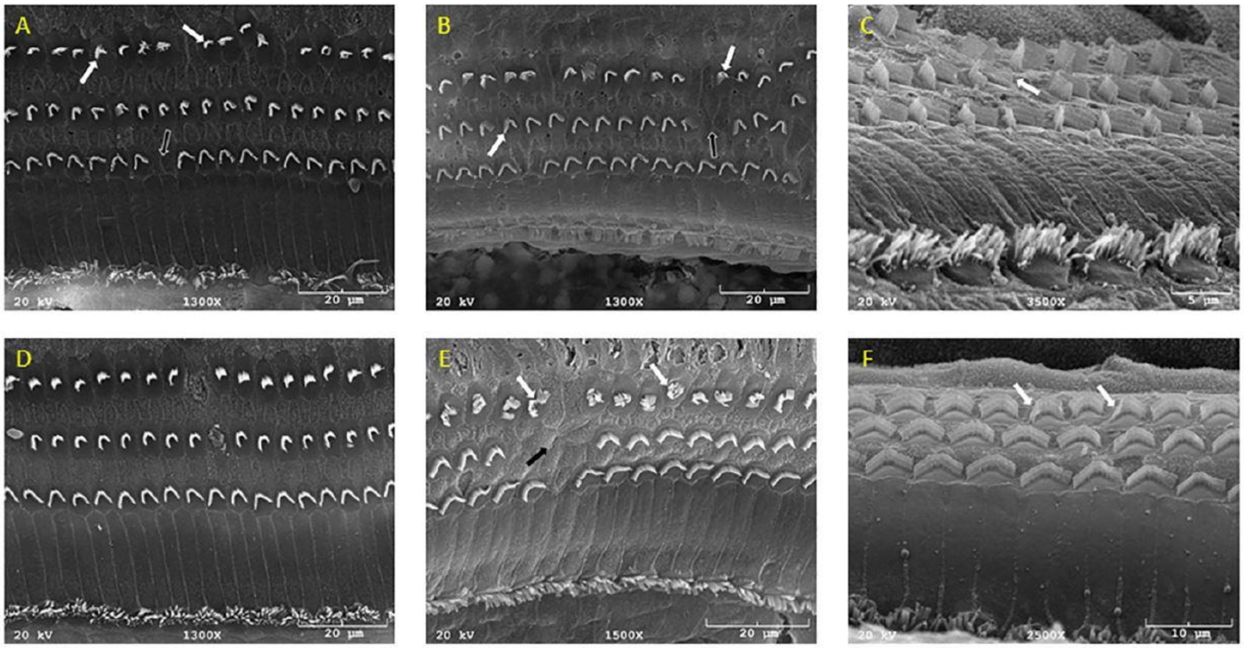

Figure 21. **A&D**: SEM images of the stereocilia from the hair cells in the apical turn (~0.5 kHz) of control (A) and 7 days after blast exposure (D) showing no significant change in the number of hair cells. **B&E**: Stereocilia from the hair cells in middle turn (~4 kHz) of control (B) and 7 days post-blast (E) showing increased scarring on the Organ of Corti in injury groups. **C&F**: Stereocilia from the hair cells in basal turn (~6 kHz) of control (C) and 7 days post-blast (F) showing no change in the number of hair cells. White arrows point out disrupted stereocilia and black arrows show areas of missing outer hair cells and Organ of Corti scarring.

(2-4) Preliminary study on separation of hearing damage from injuries in PAS and CAS under blast exposure

Chinchilla helmet design and animal experiment:

It is well-known that the blast overpressure can cause hearing loss through the damage of the TM, the distortion of the ossicular chain, and the loss of the hair cells. However, the blast can also induce traumatic brain damage. The injury of auditory cortex may directly affect the central auditory function. The significance of the auditory cortex injury in blast-induced hearing loss remains unclear. To isolate the auditory cortex injury from auditory organ (PAS) damage, we proposed to use 3D printed chinchilla "helmet" to reduce the impact to the brain during the blast overpressure test or to measure the effect of the helmet on whether there is a hearing level change with the protection on the skull. As a preliminary study, we designed and tested chinchilla "helmet" to isolate the TBI-induced hearing damage – CAS injury.

Geometry of the chinchilla head was determined from chinchilla cadaver using paraffin and 2-part acrylic to make a mold of the head. After incorporating the geometry and dimensions of the chinchilla mold, a solid model of chinchilla helmet was created in SolidWorks. The design is to fully cover the top of the chinchilla head but allow the ears to be exposed to the blast. Then, the prototype helmet was fabricated using multi-material 3D printing system (Object350, Stratasys) in our lab. The inside of the helmet was filled with a layer (~1 cm thick) of expansion foam to further reduce the impact and to tightly fit the helmet to the surface of chinchilla head. As shown in Fig. 22, the helmet consists of three sections: the main body, the back cover and the face cover. The main body covers the major area of the chinchilla head from forehead to its ears; the back cover shields the back side of the head where the brain is located; the face cover is an extension of the main body to protect the nasal bones and the incisive bones. The whole helmet covers about 75%~80% area of the entire chinchilla head.

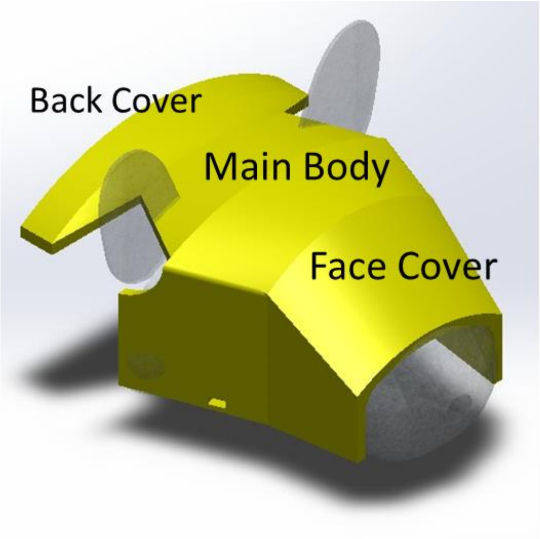

Fig. 22. 3D view of the chinchilla helmet design.

Eleven animals were included in this study with both ears plugged with foam earplugs. Animals were exposed to 3 blasts at the BOP about 15-20 psi, the mild TBI level. Five animals were blast control without helmet and 6 animals were covered by the prototype helmet as shown in Fig. 23. The ABR thresholds of the animal ears were measured before and after 3 blasts on Day 1 and the following Day 4 and Day 7. Figure 24A shows the ABR thresholds measured from animals without helmet and Fig. 24B shows the ABR thresholds form animals with helmet on Days 1, 4, and 7, respectively. The ABR threshold shifts were calculated and plotted in Fig. 25. The ABR threshold shift for the control group (without helmet) is about 10 dB higher than that for the helmeted group at low frequencies and up to 30 dB at high frequencies. On Day 4, the chinchilla of helmeted group recovered hearing function below 2 kHz. On Day 7, the ABR threshold of the helmeted chinchillas averages around 5 dB, reflecting a nearly full recovery of the hearing function. This observation proves that the helmet may not only attenuate the instant devastating effect of the blast overpressure, but also significantly reduce the deeper central auditory neural damage that causes long-term hearing loss.

Fig. 23. View of a chinchilla with the prototype helmet for blast test inside the test chamber. Left: side view; Right: front view.

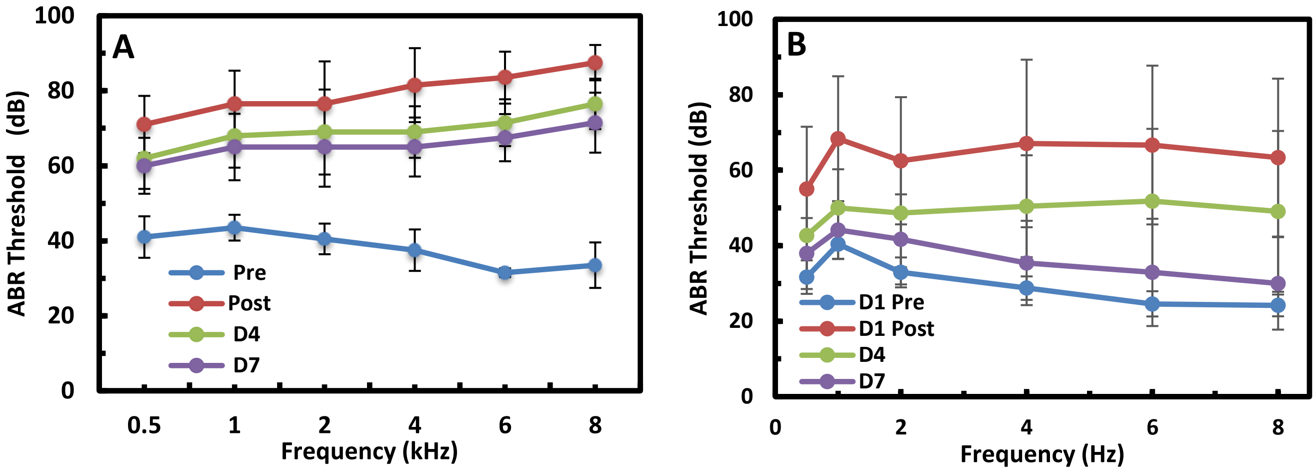

Fig. 24A. ABR thresholds for chinchillas at pre-exposure, post-exposure, Day 4, and Day 7. (A) Animals (n=10 ears) exposed to blasts without helmet protection.

(B) Animals (n=12 ears) exposed to blasts with helmet protection. The error bar shows the standard deviation.

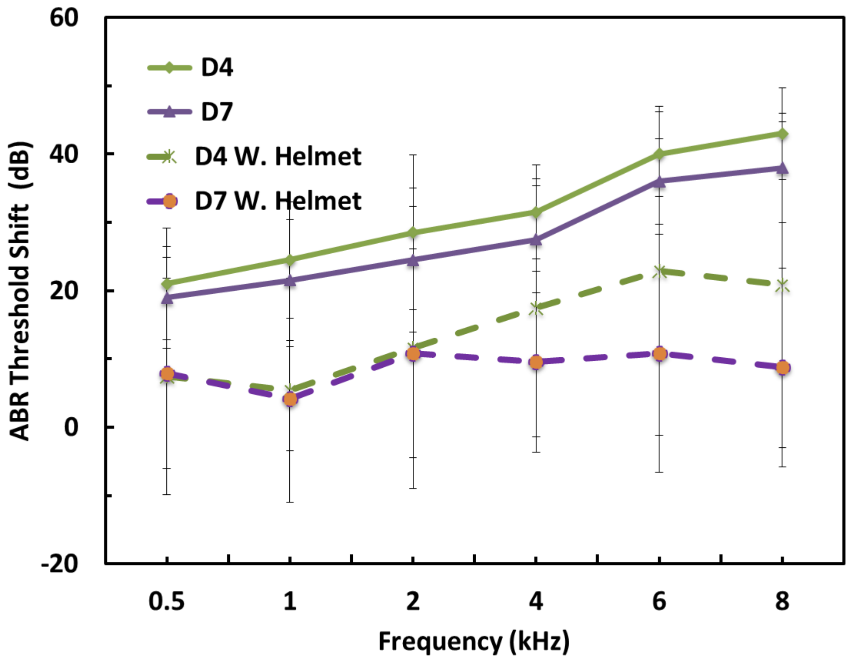

Fig. 25. Comparison of ABR threshold shift between control chinchillas (n=10, solid lines) and helmeted chinchillas (n=12, broken lines). The error bar shows the standard deviation.

Preliminary finite element modeling analysis:

To illustrate the effect of the helmet, a simple 2D FE model of the cerebral structure of the chinchilla skull was established. The model was meshed with 1118 Plane 182 rectangular elements and was separated into four sections: the exterior 3D printed shell of the helmet, the buffering foam, the bony skull and the brain. The outer boundary of the bony skull section was fixed at all degree of freedom, while the other boundary was free of constrain. The material properties of the exterior shell were based on the industrial data reported by Stratasys. The material properties of the skull and the brain were based on data that measured from human. For the foam, since the mechanical properties can vary significantly depending on the curing time, temperature, moisture and many other manufacture factors, thus we used a series of values for the simulation. This can also serve as a guideline for further improving the helmet. However, for the demonstration purpose, only one value was used for the comparison between control and helmeted animals. The model and its boundary condition are shown in Fig. 26 while the mechanical properties are shown in Table 3.

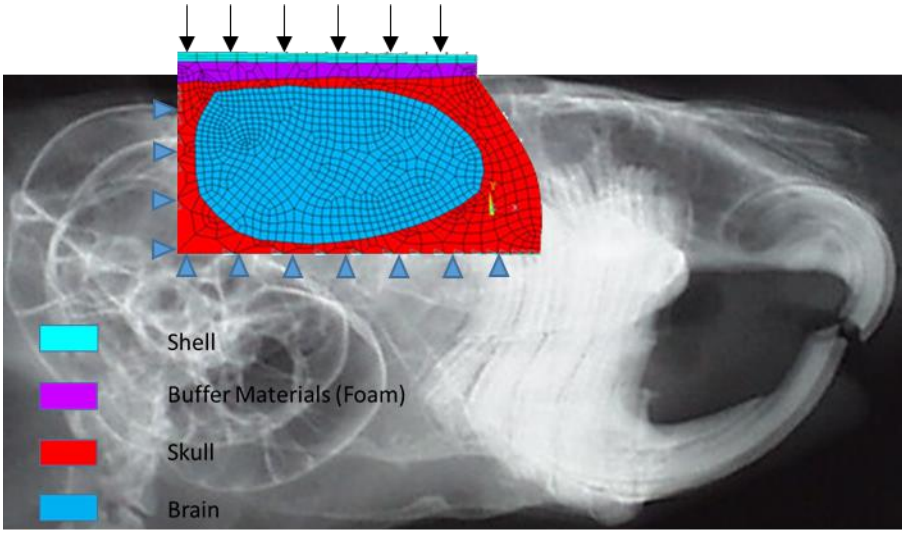

Fig. 26. FE model of chinchilla intraceretal structure and chinchilla helmet.

Table 3. Material properties used in the FE model.

Parts	Model type	Material Properties
Shell	Elastic	E=2500 MPa, µ=0.3
Foam	Hyperelastic (Mooney-Rivlin)	C1=-4.4 MPa, C2=1.5MPa, D=-0.29
Skull	Elastic	E=10 GPa, µ=0.3
Brain	Hyperelastic (Mooney-Rivlin)	C1=240 Pa, C2=342 Pa, D=27

In the FE simulation, the BOP recorded at the ear canal entrance (P0) was used as loading as shown in Fig. 27. The shear stress of the center of the brain section was the output to evaluate the TBI. It is worth to mention that the brain in the real case is composed of grey and white matter. The auditory cortex is actually located at the inferior section of the brain. In our model, the brain is simplified by using average material properties of grey and white matter, thus there is no significant change among locations of the brain.

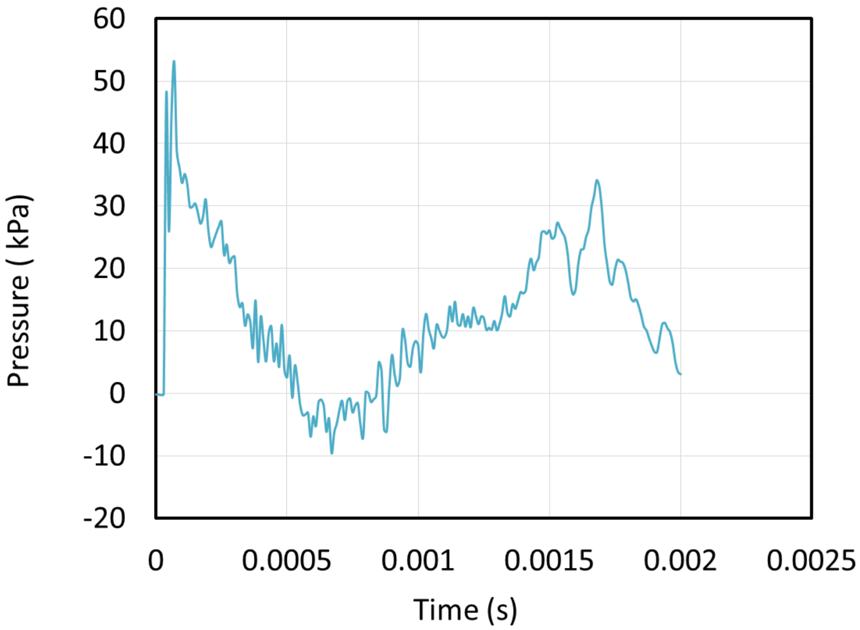

Fig. 27. Measured blast pressure applied on the chinchilla skull and helmet model.

The shear stress in the center of the brain was compared between cases of with helmet and without helmet (Fig. 28). It clearly shows that the helmet reduced the peak of the shear stress by about 60%

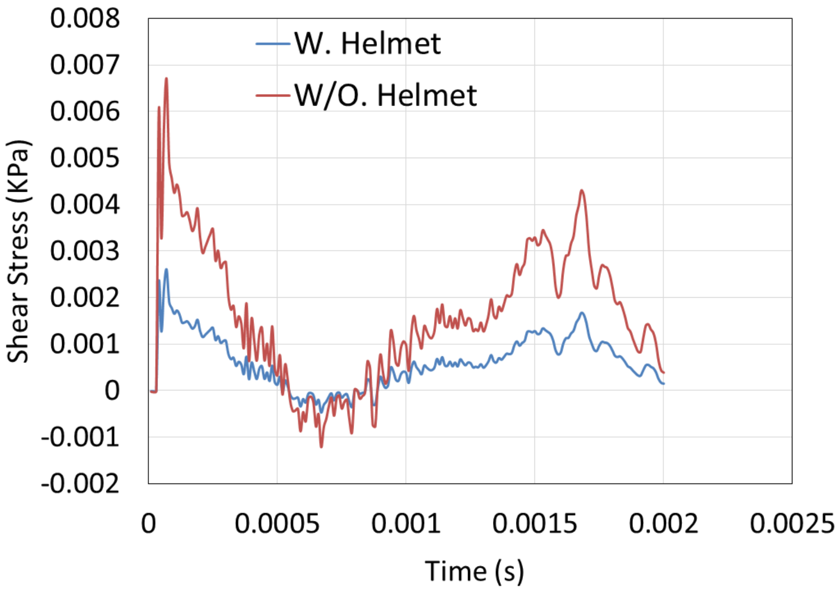

Fig. 28. Comparison of shear stress at the center of the brain derived from the FE model for cases of with helmet and without helmet.

Discussion:

The helmet used in this study is still in the preliminary stage. Although the geometry of the helmet design has been alternated several cycles, there are still many places the helmet design can be improved. For example, the shape of the exterior can be streamlined to reduce the impact of the overpressure and wavy surface might be used to dissipate the blast energy. Multiple layer of buffer material may also improve the protection effect as the result of the dissipation of the energy across their interfaces.

In this study, the ears of the chinchilla were protected with earplugs. Therefore, majority of the damage is presumably from TBI. Our results do prove that the chinchilla helmet, though still in its prototype, demonstrates promising protection of the TBI, especially for that causes long-term hearing loss. However, the deviation of data for the helmeted animal is high. This could stem from the movement of the helmet during blast and the uniform geometry of the helmet for all the animals. These two limitations will be solved in future studies. Lastly, the purpose of the helmet is to isolate the PAS injury from the CAS injury. In the next phrase, ABR will be measured in animals with helmet but without earplug and the animals with earplug but without helmet, which will grant us more comprehensive understanding the injuries from either the PAS or the CAS caused by blast overpressure. Figure 29 illustrates the studies we proposed on chinchillas using the helmet and earplugs to separate the hearing damage from injuries in PAS and CAS under blast exposure.

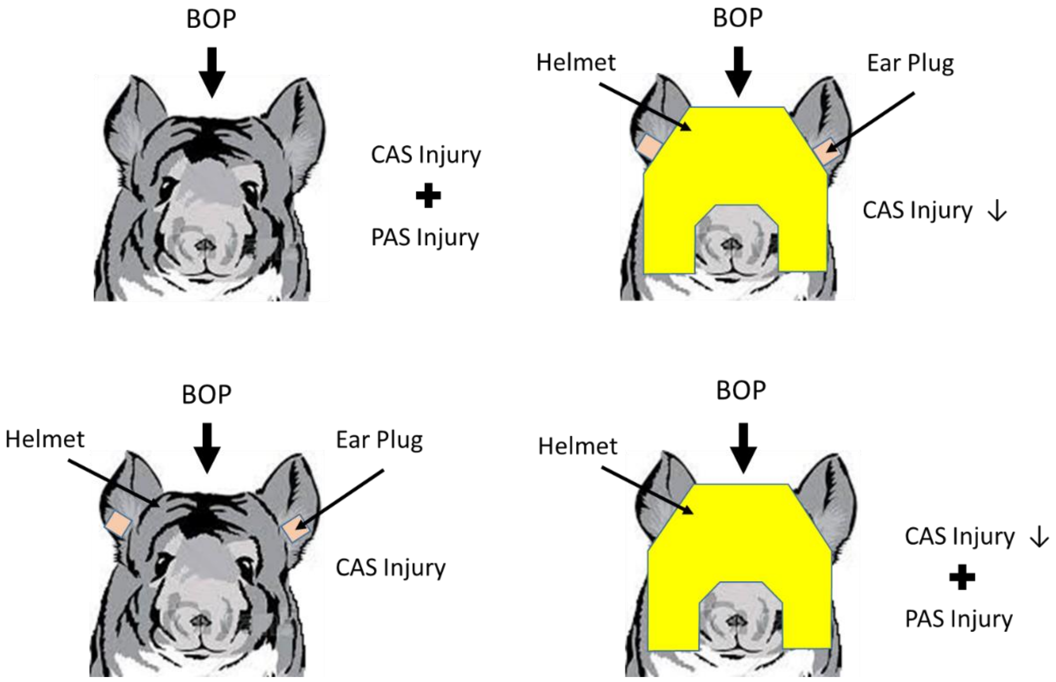

Fig. 29. Illustration on different studies for the inter-relation between CAS injury and PAS injury.

(2-5) Measurement of TM mechanical properties using biaxial tension test system

A new technique, biaxial tension measurement, to determine mechanical properties of the TM along the radial (R) and circumferential (C) direction has been developed in our lab. TM is a multiple layer membrane tissue and its fiber layer consists of radial and circumferential fibers. The orientation of the fibers reflects the strength difference of the TM along the R and C direction which is related to the TM damage analysis after blast exposure. We are currently in the process of establishing the experiment protocol including the TM sample preparation, tissue adaptor/holder design, and x- and y-axial deformation analysis.

A biaxial tension test system (Biaxial Tester CellScale) is used to test the TM samples. The stress is calculated directly from the load cell reading of the tester. The strain is determined indirectly using Digital Image Correlation (DIC) method with the help of digital images of the speckles-painted sample taken in the testing process. DIC is used to measure the strain based on images simultaneously recorded during the biaxial tensile test. The images recorded during the biaxial tensile test are read into the DIC software package SpeckleTrack to determine the strain of the sample.

TM samples can be cut from the inferior, anterior, or posterior section of the TM and then mounted to the adaptor. We plan to test the samples from two locations of the TM as shown in Figs. 30A and 30B, but the focus is on the inferior. The sample was attached to the adapters in x- and y- directions which are close to C and R directions of TM fibers. Figure 30C shows the TM sample attached to adapters in x- and y- directions, aligned with the ranks, and the adaptor released for biaxial testing. Figure 31A shows the displacement applied on the sample and Fig. 31B shows the corresponding force measured on the TM sample.

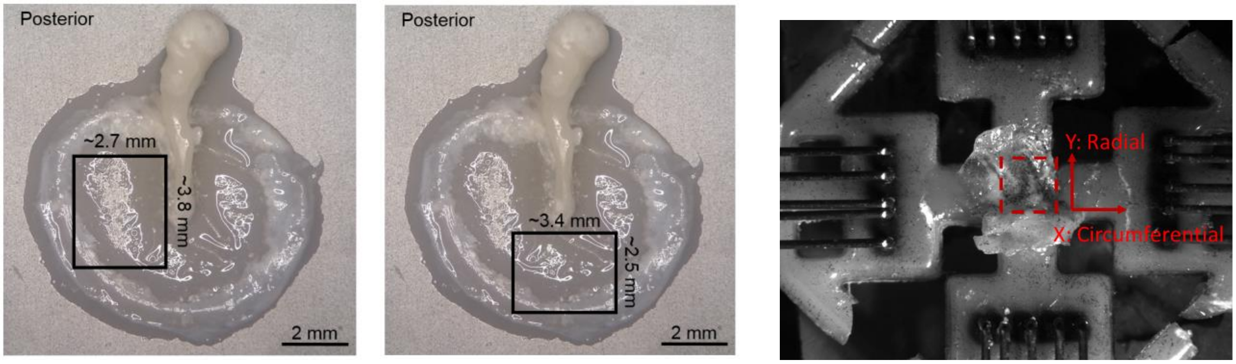

(A) (B) (C)

Fig. 30. (A) TM sample location at posterior; (B) TM sample location at inferior; (C) TM sample cut from inferior location attached to the adaptor by superglue.

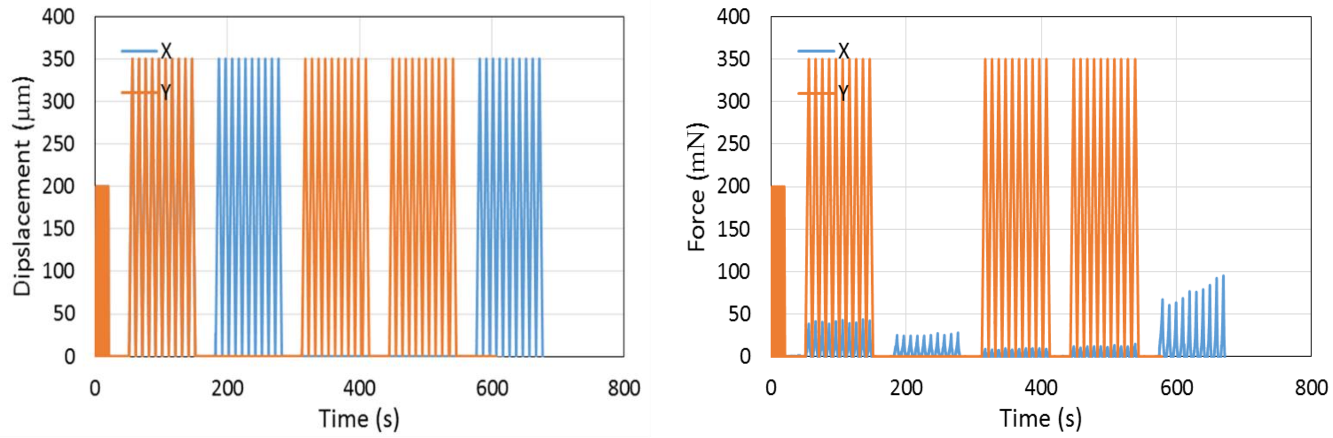

Fig. 31A. Displacement applied on the TM sample along the x- and y-direction.

(B) Force measured on the TM sample along the x- and y-direction.

Fig. 32A shows the stress-strain relationship of a TM sample in radial direction and Fig. 32B shows the stress-strain relationship in circumferential direction. To compare the mechanical properties of TM in these two directions, average values are plotted in Fig. 33.

The plot in Fig. 33 elucidates the strong anisotropic characteristics of the TM mechanical properties. The radial direction of TM is stiffer than the circumferential direction of the TM. This observation agrees with the results reported by Luo et. al., (2009). It should note that the data is relatively noisy especially in the radial direction. This could stem from the unsteadiness of the bio-rake. In next phrase, we will replace the bio-rake with bio-clamp.

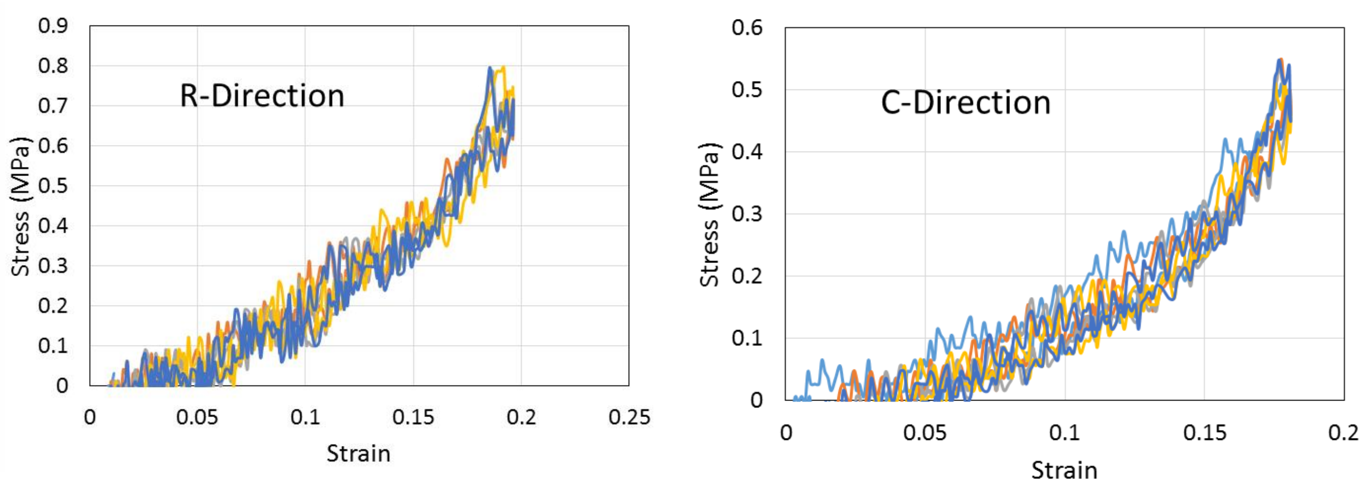

Fig. 32A. Stress-strain relationship along the radial (y-) direction.

(B) Stress-strain relationship along the circumferential (x-) direction.

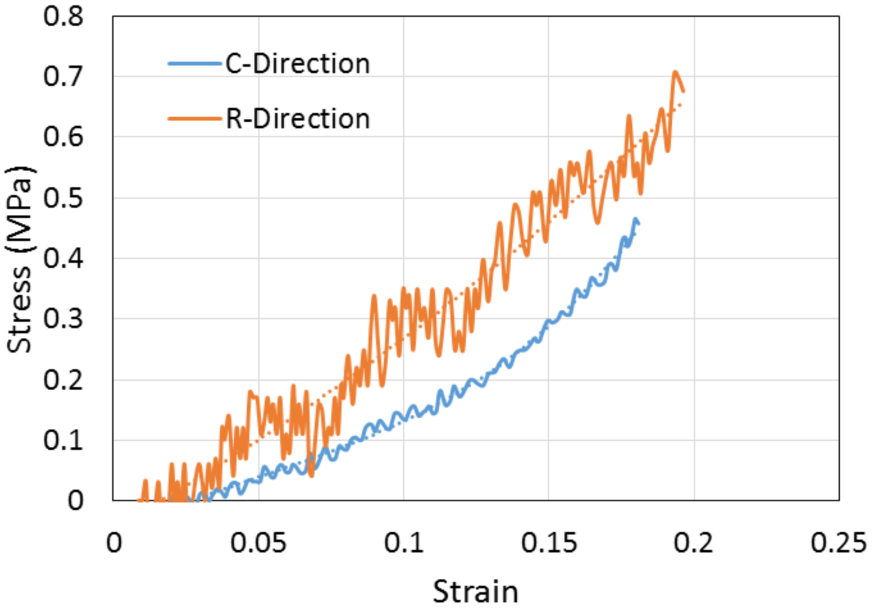

Fig. 33. Comparison of stress-strain relationships of TM sample in radial and circumferential directions.

In summary, the protocol for the biaxial test in human TM samples needs to further improve in the adapter design, method to attach the TM sample to the adapter, change of the ranks to clamps, and DIC method.

(4) In this 4th year of the project, the <u>major activities</u> under <u>Aim 3</u> include:

1) Continuing development of the FE model of the cochlea to analyze blast overpressure transmission from the external ear canal and middle ear to cochlea;
2) Improving the FE modeling process (reducing the computational time) by using the supercomputer facility at OU;
3) Including the simulation of middle ear muscle active function in the FE model;
4) Identifying injury threshold of PAS using the FE model of the human ear;
5) Improving the cleaning process for 3D printed human ear model or temporal bone, particularly the ossicular chain, and calibrating the 3D printed ear.

The **<u>specific objectives</u>** are to improve the 3D FE model of the entire human ear for understanding the blast pressure transmission through the ear and simulating blast-induced hearing damage in PAS and to seek the applications of the FE model and 3D printed human ear or temporal bone for evaluating HPDs (e.g. earplugs) design and protection mechanisms to blast waves for Service members.

(4-1) 3D FE modeling of blast wave transduction to the cochlea

The entire ear model including the external ear canal, middle ear, and cochlea for simulating the blast overpressure transduction through the ear canal, middle ear, and into the cochlea has been developed in our lab and reported in the last year's annual report. Figure 34 shows the current FE model of the human ear in ANSYS Mechanical and Fluent. To improve the model-prediction of cochlear basilar membrane (BM) vibration in response to blast pressure reaching the ear canal, the distribution of material properties of BM along the BM longitudinal distance from the base to apex is a key factor. Various material properties of the BM are currently being investigated to improve the accuracy of the FE model. The properties come from a survey of the literature and simulations are being run to see how well these properties work within our model.

Figure 35A shows the blast waveform used as the input for FE modeling of blast wave transduction through the ear, which was recorded at the entrance of the ear canal (P0) in the temporal bone experiments. Figure 35B shows the locations of P0, P1, and P2 in the FE model which are the same locations of 3 pressure sensors placed in the temporal bone experiments. The model was validated by comparison of model-derived P1 and P2 pressures with the data measured from the cadaver ear experiments as shown in Fig. 36 as the comparison of model-predicted P1 and P2 waveforms with those of experimentally measured data in human temporal bones. The BM displacement and cochlear pressures across the BM are also derived from the model as described below.

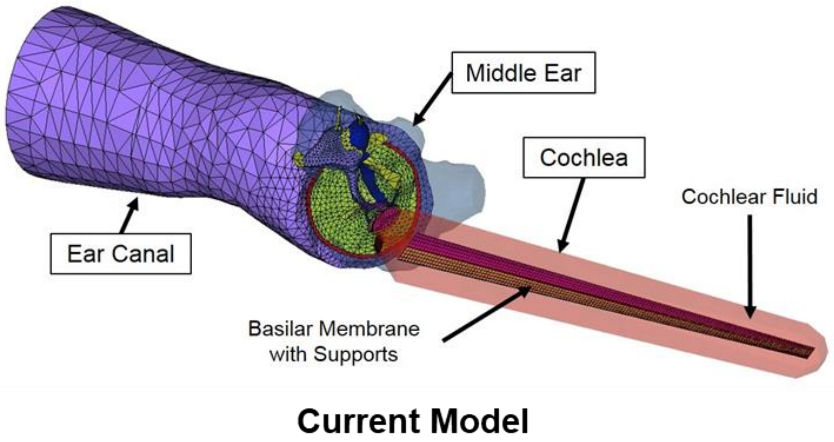

Fig. 34. Current 3D FE model of the entire ear for running transient analysis of blast overpressure transmission from the ear canal to cochlea. The model has ear canal, middle ear, and a two-chamber, straight cochlea.

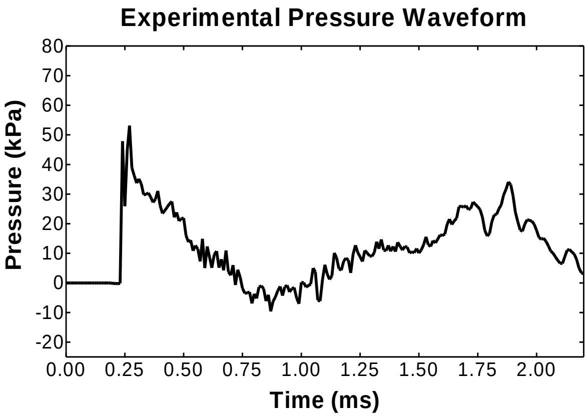

Fig. 35A. Blast overpressure waveform P0 used as the input for the FE model.

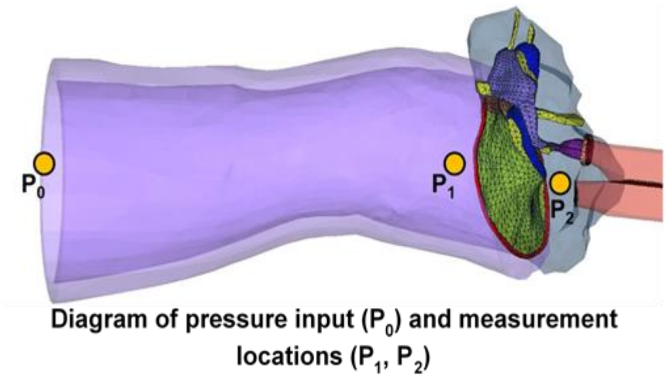

(B) P0, P1, and P2 locations in the model. P1 is near the TM in the canal and P2 is in the middle ear cavity behind the TM.

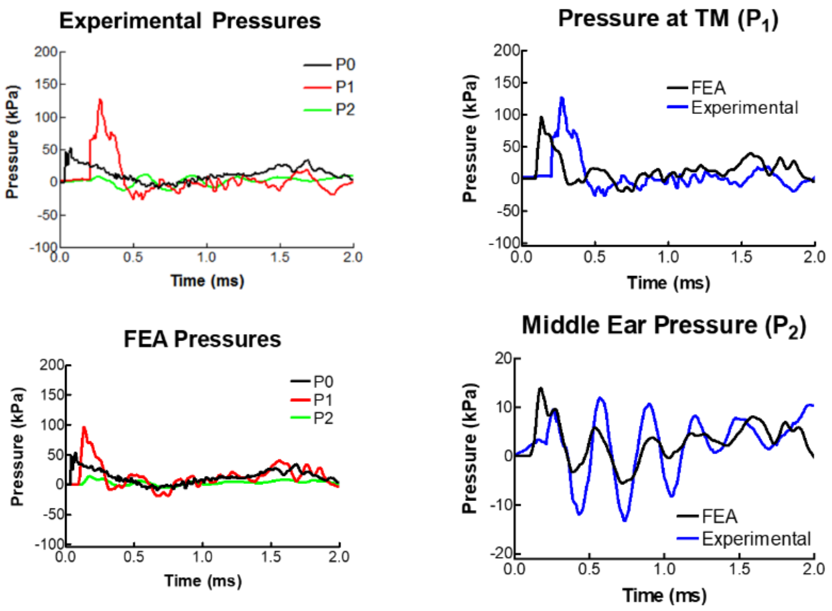

Fig. 36. Plots comparing simulated and experimental pressure measures of the ear canal near the TM and middle ear cavity. The two figures on the left show the P0, P1, and P2 values over a 2 ms interval with the experimental results on top and the FE analysis (FEA) pressures below. Right plots show comparisons between simulated and experimental results of ear canal pressures (Top) and middle ear cavity pressures (Bottom).

The model was run with the PISO scheme in ANSYS Fluent and the transient formulation was set to 2nd order implicit instead of with a 1st order SIMPLE scheme. This was done to increase the accuracy of the model for the cochlea. Figure 37A shows the maximum BM displacement over the time derived from the model and Fig. 37B shows the BM displacement at different locations (4.3, 10.5, 16.8, 23.0, and 29.3 mm from the base of BM) over the time. The maximum displacement 250 μm occurred at 0.6 ms as shown in Fig. 37A and large BM displacement was around 23 mm from the BM base (blue line) shown in Fig. 37B. The cochlear fluid pressures at 4 locations (0.25, 7.5, 20.0, and 28.75 mm) are displayed in Fig. 38.

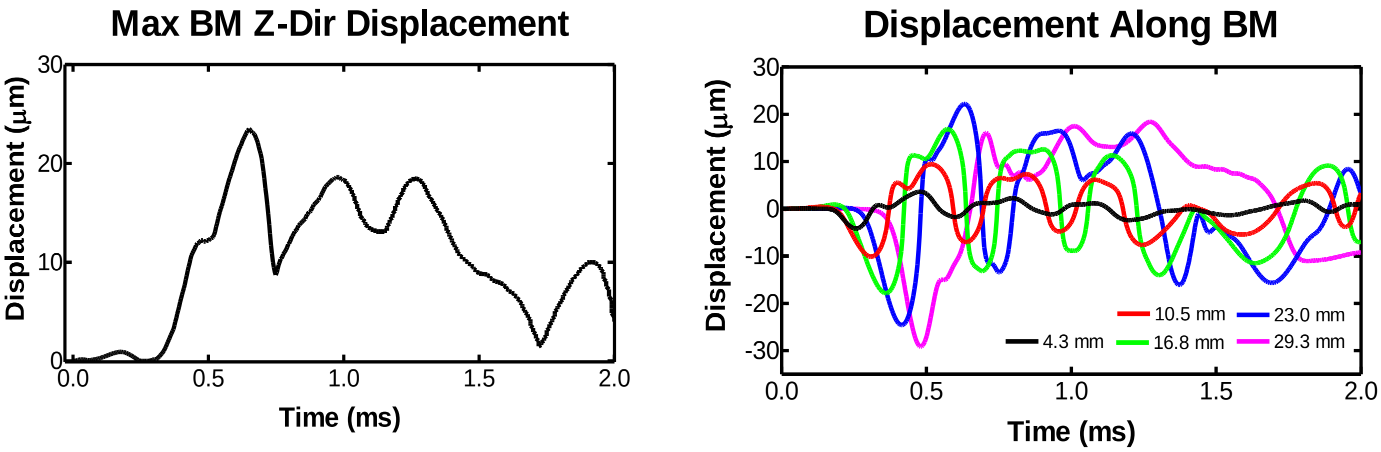

Fig. 37A. Maximum BM displacement in the positive z-direction. (B) BM displacement over time at different points along the BM.

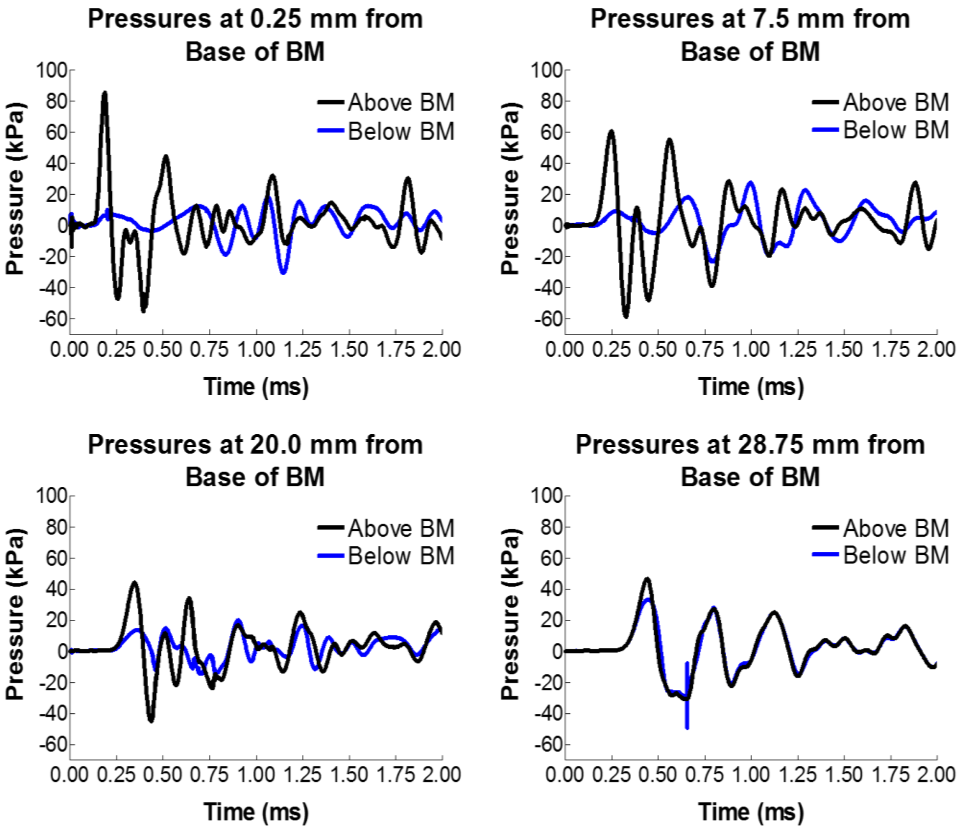

Fig. 38. Fluid pressures in the cochlea at four distances from the base of the BM: 0.25, 7.5, 20, and 28.75 mm. “Above BM” represents the scalar vestibuli and “Below BM” represents the scalar tympany in the cochlea.

The model is currently being evaluated for its ability to predict middle ear injury during blast exposure. Figure 39 shows that the model-resulted high stress regions on the TM can predict where the failure is likely and the injury threshold in the TM. Figure 40 shows the location and high stress regions in the middle ear ossicular chain, which highlight the possible failure of middle ear ossicular chain. The model results of TM or stapes footplate displacement with respect to P0 or P1 pressure can represent function damage of the middle ear. The FE model results of cochlear pressure across the BM and the BM displacement can represent function damage of the cochlea. In summary, the 3D FE model of the human ear can become a standard for evaluating ear damage from blast exposure as well as for evaluation of the HDPs in their design and protection function.

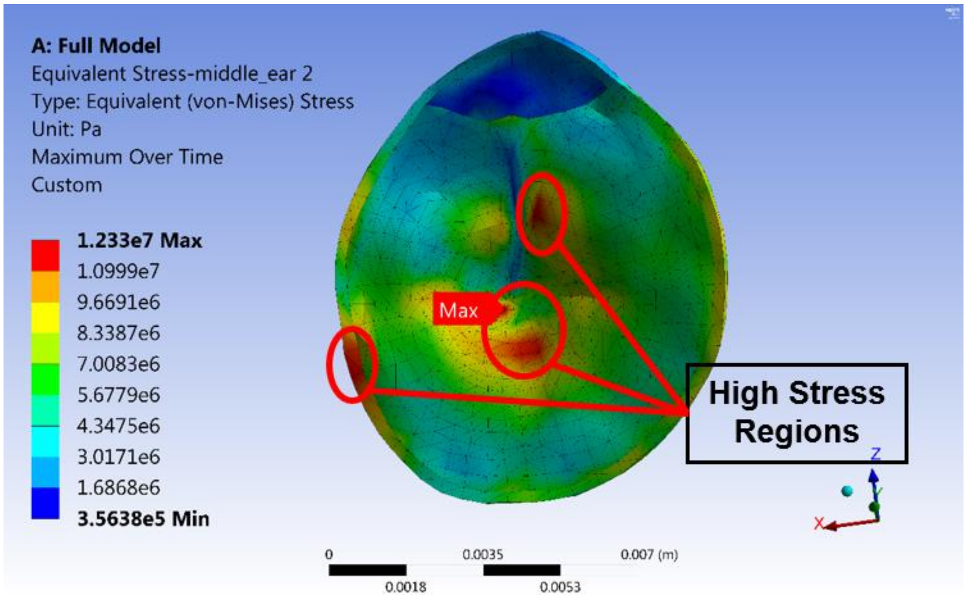

Fig. 39. Stress contour plot highlighting high stress regions in the TM during blast exposure simulation.

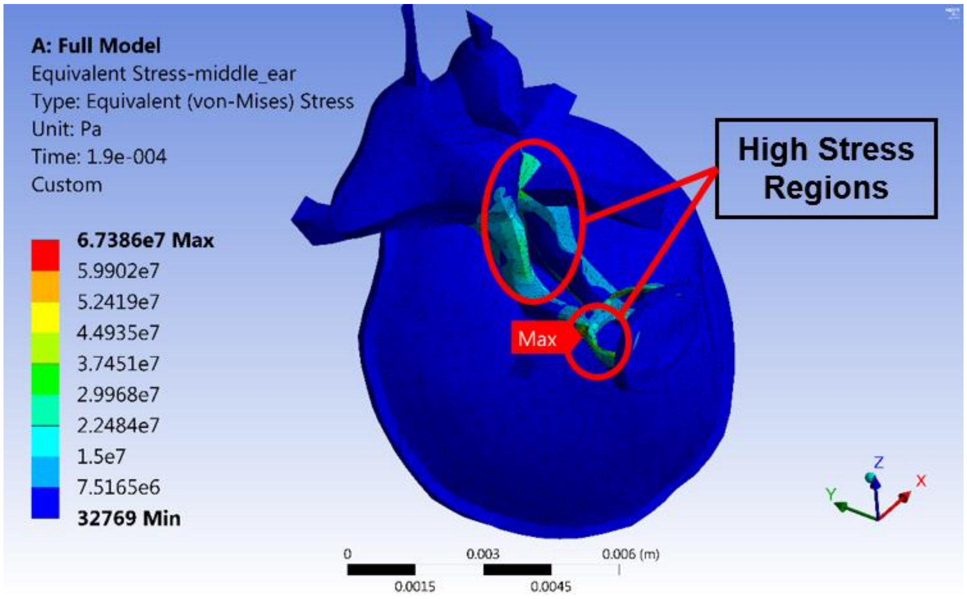

Fig. 40. Stress contour plot highlighting high stress regions in the ossicles during blast exposure simulation.

(4-2) Simulation of middle ear muscle active function in the FE model

Middle ear reflex is an involuntary middle ear muscle contraction that occurs in response to high-intensity sound stimuli. There are two muscles in the human middle ear: the stapedius muscle and tensor tympani muscle which are included in our 3D FE model and denoted as C5 and C7, respectively. The movement of the ossicles is stiffened by the muscle contraction in response to high intensity sound so that the sound energy transmitted into the cochlea would be reduced.

In the FE model, the middle ear reflex is implemented by increasing the stiffness of the muscle (e.g. stapedius muscle C5). We first create the middle ear impedance change as a function of muscle stiffness change. Then, using the function of impedance change vs sound intensity published by A. R. MØller (1962), we create a function of stiffness change of the muscle vs sound intensity. The middle ear reflex is indirectly implemented by associating the stiffness change of the muscle with sound intensity.

As an example, Fig. 41 shows the FE model-derived the middle ear impedance change with respect to the stapedius muscle stiffness change or the relationship between the stapedius stiffness and middle ear impedance. E/E_0 is the ratio of active C5 stiffness to normal (passive) C5 stiffness. Figure 42 displays the comparison of stapes footplate displacement in warned or with active C5 muscle and the unwarned with passive or normal C5 muscle. Figure 43 displays the warned vs unwarned stapes movement caused by stapedius muscle C5 contraction. With an unwarned response (e.g. low stiffness), the maximum stapes displacement was about 140 micron with a blast of 5 psi. A warned response, however, reduces this maximum displacement by an order of magnitude.

We will continue working on our FE model for simulation of the middle ear muscle reflex. Note that the electromyographic measurement of the stapedius muscle reflex in chinchillas has been conducted in our lab with several conference publications. A PhD dissertation about this topic will be defensed in November 2018. The animal data will help us in modeling the middle ear muscle function.

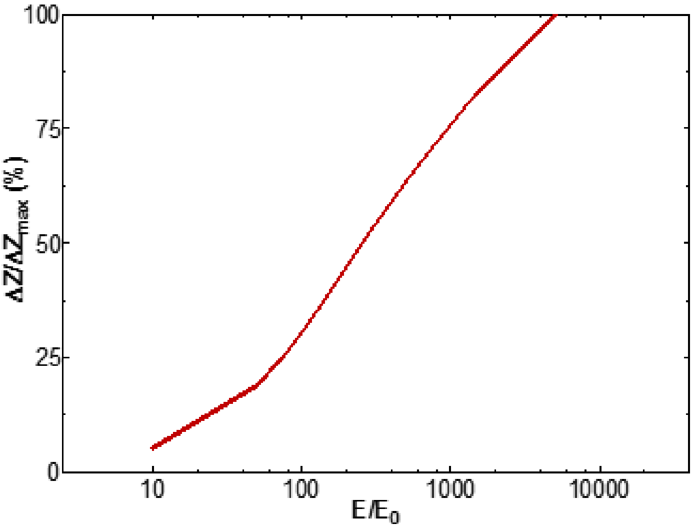

Fig. 41. FE model-derived the middle ear impedance change with respect to the stapedius muscle (C5) stiffness. E/E_0 is the ratio of active C5 stiffness to normal (passive) C5 stiffness.

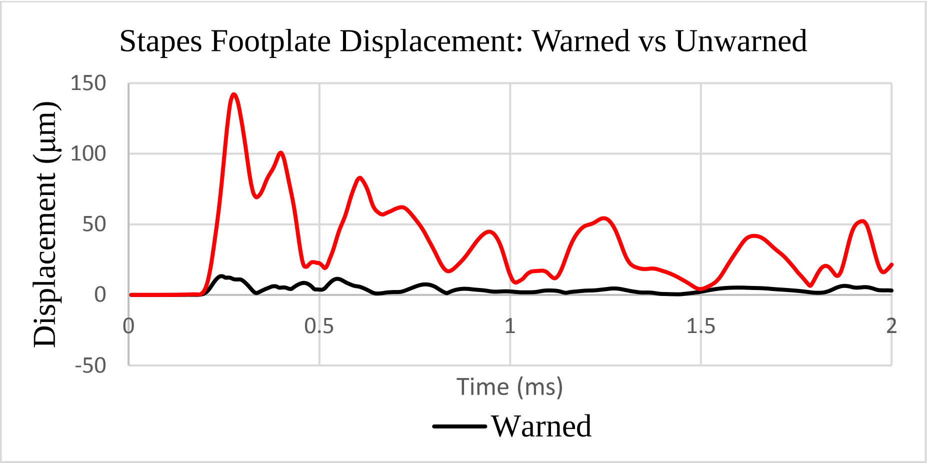

Fig. 42. Stapes displacement calculated from the model with stapedius muscle contraction: warned vs. unwarned.

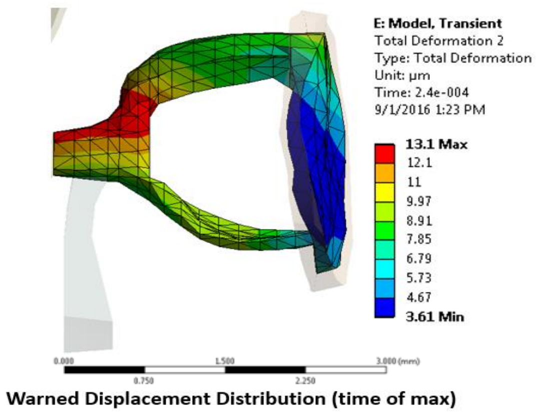

Fig. 43A. Stapes displacement derived from the FE model in warned case with stapedius muscle reflex.

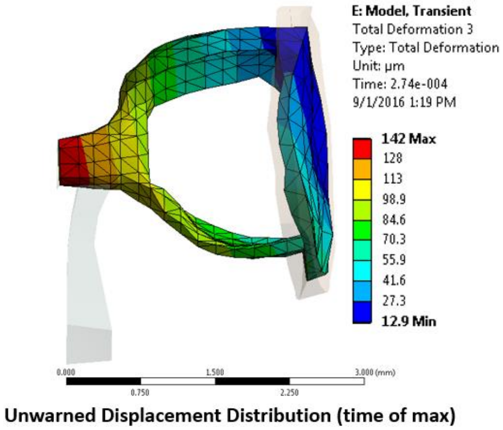

(B) Stapes displacement from the model in unwarned case.

(4-3) Improvement of 3D printed human temporal bone or human ear

The 3D printing system (Object350, Stratasys) with multiple materials was used to print human temporal bone (TB) consisting of the ear canal, TM, middle ear ossicular chain, and middle ear cavity. The cochlear load was added to the stapes footplate through liquid pressure.

- The middle ear portion of the 3D printed TB was modified allowing for improved cleaning of the middle ear cavity. The changes can be seen in Figs. 44 and 45. The top slot was increased to allow removal of more support material from the posterior portion of the middle ear cavity, and more of the anterior wall of the middle cavity was removed to further improve cleaning. These improvements resulted in models that have all the support material removed from the middle ear cavity, and an example is shown in Figs. 46 and 47.

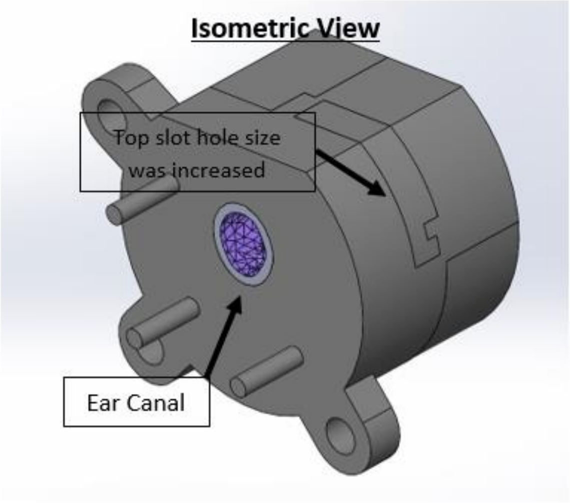

Fig. 44. Isometric view for CAD Model of middle ear portion.

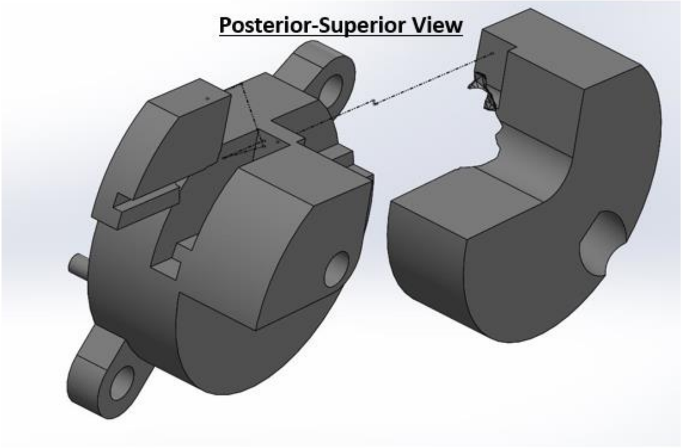

Fig. 45. Exploded view of CAD model of middle ear portion showing the top slot with an increased opening from the posterior-superior side.

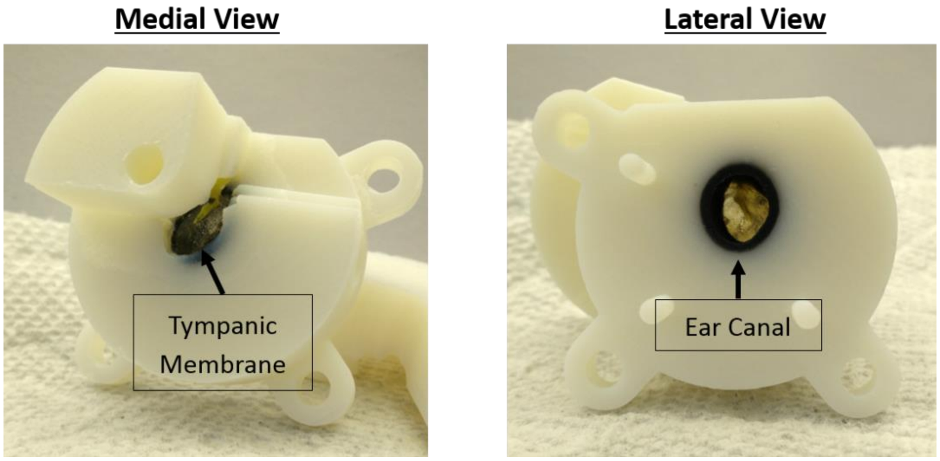

Fig. 46. 3D Model of middle ear portion from medial (left) and lateral (right) side views.

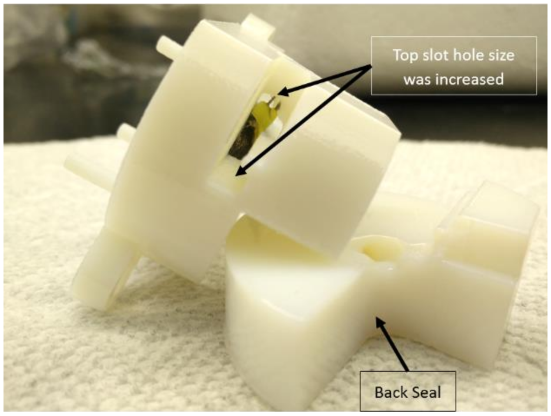
Posterior View

Fig. 47. 3D Model of middle ear portion from posterior side. The image shows the increased opening in the top slot.

- The left image in Fig. 48 shows the middle ear structures printed in the model after it has been cleaned. The right image in Fig. 48 shows the ossicular chain printed at 5 times the scale used in the 3D printed TB.
- Preliminary LDV measurements have been done on the 3D printed TB. Once the preliminary data is analyzed, the 3D printed model will be modified to better mimic the TM displacement shown in the published results of LDV experiments.
- The 3D printed model is currently undergoing blast tests to evaluate how effective the model is at simulating the blast tests with cadaver TB. These tests will be conducted with and without hearing protection devices. The results will be compared with previously published data to confirm the effectiveness.
- The materials used in the model being characterized with mechanical tests to have a more accurate description of the 3D printed materials' mechanical properties.
- This project will be presented at the 2018 BMES Annual Meeting as a poster presentation.

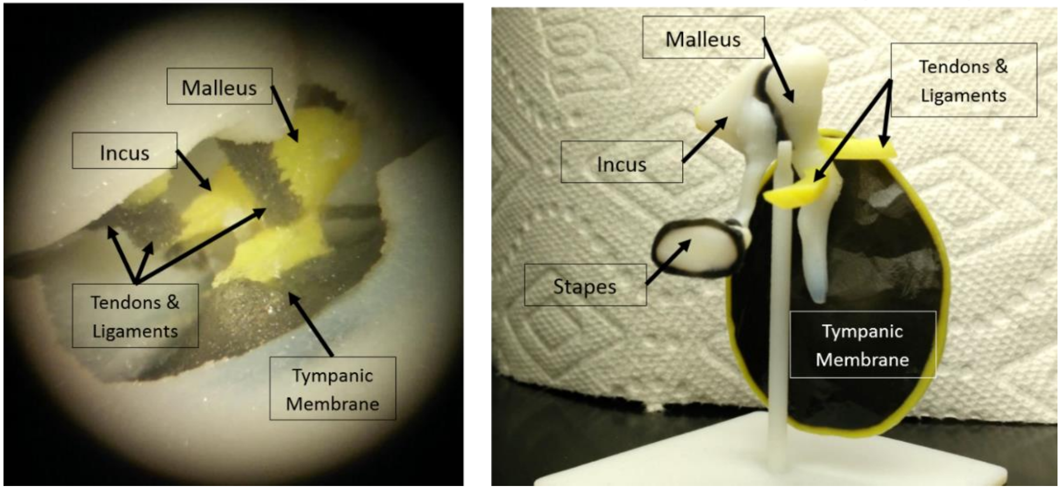
Inferior View

3D Printed TM & Ossicles (5:1 Scale)

Fig. 48. Close-up image on 3D printed middle ear cavity (Left) from inferior side, and image of 3D printed TM, ossicular chain, ligaments and tendons (right).

- **What opportunities for training and professional development has the project provided?**

Nothing to Report

- **How were the results disseminated to communities of interest?**

Nothing to Report

- **What do you plan to do during the next reporting period to accomplish the goals?**

(1) Biomechanical analysis of TM rupture threshold and TM tissue damage after multiple blast exposure will continue with a focus on mechanisms of tissue injury and tissue mechanical property changes after blast exposure. With the dual laser setup and the high-speed camera, we may try to extend the measurement of TM motion to the measurement of the stapes or middle ear ossicular motion during the blast exposure.

Evaluation of HPDs (earplugs) in human cadaver ears, animal ears, and the 3D printed human ear and calculated from the FE model are promising. The standard criteria for HPDs design and function evaluation based on nonlinear FE model of the human ear and biomechanics of tissue injury after blast exposure will be delivered.

Several manuscripts will be prepared and submitted including: 3D printed ear model for standardized testing of HPDs to blast exposure, TM vibration behavior after multiple-blast exposure, the transfer functions of the ear canal and middle ear in response to blast overpressure, etc.

(2) The study on auditory dysfunction after repetitive exposures to the low BOP or mild TBI level will continue in chinchillas. We will focus on the biomechanical damage induced by blast in peripheral auditory system (PAS) and the neurophysiological injury in central auditory system (CAS). The preliminary study on chinchilla helmet has proved that using a well-designed helmet in animal is a good approach for the objective of isolating the PAS injury from the CAS injury studies. In the next phrase, ABR will be measured in animals with helmet but without earplug and in animals with earplug but without helmet, which will grant us more comprehensive understanding the injuries from either the PAS or the CAS caused by blast overpressure.

In addition to acute hearing damage after blast exposure, we will conduct longitudinal studies to explore progressive hearing damage in the conductive path of blast through the ear canal and middle ear into the cochlea. The ABR hearing threshold measurement will be extended to include ABR wave 1 amplitude and latency. ABR wave 1 signal reflects the function of cochlear spiral ganglion neurons and the ribbon synapses.

We will further improve the SEM imaging of cochlear hair cells in sample preparation and handling and will quantify the damages from the basal tern to apex under different BOP levels. This imaging study on cochlear injury will be correlated with the auditory function damage during the time course after blast exposure.

The tissue mechanical tests on human TM using biaxial tension test system will continue in the next year. We will improve the adapter design, method to attach the TM sample to the adapter, and DIC method for calculating deformation or strain in both radial and circumferential directions.

Several manuscripts will be prepared and submitted including: the electromyographic (EMG) measurement of middle ear muscle reflex in response to acoustic sound and blast waves, the effect of noise exposure on middle ear muscle reflex, the hearing damage induced by blast overpressure at the mild TBI level in chinchillas, and the dynamic properties of the ISJ measured by the miniature split Hopkinson tension bar (SHTB) system.

(3) The FE model of the entire human ear will be improved in two directions:
1) extend the application of the 3D FE model for prediction of middle ear and cochlear injuries induced by blast waves. The FE model of the human ear will become a standard for evaluating ear damage from blast exposure as well as for evaluation of the HPDs in their design and protection function.
2) continue the FE simulation of middle ear muscle active function in the ear model. We will further identify the relationship of FE model-derived middle ear impedance change with respect to the stapes muscle stiffness. The function of stiffness change of the muscle vs sound intensity will be created. On the other hand, the EMG measurement data of the stapedius muscle reflex in chinchillas will help us in modeling the middle ear muscle function. We will first use the data in our published 3D FE model of the chinchilla ear and then transfer the results to human ear model.

There are several issues in the 3D printing system:
- Cleaning of the middle ear cavity still needs to be improved. Some of the support material remains in the middle ear cavity and is an area where it is difficult to clean without damaging the sensitive parts of the model.
- 3D-printed human temporal bone or ear model will be calibrated for the TM movement with LDV in comparison with the published data measured in human cadaver temporal bones.
- The materials used in the model will be characterized with mechanical tests to have a more accurate description of the 3D printed materials’ mechanical properties.
- The 3D printed model is currently undergoing blast tests to evaluate how effective the model is in comparison with the blast tests in cadaver temporal bones. These tests will be conducted with and without hearing protection devices to verify that the 3D printed ear model for standardized testing of HPDs to blast exposure.

4. **IMPACT**

● **What was the impact on the development of the principal discipline(s) of the project?**

The accomplishments in the 4th year have great impact to understanding the hearing damage induced by blast exposure at different situations in relation to the BOP or TBI and the protection mechanisms of HPDs (earplugs) to blast exposure.

● It is the first time that the movement of the TM under blast exposure measured by the dual-laser setup. The method developed in this project provides a new methodology to determine the behavior of the middle ear in response to blast overpressure. The experimental data are critical for validating the FE model of the human ear for blast wave transduction and understanding the TM damage induced by blast exposure.

● Hearing damage in relation to number of blast exposures at an equivalent level to the mild TBI (15-20 psi or 105-138 kPa) and the hearing damage after repetitive exposure to the low BOP level (3-5 psi or 21-35 kPa) were investigated in chinchillas with the measurements of ABR threshold and DPOAE level over 7 days and 14 days. Animal ears were either both protected with earplugs for the high BOP (mild TBI) or one ear protected and one ear open for low BOP exposure. The experimental results provide important information about permanent hearing damage in relation to the parameters including the intensity of BOP level, number of blast exposures, and time course after exposure. Our results demonstrate that the HPDs can mitigate the hearing damage and help the recovery, but the effectiveness depends on the BOP intensity or TBI severity and the number of blast exposures.

● The 3D FE model of the human ear has been evaluated for its ability to predict middle ear injury during blast exposure in following areas. 1) The model-resulted high stress regions on the tympanic membrane (TM) can predict where the rupture is likely and the injury threshold in the TM. 2) The location and high stress regions in the middle ear ossicular chain highlight the possible failure of middle ear ossicular chain. 3) The model resulted the TM or stapes displacement induced by blast pressure at the entrance of the ear canal can represent function damage of the middle ear. 4) The FE model-derived cochlear pressure across the basilar membrane (BM) and the BM displacement can represent function damage of the cochlea.

● The FE model is also used for production of the 3D printed physical model of the human ear or temporal bone (TB). The 3D printing system with multiple materials (Object350, Stratasys) is used for producing the TB which consists of the ear canal, TM, middle ear ossicular chain, and middle ear cavity. The 3D printed TB is validated for creating a standardized testing model for HPDs. The model is also tested under blast exposures to evaluate its performance in the extreme conditions Service members experience. The 3D printed TB shows similar results in pressure measurements to the tests done with a human cadaver TB.

● Characterization of HPDs protection function to blast exposure through experiments in human cadaver ears, animal ears, and the 3D printed human ear and the simulation in FE model are major outcomes from this research project. The standard criteria for HPDs design and evaluation based on nonlinear FE model of the human ear and biomechanics of tissue injury after blast exposure will be delivered.

- **What was the impact on other disciplines?**

Nothing to Report

- **What was the impact on technology transfer?**

Nothing to Report

- **What was the impact on society beyond science and technology?**

Nothing to Report

5. CHANGES/PROBLEMS

- **Changes in approach and reasons for change**

No significant changes in approach.

- **Actual or anticipated problems or delays and actions or plans to resolve them**

No significant problems and delays.

- **Changes that had a significant impact on expenditures**

No changes in expenditures.

- **Significant changes in use or care of human subjects, vertebrate animals, biohazards, and/or select agents**

Animal study protocol R14-001 at OU was renewed on February 20, 2017 as protocol R17-004. Then, the IACUC committee requested to submit a new protocol using the new forms and the protocol was approved with a new tracking number R17-015. This new protocol R17-015 was submitted to USAMRMC ACURO on March 31, 2017 and approved by ACURO on May 4, 2017.

6. PRODUCTS

- publications, conference papers, and presentations;
- website(s) or other Internet site(s);
- technologies or techniques;
- inventions, patent applications, and/or licenses; and
- other products.

- **Publications, conference papers, and presentations**

Journal publications:

1. Gan, R. Z., Leckness, K., Nakmali, D., and Ji, X. D. Biomechanical measurement and modeling of human eardrum injury in relation to blast wave direction. *J. Military Medicine*, Vol. 183, 3/4: 245-251, 2018.

2. Leckness, K., Nakmali, D., and Gan, R. Z. Computational modeling of blast wave transmission through human ear. *J. Military Medicine*, Vol. 183, 3/4: 262-268, 2018.

3. Gan, R. Z., Leckness, K., Smith, K., and Ji, X. D. Characterization of protection mechanisms to blast overpressure for personal hearing protection devices – Biomechanical measurement and computational modeling. *J. Military Medicine*, 2018 (In Press)

4. Jiang S., and Gan, R. Z. Dynamic properties of human incudostapedial joint measured with frequency-temperature superposition. *Medical Engineering & Physics*, Vol. 54: 14-21, 2018.

5. Jiang, S., Smith, K., and Gan, R. Z. Dual-laser measurement and finite element modeling of human tympanic membrane motion under blast exposure. *Hearing Research*, 2018 (Under Review)

6. Chen, T., Smith, K., Jiang, S., Zhang, T., and Gan, R. Z. Progressive Hearing Damage after Repeated Exposure to Low Level of Blast Overpressure in Chinchillas. *Hearing Research*, 2018 (Under Review)

7. Luo, H., Wang, F., Chen Cheng, C., Nakmali, D., Dai, C., Li, W., Gan, R. Z., and Lu, H. Measurement of the through-thickness Young's modulus of a human tympanic membrane by nanoindentation. *Hearing Research*, 2018 (Under Review)

8. Liang, J., Smith, K., Gan, R. Z., and Lu, H. Effect of blast overpressure on mechanical properties of human tympanic membrane. *J. Mech. Behavior Biomed Materials*, 2018 (Under Review)

9. Gan, R. Z. Biomechanical changes of tympanic membrane to blast waves. In: Molecular, Cellular and Tissue Engineering of the Vascular System. Bingmei Fu and Neil Wright, eds. Springer, pp. 321-334, 2018.

10. Liang, J., Gan, R. Z., and Lu, H. Measurement of the visco-elastic properties of the chinchilla tympanic membrane. Mechanics of Biological Systems & Micro- and Nanomechanics, Volume 4, Conference Proceedings, 2018.

11. Jiang, S. Mechanical Properties of Human Incudostapedial Joint and Tympanic Membrane in Normal and Blast-damaged Ears. Dissertation for Ph.D. Degree in Biomedical Engineering at University of Oklahoma, May 2018.

Publications – Conference papers:

1. Gan, R. Z., Chen, T., Smith, K., and Jiang, S. Therapeutic function of glucagon-like peptide-1 (GLP-1) for hearing restoration after blast exposure. *Proceedings of the Biomedical Engineering Society 2018 Annual Meeting*, Atlanta, Georgia, October 17-20, 2018.
2. Brown, M., Jiang, S., and Gan, R. Z. A 3D printed ear model for standardized testing of hearing protection devices to blast exposure. *Proceedings of the Biomedical Engineering Society 2018 Annual Meeting*, Atlanta, Georgia, October 17-20, 2018.
3. Gan, R. Z., Chen, T., and Smith, K. Hearing damage induced by blast Overpressure at the mild TBI level in a chinchilla model. *DoD 2018 Military Health System Research Symposium (MHSRS)*, Kissimmee, FL, August 20-23, 2018.
4. Chandra, N., Shao, N., Rama Rao, K. V., Jiang, S., Chen, T., Brown, M., and Gan, R. Z. Central and peripheral auditory abnormalities in animal models of blast-injury. *DoD 2018 Military Health System Research Symposium (MHSRS)*, Kissimmee, FL, August 20-23, 2018. (Podium Presentation)
5. Gan, R. Z., Jiang, S., and Smith, K. Dual-laser measurement and finite element modeling of human tympanic membrane motion under blast exposure. *8th International Symposium on Middle Ear Mechanics in Research and Otology (MEMRO)*, Shanghai, China, July 5 – 9, 2018. (Podium Presentation)
6. Chandra, N., Shao, N., Rama Rao, K. V., Jiang, S., Chen, T., Brown, M., and Gan, R. Z. Central and peripheral auditory injuries in animal models after blast exposure. *8th International Symposium on Middle Ear Mechanics in Research and Otology (MEMRO)*, Shanghai, China, July 5 – 9, 2018. (Podium Presentation)
7. Chen, T., Smith, K., Jiang, s., Zhang, T., and Gan, R. Z. Progressive Hearing Damage after Repeated Exposure to Low Level of Blast Overpressure in Chinchillas. *8th International Symposium on Middle Ear Mechanics in Research and Otology (MEMRO)*, Shanghai, China, July 5 – 9, 2018. (Podium Presentation)
8. Luo, H., Wang, F., Chen Cheng, C., Nakmali, D., Dai, C., Li, W., Gan, R. Z., and Lu, H. Measurement of the through-thickness Young's modulus of a human tympanic membrane by nanoindentation. *8th International Symposium on Middle Ear Mechanics in Research and Otology (MEMRO)*, Shanghai, China, July 5 – 9, 2018. (Podium Presentation)
9. Brown, M., Chen, T., and Gan, R. Z. SEM Imaging of Cochlear Hair Cell Damage Caused by Blast Exposure. *Association for Research in Otolaryngology (ARO) - Midwinter Meeting*, San Diego, CA, February 10-14, 2018.
10. Chen, T., Smith, K., and Gan, R. Z. Progressive Hearing Damage after Exposure to Multiple Blasts in Chinchillas. *Association for Research in Otolaryngology (ARO) - Midwinter Meeting*, San Diego, CA, February 10-14, 2018.
11. Liang, J., Gan, R. Z., and Lu, H. Measurement of the visco-elastic properties of the chinchilla tympanic membrane. Soc. Exp. Mech., IMAC conference, Orlando, FL, February 2018.

Books or other non-periodical, one-time publications:

N/A

7. PARTICIPANTS & OTHER COLLABORATING ORGANIZATIONS

- **What individuals have worked on the project?**

Provide the name and identify the role the person played in the project. Indicate the nearest whole person month (Calendar, Academic, Summer) that the individual worked on the project. Show the most senior role in which the person worked on the project for any significant length of time. For example, if an undergraduate student graduated, entered graduate school, and continued to work on the project, show that person as a graduate student, preferably explaining the change in involvement.
Describe how this person contributed to the project and with what funding support. If information is unchanged from a previous submission, provide the name only and indicate "no change".

Name: Rong Gan, Ph.D.
Project Role: PI
Researcher Identifier (OU ID): 112129499
Nearest person month worked: 3
Contribution to Project: No change

Name: Xiao Ji, Ph.D.
Project Role: Research Associate
Researcher Identifier (OU ID): 112902618
Nearest person month worked: 3
Contribution to Project: No change

Name: Zachary Yokell
Project Role: Ph.D. Student
Researcher Identifier (OU ID): 112760109
Nearest person month worked: 2
Contribution to Project: No change

Name: Shangyuan Jiang
Project Role: Ph.D. Student
Researcher Identifier (OU ID): 112979369
Nearest person month worked: 3
Contribution to Project: No change

Name: Marcus Brown
Project Role: Ph.D. Student
Researcher Identifier (OU ID): 113383397
Nearest person month worked: 2
Contribution to Project: No change

Name: Kyle Smith
Project Role: M.S. Student
Researcher Identifier (OU ID): 112831425
Nearest person month worked: 3
Contribution to Project: No change

Name: Paige Welch
Project Role: Undergraduate Student
Researcher Identifier (OU ID):
Nearest person month worked: 1
Contribution to Project: Paige has worked on the 3D FE model of the chinchilla ear

Name: Robert Beem
Project Role: Undergraduate Student
Researcher Identifier (OU ID):
Nearest person month worked: 1
Contribution to Project: Robert has been working on pressure sensor calibration and 3D printed human ear model

Name: Emily May
Project Role: Undergraduate Student
Researcher Identifier (OU ID):
Nearest person month worked: 1
Contribution to Project: Emily has been working 3D printed human ear model for improving cleaning process and calibration

Name: Tao Chan
Project Role: Scholar
Researcher Identifier (OU ID): 464955
Nearest person month worked: 1
Contribution to Project: No change

Name: Hongbing Lu, Ph.D.
Project Role: PI at UTD (subcontract)
Researcher Identifier (UTD ID): 2011733939
Nearest person month worked: 2
Contribution to Project: No change

Name: Junfeng Liang, Ph.D.
Project Role: Post-Doc
Researcher Identifier (UTD ID): N/A
Nearest person month worked: 3
Contribution to Project: No change

Name: Huiyang Luo, Ph.D.
Project Role: Research Scientist
Researcher Identifier (UTD ID): 0000-0001-7149-8609
Nearest person month worked: 2
Contribution to Project: No change

- **Has there been a change in the active other support of the PD/PI(s) or senior/key personnel since the last reporting period?**

Nothing to Report.

- **What other organizations were involved as partners?**

Nothing to Report.

8. SPECIAL REPORTING REQUIREMENTS

QUAD CHARTS: The Quad Chart (available on https://www.usamraa.army.mil) shall be updated and submitted as an appendix.

A Quad Chart is submitted as an appendix.

9. APPENDICES

- **Quad Chart**
-

MILITARY MEDICINE, 183, 3/4:245, 2018

Biomechanical Measurement and Modeling of Human Eardrum Injury in Relation to Blast Wave Direction

Rong Z. Gan, PhD; Kegan Leckness, MS; Don Nakmali, MS; Xiao D. Ji, PhD

ABSTRACT Rupture of the eardrum or tympanic membrane (TM) is one of the most frequent injuries of the ear after blast exposure. To understand how the TM damage is related to blast wave direction, human cadaver ears were exposed to blast waves along three directions: vertical, horizontal, and front with respect to the head. Blast overpressure waveforms were recorded at the ear canal entrance (P0), near the TM (P1), and inside the middle ear (P2). Thirteen to fourteen cadaver ears were tested in each wave direction and the TM rupture thresholds were identified. Results show that blast wave direction affected the peak P1/P0 ratio, TM rupture threshold, and energy flux distribution over frequencies. The front wave resulted in lowest TM rupture threshold and the horizontal wave resulted in highest P1/P0 ratio. To investigate the mechanisms of TM injury in relation to blast wave direction, the recorded P1 waveforms were applied onto the surface of the TM in a three-dimensional finite element model of the human ear and distributions of the stress in TM were calculated. Modeling results indicate that the sensitivity of TM stress change with respect to P1 pressure ($d\sigma/dP_1$) may characterize mechanical damage of the TM in relation to blast waves.

INTRODUCTION

Exposure to high-intensity sound or blast overpressure waves is considered to be an intrinsic situation faced by military personnel involved in combat operations. Over 60% of wounded-in-action service members have tympanic membrane (TM) injuries, tinnitus, and/or hearing loss.[1,2] The primary blast injury to the ear is caused by direct effect of the blast overpressure wave upon the TM and middle ear ossicular chain. Rupture of the TM is one of the most frequent injuries of the ear and has been investigated in animals and humans with wide variability.[3,4]

A recent study on chinchilla blast model by Gan *et al.*[5] reported the relationships between the TM rupture threshold, the TM damage pattern, and the overpressure waveforms. The results demonstrated that the TM rupture threshold was closely related to pressure waveforms at the entrance of the ear canal. The waveforms recorded under the shielded case had almost equal positive–negative pressure phases while the waveforms recorded in the open field had the positive pressure only. The TM rupture threshold measured in the shielded case was much lower than that in the open field. These findings in animal blast model brought further research requests on identifying human TM damage after blast exposure and the TM rupture threshold in relation to blast overpressure wave direction.

This paper reports our current study of measuring blast wave transmission through the human ear under three different incident blast directions with respect to the head or ear. In addition to experimental tests in human cadaver ears, a three-dimensional (3D) finite element (FE) model of the human ear for blast simulation was developed to simulate blast overpressure transduction through the ear.[6] The mechanisms of TM damage in relation to blast wave direction were characterized using this model.

The goal of this study is to determine the relationships between the TM rupture threshold and blast wave directions. Both the experimental measurements and computational modeling of blast wave transduction from the ear canal to middle ear will provide important data for prediction of TM injury and hearing damage induced by blast exposure in the battlefield.

METHODS

Experimental Setup and Protocol

A “head block” attached with human cadaver ear or temporal bone and mounted with two pressure sensors has been developed in our lab to measure the transfer functions of the ear canal and middle ear in response to blast overpressure. In addition to two pressure sensors inside the ear, the third sensor is placed at the entrance of the ear canal. The three pressure sensors are simultaneously monitoring the blast pressure at the entrance of the ear canal (P0), near the TM in the canal (P1), and behind the TM in the middle ear (P2) as shown in Figure 1. The pressure sensor P0 (Model 102B16, PCB Piezotronics, Depew, NY) is placed at 1 cm lateral to the ear canal opening with the sensing surface facing the blast. The other two sensors P1 and P2 (Model 105C02, PCB Piezotronics) are placed at 3 mm from the TM in the canal and inside the middle ear cavity through the Eustachian tube, respectively. The P0 and P1 difference shows the transfer function of the ear canal in response to blast wave, and the difference between P0 and P2 or between P1 and P2 shows the middle ear transfer function or indicate how much sound pressure is transmitted into the middle ear in both time and frequency domains, respectively.

School of Aerospace and Mechanical Engineering, University of Oklahoma, 865 Asp Avenue, Norman, OK 73019

doi: 10.1093/milmed/usx149

The “head block” was exposed to open-field blast inside an anechoic test chamber along three directions: the vertical, horizontal, and front with respect to the head as shown in Figure 2. A total of 41 fresh human temporal bones (TBs) were used in this study for testing of three wave directions: from the top of the head – the vertical setup (13 TBs, donors’ average age 66.2 ± 6.6), from the lateral to the ear – horizontal setup (14 TBs, donors’ average age 64.5 ± 9.6), and from the front of the face – the front setup (14 TBs, donors’ average age 73.7 ± 7.1). The setups along these three directions with the pictures of head block are displayed in Figure 2. The TBs were obtained from Life Legacy Foundation, a certified human tissue supply source for military research. The study protocol was approved by the US Army Medical Research and Material Command Office of Research Protections.

All experiments on human TBs were performed in the Biomedical Engineering Laboratory at the University of Oklahoma. A well-controlled compressed air (nitrogen) – driven blast apparatus located inside an anechoic chamber was used to create a blast overpressure wave in this study.[5–7] Polycarbonate film (McMaster-Carr, Atlanta, GA, USA) of either 130 µm or 260 µm thick was employed to generate blast overpressure of at least 30 psi (207 kPa or 200 dB SPL). The overpressure level was controlled by varying the distance from the blast reference plane.

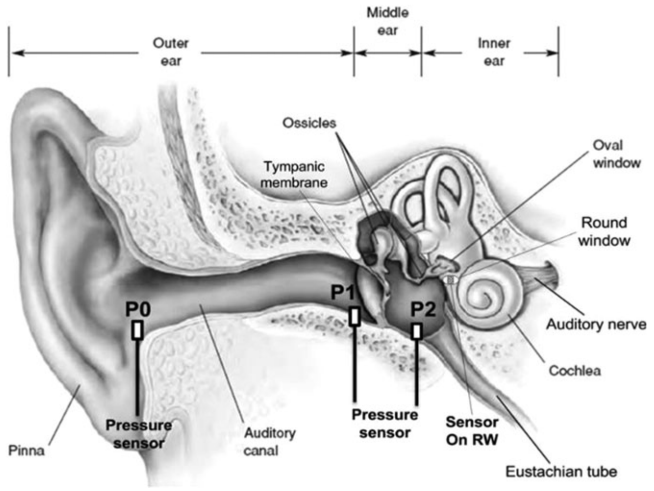

FIGURE 1. Schematic of simultaneously measuring blast overpressure transduction through the ear with three pressure sensors.

The pressure sensor signal was measured by cDAQ 7194 and A/D converter 9215 (National Instruments Inc., Austin, TX, USA) with the sampling rate of 100 k/s (10 µs dwell time). The LabVIEW software package (NI Inc.) was used for data acquisition and analysis. The waveform of each blast test was saved in a PC for further analysis.

It usually took three-to-four iterations of blast tests to reach the TM rupture threshold defined as the peak pressure before the TM rupture. That means if the TM ruptured after the third blast, the threshold was the peak pressure level of the second blast. The initial blast pressure level was selected based on the system calibration using different films and changing the distance between the sensor surface and the blast reference plane. The number of blast tests also varied with individual TBs due to the variation among the human samples and setups. To confirm the TM damage, an otoscopic examination of the ear was performed first and further verification was done using wideband tympanometry to determine whether the TM was ruptured.[5] When the TM was found without rupture, the next blast test was conducted with an increase of overpressure level. The testing stopped when the ear was ruptured. Note that the TM rupture threshold is a parameter to describe TM tissue damage in relation to the pressure force reaching the TM surface during blast exposure, which may not only depend on pressure level but also the exposure times before the rupture. However, in this study, the time interval between exposures was very short and the mechanical change of TM tissue in previous exposure was neglected.

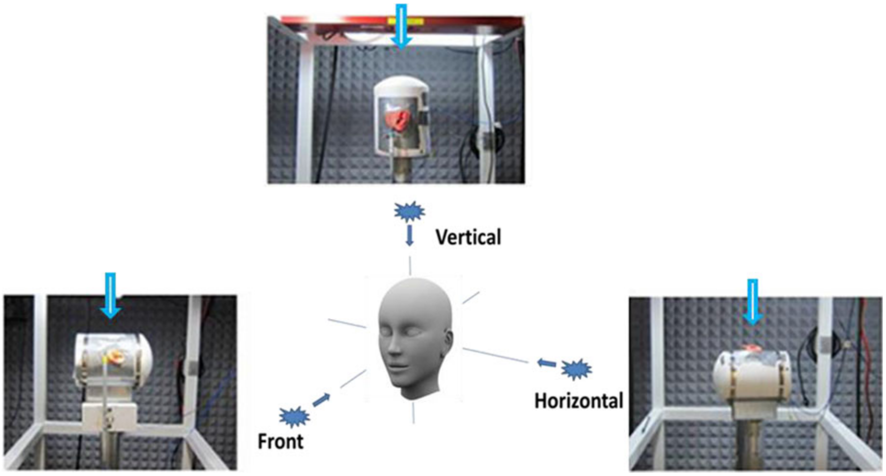

FIGURE 2. Schematic of three blast wave directions with respect to the head and the pictures of experimental setup with the head block along the vertical, horizontal, and front wave directions inside the test chamber. The blue arrow in each picture shows blast wave origination for the vertical, horizontal, and front setup test, respectively.

Waveform Analysis

Blast pressure energy spectra analysis on recorded waveforms (P0, P1, and P2) in the time domain was conducted in MATLAB to determine the signal energy distribution over the frequencies under three blast wave directions. First, the recorded pressure waveforms were converted to pressure distributions over the frequencies of 0.2–20 kHz by using FFT spectral analysis. Next, following the methods of impulse signal energy distribution theory reported by Gan et al,[5] the total sound exposure was divided by the standard characteristic impedance of the air ρc as impulse energy flux (energy per unit area) and expressed as:

$$E^* = \frac{1}{\rho c}\int_0^T p^2(t)\,dt, \qquad [\mathrm{J/m^2}] \tag{1}$$

where $p(t)$ is the instantaneous value of acoustic pressure in Pa or N/m^2, dt is the time increment for scanning of acoustic pressure in seconds, T is the duration of $P(t)$, and $\rho c = 406$ mks rayls to produce a quantity with units of energy flux (i.e., J/m^2). Both ρ and c are pressure-dependent in the shock front. The duration of $T = 6$ ms was used for calculation in the present study.

Eight octave band-pass filters with center frequencies at 125 Hz, 250 Hz, 500 Hz, 1 kHz, 2 kHz, 4 kHz, 8 kHz, and 16 kHz were designed. A low pass filter L125 and a high pass filter H16k were also designed to catch signals at frequencies lower than 125 Hz and higher than 16 kHz. The filtered signals were then generated and the sound energy in each band was calculated as the distribution of pressure energy flux over 10 bands. Instead of directly comparing the energy flux values in the three wave directions, the energy in each band was normalized with respect to the total sound energy in that band.

Finite Element Modeling

The 3D FE model of the human ear developed by Gan *et al*[8] for sound transmission and being used for TM perforation studies was employed to simulate the blast wave transmission through the ear as shown in Figure 3. The FE model consisted of the ear canal, TM, TM annulus (TMA), three ossicles connected by two joints: incudomelleolar joint (IMJ) and incudostapedial joint (ISJ), middle ear suspensory ligaments/muscle tendons, stapedial annular ligament (SAL), and the middle ear cavity. The cochlea was not included in this initial model, but the cochlear load was applied on the stapes footplate by a mass block-dashpot system with the cochlear input impedance of 20 GΩ.[8] The cochlear impedance was defined as the pressure per unit volume velocity of stapes footplate.

This FE model of the human ear was regenerated in ANSYS Workbench (ANSYS Inc., Canonsburg, PA, USA) where Fluent/ANSYS Mechanical coupled fluid–structure interaction analyses were employed to compute blast overpressure transduction from the environment to the TM and middle ear.[6] Briefly, the viscoelastic material properties were assigned to soft tissues in the middle ear including the TM, TMA, IMJ, ISJ, and SAL. The experimentally recorded P0 waveforms from the head block with cadaver TBs were applied onto the boundary at the entrance of the ear canal and the pressure waveforms P1 and P2 were then calculated and compared with those measured from the experiments. Note that the detailed description and validation of the FE model of the human ear for blast overpressure wave transduction can be found in Leckness' MS thesis (2016).[6]

The FE model was employed to investigate the mechanisms of TM injury under recorded P1 profiles from the vertical, horizontal, and front directions in this study. The P1 overpressure waveforms recorded from multiple iterations of blast tests in 14 temporal bones (four from the vertical direction and five from the horizontal and front directions) were applied to the surface of the TM in the FE model. The equivalent (von Mises) stress was used as a measure of the stress state of the TM and the maximum stress distributions on the TM were calculated. The sensitivity of TM stress with respect to P1 pressure increase, that is the TM stress gradient with respect to P1, $d\sigma/dP_1$, was then calculated from the model based on experimental P1 waveforms of pre-threshold

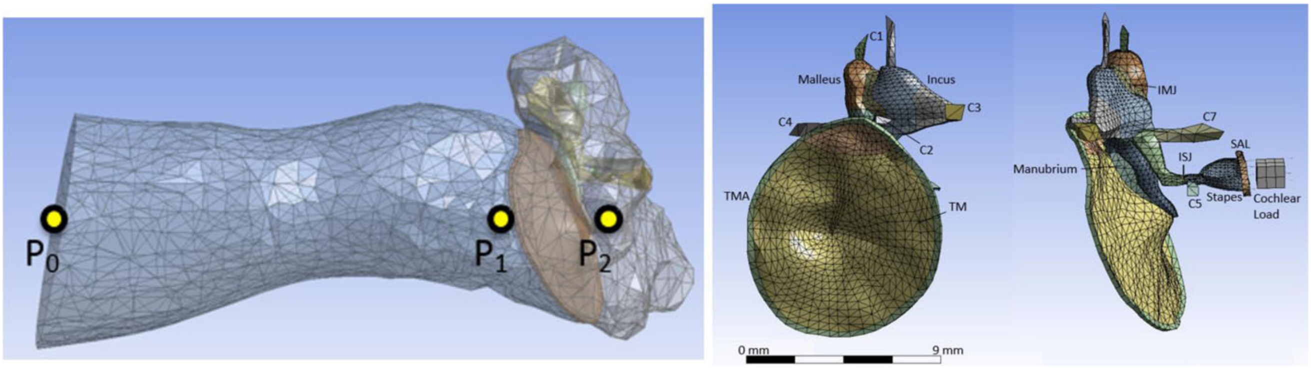

FIGURE 3. (Left) FE model of the human ear comprised of the ear canal, TM, middle ear ossicles, and middle ear cavity. The locations for pressure monitoring points are designated as P0, P1, and P2. (Right) Structural mesh of the model, showing the TM, TMA, middle ear ossicles, IMJ, ISJ, suspensory ligaments/muscle tendons (all Cs and SAL), and cochlear load.

up to rupture level. Usually two-to-four pressure waveforms per cadaver ear or temporal bone were involved in modeling calculation for $d\sigma/dP_1$.

RESULTS

Blast Experiment

Figure 4 shows typical overpressure waveforms of P0, P1, and P2 recorded from three cadaver ears in the vertical, horizontal, and front tests (before the TM rupture). The pressure waves are displayed in 2 ms of time duration and the positive overpressure is followed by negative pressure. As shown in Figure 4, the peak P0 level was around 50 kPa or 7.5 psi or 188 dB SPL for all three tests. The P1 peak pressure shows a substantial increase compared to the P0 pressure in all wave direction tests. The results demonstrate the ear canal effect on enhancing the impulse pressure level near the TM in the canal.

The otoscopic photos displayed in Figure 5 illustrate the TM damages observed at the vertical (V), horizontal (H), and front (F) tests with the peak P0 pressure level of 191, 186, and 189 dB SPL (or 11, 6, and 8 psi), respectively. There is no consistent TM rupture pattern observed from the experiments at different wave directions. However, in the most ruptured TM samples, the damage along the TM-radial fiber direction is observed, which is consistent with that the circumferential fibers of the TM have lower fracture strength and would break before the radial fibers. In some TM samples, the rupture area is near the manubrium or inferior side of the TM along the radial direction.

Table I lists the mean and standard deviation (SD) of P0, P1, P2, ratio of P1/P0 and the TM rupture P0 and P1 thresholds obtained from all tests along three blast wave directions: V, H, and F. The P1 rupture threshold was determined by multiplying the P1/P0 ratio and the P0 rupture threshold for each direction. The results in Table I show that the P0 rupture threshold for the V and F directions are comparable and that the P0 threshold in H-direction is significantly lower than the other two directions. Conversely, the P1/P0 ratio in H-direction is well above the others. It is also observed from Table I that the P1 rupture threshold (the pressure that is directly responsible for TM damage) is similar for the V and H directions, at 20.2 and 20.1 psi, respectively. Interestingly, the results indicate that the F direction requires less pressure as measured at P1 to rupture the TM.

Waveform Analysis

Figure 6 displays the comparison of impulse energy flux (energy per unit area in unit J/m^2) distributed in 10 frequency bands from the below 125 Hz to over 16 kHz obtained from waveforms recorded in three wave direction tests. The results demonstrate that (1) P0 pressure-induced energy is mainly distributed at frequencies below 1 kHz and there is a large peak for V direction at 500 Hz as shown in Fig. 6A; (2) P1 pressure-induced energy is distributed mainly at frequencies up to 4 kHz as shown in Fig. 6B; and (3) blast waves at F and H directions

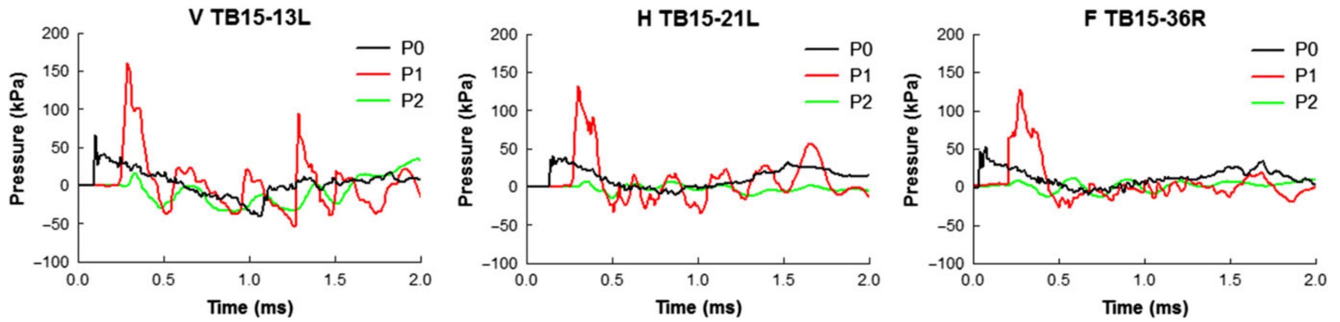

FIGURE 4. Overpressure waveforms of P0 (black), P1 (red), and P2 (green) recorded from three cadaver ears or temporal bones under the vertical (V, left), horizontal (H, medium), and front (F, right) tests. TB15-13L, TB15-21L, and TB15-36R represent the temporal bone (TB) samples.

FIGURE 5. Otoscopic pictures of human TMs ruptured after blast exposure. (A) Vertical test, left ear, TM ruptured in the superior-posterior region; (B) horizontal tests, left ear, TM ruptured in the inferior side; (C) front test, right ear, TM ruptured in the superior-posterior region.

TABLE I. Mean and SD of Peak Pressure Values P0, P1, and P2, Ratio of P1/P0 and the TM Rupture P0 and P1 Thresholds

Blast Wave Direction	TB Sample	P0 (psi)	P1 (psi)	P2 (psi)	P1/P0	Threshold P0 (psi)	Threshold P1 (psi)
Vertical	Mean ± SD (*N* = 13)	8.9 ± 1.8	19.3 ± 3.3	2.3 ± 1.6	2.2 ± 0.5	9.2 ± 1.7	20.2 ± 2.2
Horizontal	Mean ± SD (*N* = 14)	6.4 ± 2.1	19.0 ± 6.1	2.2 ± 1.4	3.0 ± 0.7	6.7 ± 1.2	20.1 ± 1.9
Front	Mean ± SD (*N* = 14)	9.8 ± 2.0	16.3 ± 3.3	2.1 ± 0.7	1.7 ± 0.4	9.8 ± 2.1	16.7 ± 2.5

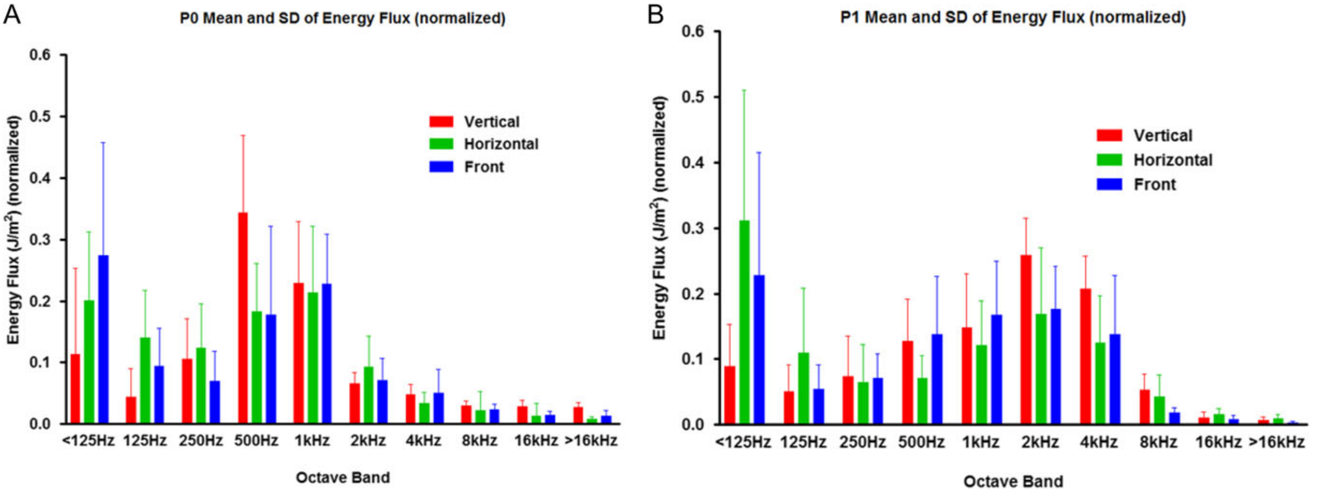

FIGURE 6. Comparison of normalized energy flux over 10 octave bands from below 125 Hz to above 16 kHz between the waveforms recorded in vertical, horizontal, and front tests. (A) Mean and SD of energy flux for P0 waveforms; (B) mean and SD of energy flux for P1 waveforms.

result in relatively large energy flux of both P0 and P1 at frequencies below 125 Hz.

FE Modeling

The average maximum stresses induced by the P1 rupture threshold waveforms were 16.2 ± 3.0, 16.3 ± 2.4, and 14.3 ± 2.5 MPa for the vertical, horizontal, and front directions, respectively. The average maximum stresses induced by the P1 waveforms that caused visible TM damage were 20.3 ± 1.2, 18.8 ± 2.0, and 15.5 ± 3.5 MPa for the vertical, horizontal, and front directions, respectively. An example of TM stress distribution at the time of maximum stress due to an applied P1 waveform of 134 kPa maximum pressure is displayed in Figure 7. As shown in this figure, the maximum stress reached 16 MPa and the regions of highest stress were along the anterior portion of the TMA, the posterior to the center of the manubrium, and the inferior to the bottom of the manubrium. These locations may indicate potential sites for TM rupture.

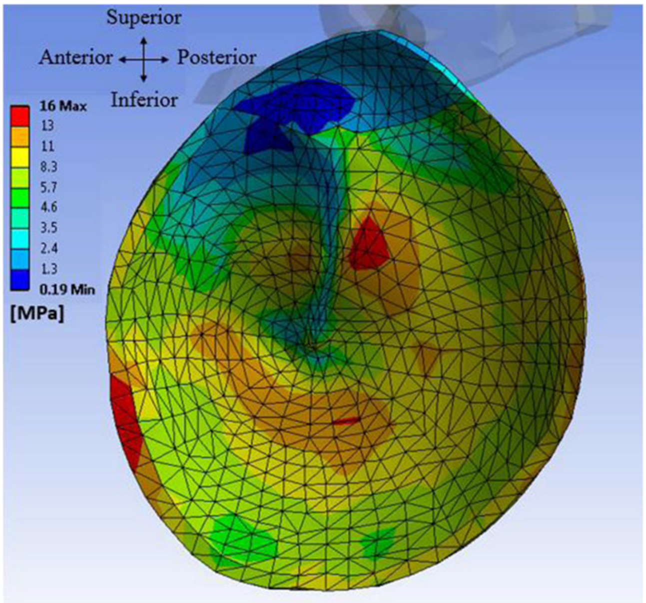

FIGURE 7. FE model-derived distribution of the equivalent (von Mises) stress in the TM when the maximum stress was reached under the vertical wave direction.

To understand the mechanism behind the experimental findings, the sensitivity of TM stress with respect to P1 pressure increase as the TM stress gradient with respect to P1, $d\sigma/dP_1$, were calculated from the four cadaver ears at the V direction test and five at the H and F direction tests, respectively. As an example, Figure 8A–C show a series of P1 pressure waveforms over 0.5 ms duration from three temporal bone experiments in V, H, and F direction test, respectively. The P1 waveforms recorded from 3 to 4 blasts to reach TM rupture were used to calculate $d\sigma/dP_1$ in V, H, and F directions using the model.

All the data points of the maximum stress in the TM vs. the maximum (peak) P1 pressure obtained along the V, H,

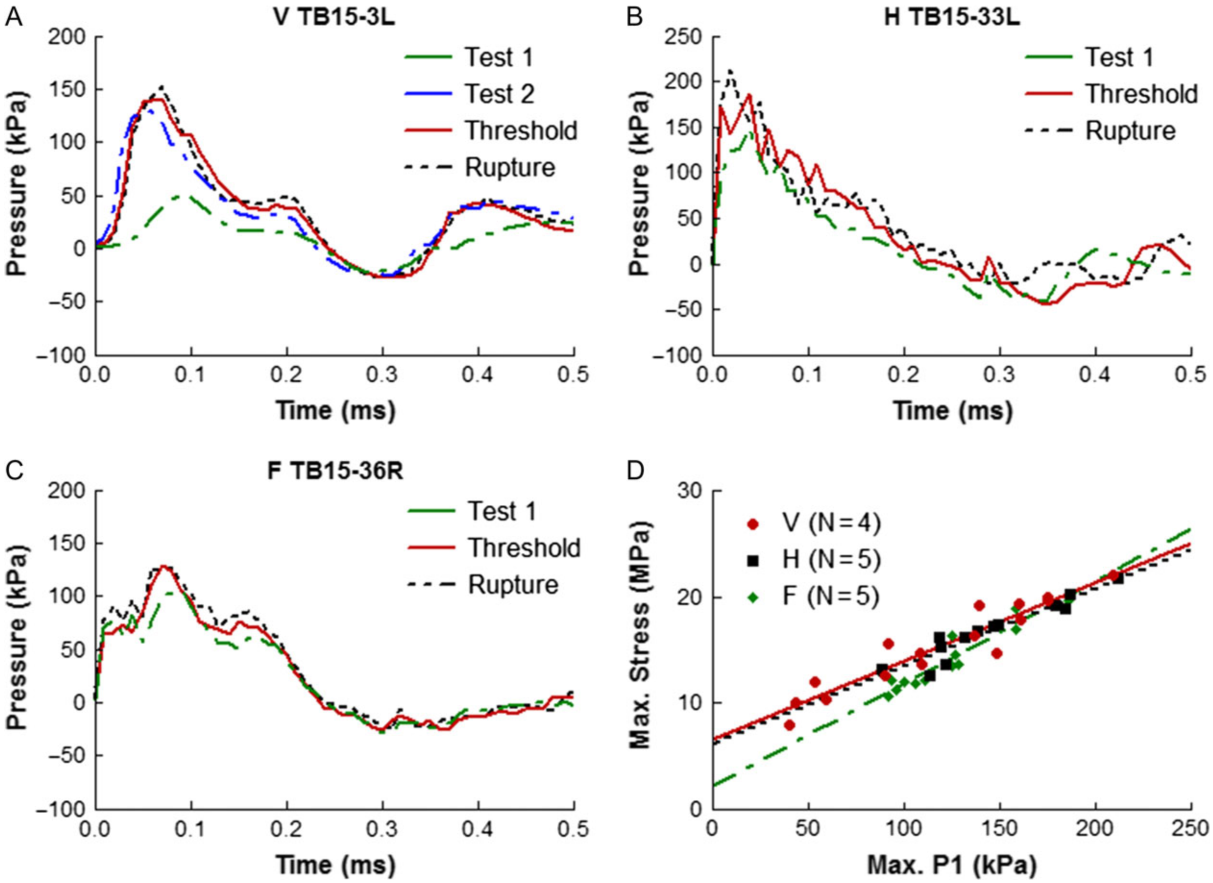

FIGURE 8. (A), (B), and (C) represent the P1 pressure waveforms with incremental peak pressure level from initial test 1 to TM rupture recorded from a temporal bone sample TB15-3L in V direction test, from sample TB15-33L in H-direction test, and from sample TB15-36R in F direction test, respectively. (D) Plots of FE model-derived maximum stress in the TM vs. P1 peak pressure obtained from V direction ($N = 4$), H direction ($N = 5$), and F direction ($N = 5$).

and F blast direction tests were plotted in Figure 8D. Statistical correlation was then applied to determine the best-fit line for the data points at each direction. Figure 8D shows the comparison of the slope (i.e., stress gradient) $d\sigma/dP_1$ at three directions. The mean value of stress gradient with respect to pressure P1 was calculated as 74.1, 73.0, and 96.7 for V, H, and F direction, respectively.

DISCUSSION

Mechanisms of TM Rupture in Relation to Blast Wave Direction

The energy analysis results shown in Figure 6 suggest that P1 pressure waveform should be considered as a primary factor for blast-induced TM damage because P1 energy distributions on octave bands are similar for all three wave directions and concentrated from 500 Hz to 4 kHz. Moreover, the P1 pressure is measured near the TM which represents the pressure force reaching the TM surface during blast exposure. Thus, the P1 threshold for TM damage is more accurately represent the pressure applied to the TM than the P0 threshold. The experimental results shown in Table I indicate that P1 threshold in F direction is lower than V and H directions, or in other words, the blast wave from front of the face (F direction) is easier to cause TM rupture than other blast wave directions. Now the question is: why does the front direction of blast wave result in a lower P1 threshold for TM damage?

To answer this question and understand the mechanism behind the experimental findings, the FE model of the human ear was used to compute the distributions of the stress in the TM and derive the sensitivity of TM stress with respect to P1 pressure increase as the TM stress gradient with respect to P1, $d\sigma/dP_1$. The results shown in Figure 8 indicate that the change of maximum stress in the TM with respect to P1 peak pressure increase in the front direction is higher than other two directions. The high sensitivity of TM stress with respect to the P1 pressure in front setup, or the blast wave coming to the face, may characterize mechanical damage of the TM induced by blast. The average maximum stress was lowest for the front direction, as was the average P1 rupture threshold; this suggests that neither stress level nor P1 level alone determines TM failure, but that TM failure is best predicted by the rate change of stress with respect to maximum P1 pressure reaching the TM.

This finding agrees with the study reported in chinchilla TM damage by Gan *et al.*[5] The variation of TM stress in chinchilla ear with respect to blast overpressure level showed obvious difference between the open and shielded exposures in Gan's paper (Figure 10 of that paper). The rapid change of stress σ to the pressure loading p, or the higher $d\sigma/dp$ value in shielded case than the open case, resulted in a lower threshold of TM rupture in chinchilla blast experiments. The present study in human TM damage during the blast exposure also shows that the rate of stress change with respect to the overpressure loading is a parameter to characterize TM tissue damage caused during the blast exposure.

Additional Insight from This Work

This is the first time the TM damage in relation to blast overpressure wave direction has been investigated using the human cadaver ears and 3D FE model of the human ear. The available studies in the literature on the effect of blast direction on tissue injury are mainly in the areas of brain responses to different blast or impact directions using the computational modeling approach. For example, a recent study by Sarvghad-Moghaddam *et al*[9] reported their FE analysis of the human head model with the helmet and faceshield under three blast wave directions: the front, back, and side of the head. The calculated intracranial pressure and the maximum shear stress were used as the major injury predictors for evaluation of helmet and faceshield protections. Sarvghad-Moghaddam *et al* found that the underwash incidence overpressure greatly changed with the blast direction. However, the main limitation of their study and probably similar blast-head interaction studies is lack of validation of the head model against blast loads as stated in their paper.

Compared with the published works in head injury in relation to blast direction, the present study includes both the experimental tests in human cadaver ears and the FE modeling of the TM maximum stress increasing with blast pressure loads. The results and findings from this study have general contributions for providing the TM rupture threshold data and the mechanisms of TM damage during blast exposure. The results reported in this paper can be used in clinics for understanding or explaining the TM damage in relation to blast exposure for military Service members regarding their specific experiences in the battlefield. However, there are still many questions to be answered, including the TM damage after repetitive blast exposures and the relationship between the mechanical injuries of the TM and the cochlear damage during blast exposure. The investigation along this direction on mechanisms of the TM and other ear tissue damages in relation to blast overpressure waveforms is needed for development of the failure criteria for TM, a multiple layer, viscoelastic membrane tissue, in response to blast overpressure.

CONCLUSIONS

The relationship between the TM damage threshold and blast overpressure wave direction has been investigated in human cadaver ears or temporal bones and the FE model of the human ear. The "head block" attached with the temporal bone was exposed to open-field blast inside the test chamber at three incident wave directions: vertical, horizontal, and front with respect to the head. Results demonstrate that blast overpressure P0 at the ear canal entrance induced the highest peak pressure P1 near the TM in the canal, which determines the TM injury. The P1 pressure differences in vertical, horizontal, and front tests reflect the variations of energy flux distribution over frequencies, peak P1/P0 ratio, and TM rupture threshold. FE modeling results indicate that P1 threshold for TM rupture in front direction is the lowest because of the highest TM stress change rate with respect to P1 pressure increase, $\delta\sigma/\delta p_1$, compared with the vertical and horizontal directions.

PRESENTATIONS

Presented in a breakout session entitled "The Role of Medical Research in Blast Injury" at the 2016 Military Health System Research Symposium. (Abstract number: MHSRS-16-0405).

FUNDING

This work was supported by U.S. Army Medical Research and Material Command (USAMRMC) Military Operational Medicine Research Program, Contract No. W81XWH-14-1-0028.

REFERENCES

1. Helfer TM, Jordan NN, Lee RB: Postdeployment hearing loss in U.S. Army soldiers seen at audiology clinics from April 1, 2003, through March 31, 2004. Am J Audiol 2005; 14: 161–8.
2. Cave KM, Cornish EM, Chandler DW: Blast injury of the ear: clinical update from the global war on terror. J Mil Med 2007; 172(7): 726–30.
3. Cho S-I, Gao SS, Xia A, et al: Mechanisms of hearing loss after blast injury to the ear. PLoS One 2013; 8(7): e67618.
4. Fausti SA, Wilmington DJ, Gallun FJ, Myers PJ, Henry JA: Auditory and vestibular dysfunction associated with blast-related traumatic brain injury. J Rehabil Res Dev 2009; 46(6): 797–810.
5. Gan RZ, Nakmali D, Ji X, Leckness K, Yokell Z: Mechanical damage of tympanic membrane in relation to impulse pressure waveform - a study in chinchillas. Hearing Res 2016; 340: 25–34.
6. Leckness K: Novel finite element method to predict blast wave transmission through human ear. Thesis for Master Degree in Biomedical Engineering at University of Oklahoma, August 2016. Avialable at http://hdl.handle.net/11244/44932; accessed December 30, 2016.
7. Hawa T, Gan RZ: Pressure distribution in a simplified human ear model for the high intensity sound transmission. J Fluids Eng 2014; 136(11): 111108-1–6.
8. Gan RZ, Cheng T, Dai C, Yang F, Wood MW: Finite element modeling of sound transmission with perforations of tympanic membrane. J Acoust Soc Am 2009; 126(1): 243–53.
9. Sarvghad-Moghaddam H, Rezaei A, Ziejewski M, Karami G: Evaluation of brain tissue responses because of the underwash overpressure of helmet and faceshield under blast loading. Int J Numer Mechod Biomed Eng 2017; e02782: 1–13.

MILITARY MEDICINE, 183, 3/4:262, 2018

Computational Modeling of Blast Wave Transmission Through Human Ear

Kegan Leckness, MS; Don Nakmali, MS; Rong Z. Gan, PhD

ABSTRACT Hearing loss has become the most common disability among veterans. Understanding how blast waves propagate through the human ear is a necessary step in the development of effective hearing protection devices (HPDs). This article presents the first 3D finite element (FE) model of the human ear to simulate blast wave transmission through the ear. The 3D FE model of the human ear consisting of the ear canal, tympanic membrane, ossicular chain, and middle ear cavity was imported into ANSYS Workbench for coupled fluid–structure interaction analysis in the time domain. Blast pressure waveforms recorded external to the ear in human cadaver temporal bone tests were applied at the entrance of the ear canal in the model. The pressure waveforms near the tympanic membrane (TM) in the canal (P1) and behind the TM in the middle ear cavity (P2) were calculated. The model-predicted results were then compared with measured P1 and P2 waveforms recorded in human cadaver ears during blast tests. Results show that the model-derived P1 waveforms were in an agreement with the experimentally recorded waveforms with statistic Kurtosis analysis. The FE model will be used for the evaluation of HPDs in future studies.

INTRODUCTION

Hearing loss is the most common disability among veterans, and is often caused by exposure to high-intensity sound or blast overpressure waves that are considered to be an intrinsic eventuality faced by military personnel involved in most operational activities. Blast overpressure is a high-intensity disturbance in the ambient air pressure that is characterized by an intense impulse sound wave of over 170 dB sound pressure level (SPL).[1] When exposed to a blast, the human auditory system is vulnerable to both peripheral and central damage from the overpressure.[2,3]

In a previous study by Gan et al,[4] the experimental measurement and finite element (FE) modeling methods were used to investigate blast-wave-induced tympanic membrane (TM) rupture in two cases in chinchillas: the open-field and shielded cases. Eighteen animals were tested under two cases (nine for each) and the stainless steel cup was used as a shield. A compressed nitrogen-driven blast apparatus located inside an anechoic chamber in the Biomedical Engineering Laboratory at the University of Oklahoma was used to generate blast overpressure. The resulting waveforms were then recorded and TM rupture was observed. Driven by experimentally measured pressure waveforms, the FE model of the chinchilla middle ear[5] was used to develop the stress distributions in the TM for the open-field and shielded cases. The stress gradients with respect to the maximum incident pressure were then derived to explain why the shielded chinchillas' TMs ruptured at much lower pressure levels than those without a shield.

In this article, we report our recently developed three-dimensional (3D) FE model of the human ear to simulate blast wave transmission through the ear. The purpose of this study is to provide a 3D computational model for the improvement of current auditory hazard assessment models and for a better understanding of blast wave transmission through the human ear.

A 3D human ear model published by Gan et al[6] consisting of the ear canal, TM, ossicular chain, and middle ear cavity was used in this study. Fluent/ANSYS Mechanical coupled fluid–structure interaction (FSI) analyses were employed to compute blast overpressure transduction from the environment to the TM and middle ear. Fresh human cadaver temporal bones (TBs) with all soft tissue intacts were subjected to blast exposures from three directions (vertical, horizontal, and front) inside the test chamber. The pressures at the ear canal entrance (P0), near the TM in the canal (P1), and behind the TM in the middle ear cavity (P2) were simultaneously monitored. The P0 waveforms measured in cadaver ears were applied at the entrance of the ear canal of the FE model. The P1 and P2 pressures were calculated from the model. The model-derived results were compared with experimentally measured P1 and P2 waveforms from human cadaver ears. The comparisons show that the FE model of the human ear is able to predict blast overpressure transmission through the ear canal into the middle ear. The model will be used for the evaluation of hearing protection devices (HPDs) in future studies.

METHODS

FE Model

Human ear FE model geometry built on a set of histological cross-sectional images of a human TB reported by Gan et al[6] was remeshed in HyperMesh 12 (Altair Engineering, Inc.,

---

School of Aerospace and Mechanical Engineering, University of Oklahoma, 865 Asp Avenue, Norman, OK 73019.

doi: 10.1093/milmed/usx226

Troy, MI, USA) using tetrahedral and wedge elements. The model consists of the ear canal, TM (pars flaccida and pars tensa), TM annulus (TMA), manubrium, ossicles and associated suspensory ligaments, incudo-malleolar joint (IMJ), incudostapedial joint (ISJ), and stapedial annular ligament (SAL). The middle ear structures, ear canal, and middle ear cavity consist of 8,043, 13,805, and 11,884 elements, respectively.

The entire model (Fig. 1) was then imported into the ANSYS Workbench v16.1 (ANSYS Inc., Canonsburg, PA, USA) environment where the strongly coupled FSI analysis method was developed. The structural calculations were carried out in ANSYS Mechanical. Linear viscoelastic material properties reported by Zhang and Gan[7] were assigned to the middle ear soft tissues including the TM, TMA, IMJ, ISJ, and SAL. The manubrium, ossicles, and suspensory ligaments were presented as elastic materials as reported by Gan et al.[6] The TMA, SAL, and ends of the suspensory ligaments where they meet the bony wall were given fixed boundary conditions. As the cochlea was not included in this initial model, its damping effect on stapes footplate motion was modeled by introducing a mass block-dashpot system, with parameters adjusted to reflect the cochlear input impedance of 20 GΩ.[8] The middle ear structures were assumed to react to the oncoming blast wave passively, and so the only loads acting on the structures were transferred via fluid–structure interface applied to both sides of the TM. The FSI between the ossicular chain and middle ear cavity fluid (air) was considered negligible and was not included in this study.

The computational fluid dynamics (CFD) software Fluent was used to determine the air pressure propagation through the ear canal and middle ear cavity. Computational fluid dynamics packages have been shown to be useful in the prediction of blast wave dynamics[9] and Fluent, specifically, has been implemented in impulsive flow studies.[10] Fluent utilizes the finite volume method to numerically solve the equations of mass, momentum, and energy conservation and the equation of state. Standard compressible air properties were employed and the operating pressure was set to ambient air pressure at sea level, or 101,325 Pa and the gravitational effects were neglected. The walls of the canal and middle ear cavity were defined as rigid and a no-slip boundary condition was applied. Fluid–structure interactions were prescribed to the boundaries of the fluid domains coincident with the surfaces of the TM. Experimentally measured P0 pressure profiles from TB tests were applied directly onto the boundary at the entrance of the canal as a pressure inlet. The pressure waveforms at P1 and P2 were calculated. To keep the fluid meshes' cell quality sufficient for convergence under large TM deformation, a dynamic smoothing and remeshing scheme was employed. The FE modeling results included the pressure distribution throughout the fluid domains (ear canal and middle ear cavity) and the associated structural response.

Blast Test with Cadaver Ears

Human cadaveric temporal bones with intact pinna, TM, and ossicular chain were mounted to a specifically designed "head block" inside the blast chamber as shown in Figure 2A (setup for vertical exposure). The temporal bones were divided into three groups to test the blast direction effect: the vertical, horizontal, and front directions (Fig. 2B). A compressed nitrogen-driven blast apparatus was used to mimic blast exposure in this study. Polycarbonate film of varying thicknesses (130 μm or 260 μm) was employed as a diaphragm under compressed nitrogen, the rupture of which generated blast overpressure of at least 207 kPa (30 psi or 200 dB SPL). Overpressure level at the canal entrance was controlled by varying the distance of the head block from the blast reference plane.

A pressure sensor (Model 102B16; PCB Piezotronics, Depew, NY, USA) was placed at the entrance of the ear canal (approximately 1 cm off the center of the ear canal opening) to monitor the overpressure waveform entering the ear canal (P0). Two holes were drilled into the temporal bone for the insertion of additional pressure sensors. These additional sensors were inserted to measure P1 and P2. The P1 and P2 sensors (Model 105C02; PCB Piezotronics) were placed at 3 mm from the TM in the ear canal and inside the middle ear cavity through the Eustachian tube, respectively. The pressure sensor signal was measured by cDAQ 7194 and A/D converter 9215 (National Instruments Inc., Austin, TX, USA) with the sampling rate of 100 k/s (10 μs dwell time). The LabVIEW software package (NI Inc.) was used for data acquisition and analysis. The

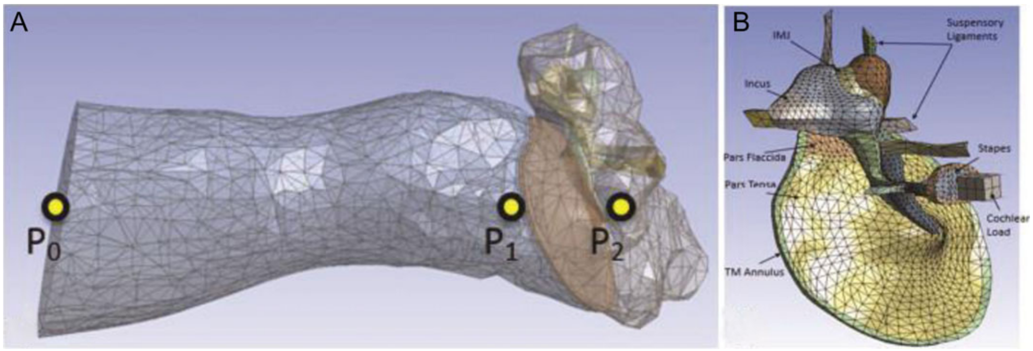

FIGURE 1. (A) Finite element model of the human ear including ear canal, middle ear cavity, and middle ear structures. Shows the pressure monitor locations P0, P1, and P2 as they exist in the model. (B) The middle ear structures isolated.

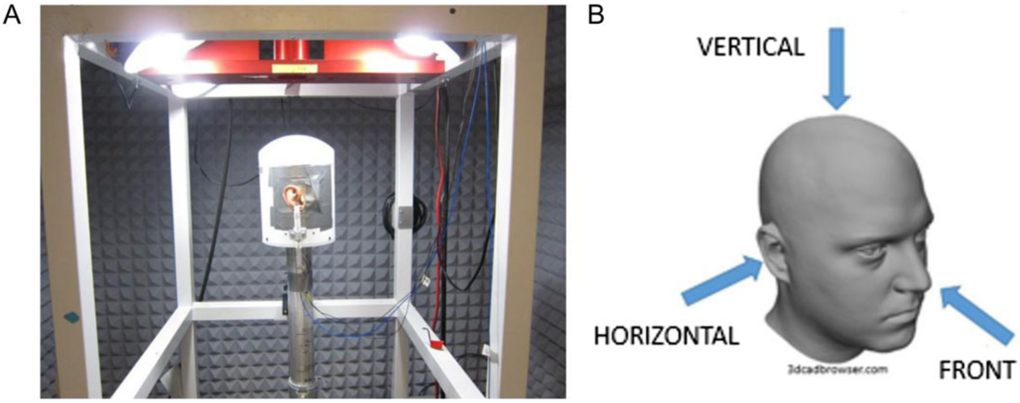

FIGURE 2. (A) Cadaver temporal bone mounted on head block under blast apparatus in blast chamber. Shows vertical exposure setup. (B) Display of blast exposure directions.

waveform of each blast test was then saved for further analysis. Note that the sampling rate is sufficient for the waveform recorded in this study.

Comparison of Model Data with Experimental Results

The 3D FE model-predicted pressure waveforms were compared with those measured in cadaver ears during experiments. The P1 pressure waveforms were the most important because this is the pressure directly responsible for TM damage and ossicular chain motion. Three metrics of the P1 waveforms in the time domain were considered for comparison: peak pressure level, A-duration, and Kurtosis. These three parameters describe the P1 waveforms from different aspects. The peak pressure P1 represents the intensity of blast overpressure reaching the TM; the A-duration is defined as the measure of time (in ms) that the positive portion of the peak pressure is sustained and describes the shape of the P1 peak wave; Kurtosis is the statistics measure of impulse pressure wave shape to compare two P1 waveforms: recorded from the experiment and derived from the FE model. Note that Kurtosis analysis has been used for prediction of human hearing loss in impulsive noise environment.[11–13] In this study, however, the statistic Kurtosis was only employed to compare two P1 waveforms for validation of the FE model. During the calculation, 1 ms of the P1 pressure profile was enough to assess the characteristics of the waveform.

Via FFT analysis, the impulse pressure spectra were then obtained from the experimental and predicted P1 waveforms to derive the energy spectra in the frequency domain. Next, following the methods of impulse signal energy distribution theory reported by Gan et al,[4] the total sound exposure was divided by the standard characteristic impedance of the air ρc as impulse energy flux (energy per unit area) and expressed as:

$$E^* = \frac{1}{\rho c}\int_0^T p^2(t)\,dt,\ \ [\mathrm{J/m^2}]$$

where $p(t)$ is the instantaneous value of acoustic pressure in Pa, dt is the time increment for scanning of acoustic pressure in seconds, and $\rho c = 406$ mks rayls to produce the quantity with units of energy flux (i.e., J/m^2). Both ρ and c are pressure-dependent in the shock front. The duration $T = 6$ ms was used for calculation in the current study.

Eight octave band-pass filters with center frequencies at 125 Hz (88–177), 250 Hz (177–354), 500 Hz (354–707), 1 kHz (0.707–1.414), 2 kHz (1.414–2.828), 4 kHz (2.828–5.657), 8 kHz (5.657–11.314), and 16 kHz (11.314–22.627) were designed. To catch signals at frequencies lower than 125 Hz and higher than 16 kHz, additional low-pass (L125, cutoff at 88 Hz) and high-pass (H16k, cutoff at 22.627 kHz) filters were designed. The MATLAB SPTOOL was used to create all the filters with IIR (infinite impulse response) Butterworth filter with 6 order, signal sample rate Fs = 100,000. The impulse pressure spectra were filtered and the sound energy in each band was calculated as the distribution of pressure energy flux over 10 bands. The energy in each band was normalized with respect to the total sound energy in that band, and the resulting energy fluxes of the experimental and predicted waveforms were compared.

RESULTS

The experimentally measured and FE model-predicted pressure waveforms for the vertical, horizontal, and front blast directions are shown in Figure 3A and B, respectively. The peak pressure level of waveforms (P0) ranged from approximately 50 kPa to 80 kPa across the incident wave directions of vertical, horizontal, and front, and the A-duration for P0 waveforms ranged from approximately 0.5 ms to 1.0 ms. Note that in the experiment, the P0 sensor was placed 1 cm lateral to the canal entrance, but in the model, the P0 waveform was applied directly at the canal entrance; this resulted in experimental P1 response times (the time it takes for P1 to respond after initial P0 response) that were longer than those predicted by the model. As can be seen when comparing the P0 and P1 waveforms

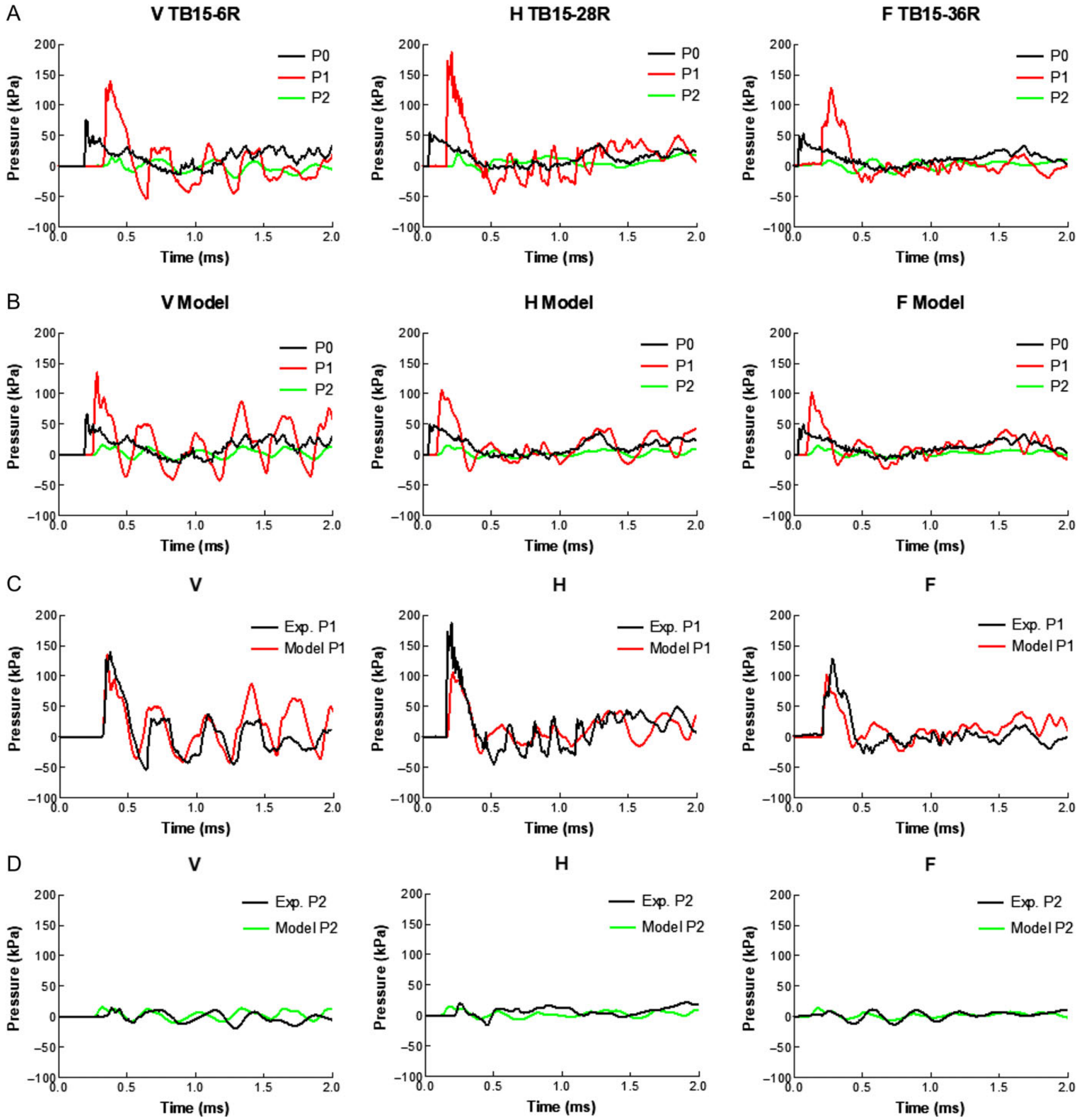

FIGURE 3. (A) Experimental recordings of the P0, P1, and P2 waveforms from vertical, horizontal, and front blast exposures. (B) Predicted P1 and P2 waveforms induced by experimental P0 waveforms from each blast direction. (C) Comparison of experimental and model-predicted P1 waveforms from each blast direction. (D) Comparison of experimental and model-predicted P2 waveforms from each blast direction.

in Figure 3A, the pressure magnitude increases significantly by the time the wave has reached the TM; the model captures this behavior. The peak pressure ratios, P1:P0, of the experimental vs. predicted waveforms were 1.83 vs. 1.78, 3.37 vs. 2.72, and 2.42 vs. 1.92 for the vertical, horizontal, and front directions, respectively. The experimental and model-derived P1 waveforms from each direction are compared in Figure 3C, accounting for the difference in P1 response time. Qualitatively, the three predicted P1 pressure profiles agree quite well with the experimental waveforms. Figure 3D shows the comparison of P2 pressure waveforms recorded from experiments and derived from the model in V, H, and F direction, respectively. As shown in this figure, the P2 waves are no longer as the impulse pressure profiles and the peak-to-peak pressure values are lower than

20 kPa or lower than 20% of P1 peak pressure value. The experimental and modeling results overlap each other, which indicates the model is also able to predict P2 pressure. However, as pointed at the beginning of the 3rd Section under 'Methods' that it is important to understand P1 waveform behavior since it is the pressure that acts directly on the TM.

Table I lists the three quantitative metrics by which the experimental and model-derived P1 waveforms were evaluated and compared in peak pressure level, A-duration, and 1 ms kurtosis. Percent error calculations were performed to assess the FE model's predictability. The model-predicted percent errors in the peak pressure level, A-duration, and 1 ms kurtosis were found to be 3.0%, 9.1%, and 15%; 25%, 17%, and 1.0%; and 20%, 13%, and 9.8% for the vertical, horizontal, and front blast directions, respectively.

Obtained from FFT analysis, the spectral behavior of the vertical P1 waveforms (sample TB15-6R) in Figure 3C is displayed for comparison in Figure 4A. These data were utilized to perform the energy flux analysis over 10 octave bands in Figure 4B. Note that the data were normalized with respect to the total signal energy and the total value was 1.0. Also note that the P0 waveform applied as input to the FE model was taken from the experiment, and so the energy flux for the experimental and predicted P0 is the same for all octave bands. The majority of the experimental P1 energy flux is in the 2 kHz and 4 kHz octave bands, peaking around 0.3 J/m^2 in the 2 kHz band. The majority of the energy flux determined from the model-derived P1 pressure spectra was also concentrated in the 2 kHz and 4 kHz octave bands, with a maximum at 4 kHz. The results demonstrate that the model is capable of predicting which frequencies the majority of P1 energy flux occupies.

Figure 5 displays the displacement (Fig. 5A) and stress distributions (Fig. 5B) plotted onto the TM at the time maximum displacement or maximum stress occurred, for the vertical exposure. The maximum TM deformation of 1.4 mm occurs approximately 2 mm inferior and anterior to the umbo. The stress contours indicate maximum stresses at three locations on the TM (the anterior TMA, inferior to the umbo, and posterior to the manubrium) and may indicate possible locations prone to TM rupture. Structural stress, strain rates, and displacement distributions may be implemented in analyses of all modeled middle ear structures.

DISCUSSION

The peak pressure metric showed the most variability when quantitatively comparing experimental and model-predicted P1 waveforms, with percent error ranging from 3.0% in the

TABLE I. List of P1 Waveform Metric Data from Experiment and FE Model at Vertical (V), Horizontal (H), and Front (F) Wave Directions.

ID		P1	Peak (kPa)	Peak (dB SPL)	A-Duration (ms)	Kurtosis (1 ms)
V	TB15-6R	Experiment	139.3	196.9	0.22	3.85
		Model	135.1	196.6	0.20	3.28
H	TB15-28R	Experiment	187.1	199.4	0.24	5.54
		Model	139.8	196.9	0.20	5.50
F	TB15-36R	Experiment	128.4	196.2	0.23	4.48
		Model	102.3	194.2	0.20	4.92

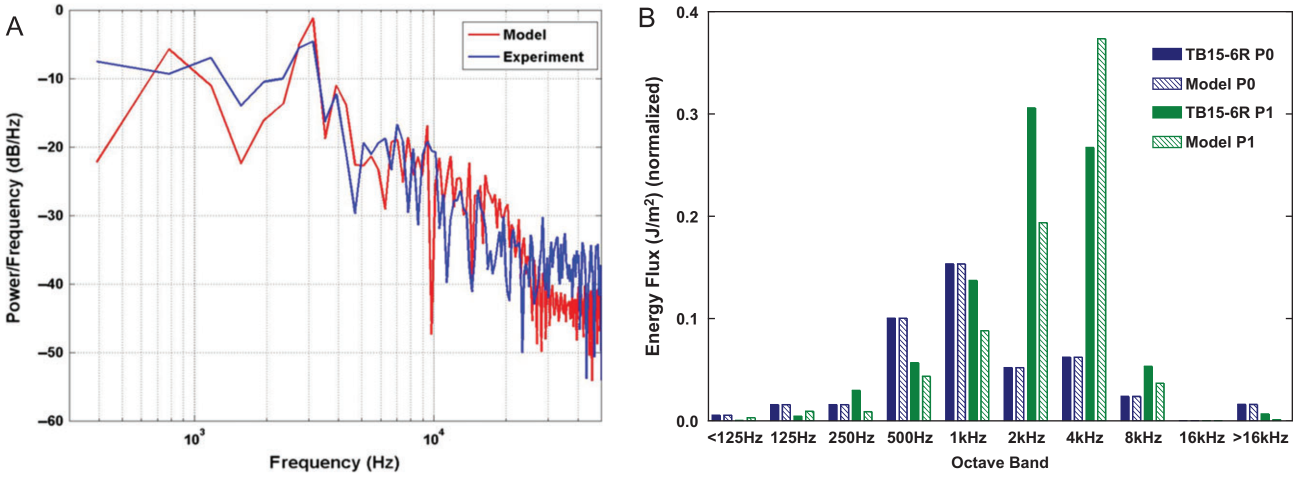

FIGURE 4. (A) Spectral behavior of the model-predicted and experimentally measured P1 waveforms from vertical blast exposure. (B) Comparison of the normalized energy flux distributions of model-predicted and experimental P0 (blue) and P1 (green) waveforms.

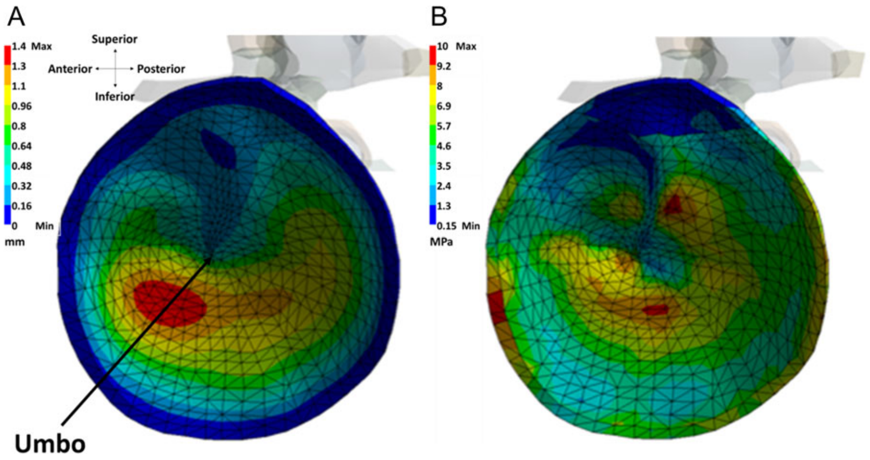

FIGURE 5. (A) TM displacement distribution at the time of maximum displacement for vertical exposure. TM is fixed to the bony wall along its annulus and experiences a maximum displacement of 1.4 mm approximately 2 mm inferior and anterior to the umbo. (B) TM stress distribution at the time of maximum stress. Displays three stress concentrations indicating possible locations for TM rupture.

vertical direction to 25% in the horizontal direction. This variability may be due to the entrance velocity effect. In experiments with three incident wave directions, the blast wave front enters the ear canal at different rates because of the orientation of the ear canal with respect to wave front. It is possible that the effects of ear canal geometry on overpressure amplification (P1/P0) are magnified due to a higher entrance velocity in the horizontal orientation (in which the ear canal is parallel to the wave front). Future blast experiments designed to measure the velocity at the ear canal entrance may provide additional data that will allow for more accurate modeling of the initial conditions of the blast wave propagation.

The percent error in the model-predicted P1 A-duration metric ranged from 9.1% to 17% for the vertical and horizontal directions, respectively. Interestingly, the predicted P1 A-durations were determined to be 0.2 ms for all directions, suggesting that A-duration near the TM is a function of ear canal geometry. The best-predicted metric was 1 ms kurtosis, ranging from 1.0% to 15% error for the horizontal and vertical directions, respectively. These results demonstrate that the statistic Kurtosis method used in this study has fulfilled the quantitative comparison of two signal shape measurements or waveforms, one from the experiments and one from the model.

The model-predicted P1 energy flux was in general agreement with the experimental energy flux, both showing the pressure spectra being concentrated in the 2 kHz and 4 kHz octave bands. The shift of the predicted P1 pressure spectra to higher frequencies may be attributed to ear canal geometry or the absence of skin in the model. The ear canal skin was not included in the model because the original FE model published by Gan et al[6] does not have the canal skin. However, to simulate blast overpressure transduction through the ear canal with the earplug inserted, the ear canal skin was added to the model.[8] The preliminary data showed that the effect of skin on overpressure transmission through the ear canal was limited. Although the addition of skin to the model did not significantly alter the pressure magnitude or P1 waveform, it is not clear how skin may affect the pressure spectra and the future study is needed. Moreover, the model-derived P1 pressure spectra were in greater agreement with the experimental data than were the predicted P2 pressure spectra; however, due to the relatively low pressure levels of the P2 waveforms, this disagreement was not considered crucial.

No experimental data currently exist that detail the response of the TM to blast exposure. The FE method is thus the best available method to investigate impulse overpressure and its effects on the TM. Future blast experiments will be designed to measure TM motion under high-intensity pressure propagation; those data will then be used to further verify the current FE model.

CONCLUSION

A FE model of the human ear including the ear canal, TM, ossicular chain, and middle ear cavity for blast wave transmission analysis has been developed. The FE model was used to predict P1 and P2 pressures induced by P0 pressure applied at the canal entrance. Further, the stress and displacement distributions on the TM were also calculated. The model was validated against experimental data with the satisfied prediction of P1 waveforms induced by P0 pressures from the vertical, horizontal, and front directions.

This model can be used for the investigation of biomechanical response of the human ear when exposed to blast overpressure. The application of experimentally measured overpressure waveforms as input to the entrance of the ear canal in the model permits the user to investigate particular disturbance sources and their impact on the ear, instead of simply the effect of altered Friedlander waveforms. The level of detail afforded by the FE method may allow for the model's application in the investigation of auditory blast injury, such as TM rupture. Hearing protection devices may be introduced to the model to study the effect of earplugs' material properties, structural designs, and insertion depths. Additionally, this model may aid in the evaluation and optimization of orifice geometries in nonlinear earplugs. This model promises to be of great value in the investigation of ear injury and in providing means to test and design protective measures for those subjected to high-intensity blast overpressures in the armed forces.

ACKNOWLEDGMENTS

The authors thank Dr. Xiao Ji, Research Associate in the Biomedical Engineering Laboratory at the University of Oklahoma, for his energy analysis expertise.

FUNDING

This work was supported by U.S. Army Medical Research and Material Command (USAMRMC) Military Operational Medicine Research Program, Contract No. W81XWH-14-1-0028.

PRESENTATIONS

Presented in a breakout session entitled "The Role of Medical Research in Blast Injury" at the 2016 Military Health System Research Symposium (abstract number: MHSRS-16–0405).

REFERENCES

1. Stuhmiller JH, Phillips YY, Richmond DR: The physics and mechanisms of primary blast injury. In: Conventional Warfare: Ballistic, Blast, and Burn Injuries, pp 241–70. Edited by Bellamy RF, Zajtchuk R, Buescher TM. Washington, DC, Department of the Army, Office of the Surgeon General, 1991.
2. Fausti S, Wilmington D, Gallun F, Myers P, Henry J: Auditory and vestibular dysfunction associated with blast-related traumatic brain injury. J Rehabil Res Dev 2009; 46(6): 797–810.
3. Saunders G, Echt K: Blast exposure and dual sensory impairment: an evidence review and integrated rehabilitation approach. J Rehabil Res Dev 2012; 49(7): 1043–58.
4. Gan RZ, Nakmali D, Xiao J, Leckness K, Yokell Z: Mechanical damage of tympanic membrane in relation to impulse pressure waveform – a study in chinchillas. Hear Res 2016; 340: 25–34.
5. Wang X, Gan R: 3D finite element model of the chinchilla ear for characterizing middle ear functions. Biomech Model Mechanobiol 2016; 15 (5): 1263–77.
6. Gan R, Reeves B, Wang X: Modeling of sound transmission from ear canal to cochlea. Ann Biomed Eng 2007; 35(12): 2180–94.
7. Zhang X, Gan R: Finite element modeling of energy absorbance in normal and disordered human ears. Hear Res 2013; 301: 146–55.
8. Leckness K: Novel finite element method to predict blast wave transmission through human ear. Thesis for Master Degree in Biomedical Engineering at University of Oklahoma, August 2016. Available at http://hdl.handle.net/11244/44932; accessed December 30, 2016.
9. Hansen OR, Hinze P, Engel D, Davis S: Using computational fluid dynamics (CFD) for blast wave predictions. J Loss Prev Process Ind 2013; 23: 885–906.
10. Cyklis P, Mlynarczyk P: The influence of the spatial discretization methods on the nozzle impulse flow simulation results. Procedia Eng 2016; 157: 396–403.
11. Davis R, Qui W, Heyer N, et al: The use of the kurtosis metric in the evaluation of occupational hearing loss in workers in China: implications for hearing risk assessment. Noise Health 2012; 14(61): 330–42.
12. Qui W, Hamernik R, Davis R: The value of a kurtosis metric in estimating the hazard to hearing of complex industrial noise exposures. J Acoust Soc Am 2013; 133(5): 2856–66.
13. Ganesh JS, Rao VS, Srinivas K: Enhanced noise type recognition using statistical measures. IOSR J Comput Eng 2012; 2(1): 19–23.

Medical Engineering and Physics 54 (2018) 14–21

Contents lists available at ScienceDirect

Medical Engineering and Physics

journal homepage: www.elsevier.com/locate/medengphy

Dynamic properties of human incudostapedial joint—Experimental measurement and finite element modeling

Shangyuan Jiang, Rong Z. Gan*

School of Aerospace and Mechanical Engineering, University of Oklahoma, 865 Asp Avenue, Room 200, Norman, OK 73019, USA

ARTICLE INFO

Article history:
Received 2 March 2017
Revised 31 December 2017
Accepted 11 February 2018

Keywords:
Incudostapedial joint
Dynamic properties
Dynamic mechanical analyzer
Frequency–temperature superposition
Finite element modeling

ABSTRACT

The incudostapedial joint (ISJ) is a synovial joint connecting the incus and stapes in the middle ear. Mechanical properties of the ISJ directly affect sound transmission from the tympanic membrane to the cochlea. However, how ISJ properties change with frequency has not been investigated. In this paper, we report the dynamic properties of the human ISJ measured in eight samples using a dynamic mechanical analyzer (DMA) for frequencies from 1 to 80 Hz at three temperatures of 5, 25 and 37 °C. The frequency–temperature superposition (FTS) principle was used to extrapolate the results to 8 kHz. The complex modulus of ISJ was measured with a mean storage modulus of 1.14 MPa at 1 Hz that increased to 3.01 MPa at 8 kHz, and a loss modulus that increased from 0.07 to 0.47 MPa. A 3-dimensional finite element (FE) model consisting of the articular cartilage, joint capsule and synovial fluid was then constructed to derive mechanical properties of ISJ components by matching the model results to experimental data. Modeling results showed that mechanical properties of the joint capsule and synovial fluid affected the dynamic behavior of the joint. This study contributes to a better understanding of the structure–function relationship of the ISJ for sound transmission.

1. Introduction

The incudostapedial joint (ISJ) is a synovial joint connecting the incus and stapes in the middle ear. ISJ consists of the articular cartilage, meniscus, capsule, and synovial fluid [1–3]. The function of the ISJ is to transmit mechanical vibration of the tympanic membrane (TM) to the stapes and cochlea, and provide flexibility to the middle ear ossicular chain [4]. The sound transmission function of the middle ear is closely related to the mechanical properties of the ISJ [4,5]. Abnormalities of the joint have been shown to impose severe conductive hearing loss, which usually requires surgical reconstruction of the ossicular chain to restore the hearing [6–10]. Recent experimental studies suggested that the increased ISJ stiffness (ankyloses) reduced the mobility of the TM and stapes footplate at 0.5–1 kHz [11], while the reduced ISJ stiffness (separation) was related to the stapes mobility loss at high frequencies [12]. These experiments, however, were not specific enough to characterize the relationship between the ISJ stiffness and middle ear transfer function without providing the material properties of the joint quantitatively.

In addition to experimental studies, the lack of knowledge on dynamic properties of the ISJ affects the accuracy of finite element (FE) modeling of the human middle ear. The ISJ has been modeled as an isotropic elastic solid body [1,13–16], an isotropic viscoelastic solid body [17,18], and a synovial joint with viscoelastic capsule [4] in published FE models of the human middle ear. The material properties of the ISJ used in these models were determined through the cross-calibration process and had significant variation across the models [4,5,16].

Experimentally measured data on the mechanical properties of the ISJ is very limited. Zhang and Gan [19] conducted quasi-static uniaxial loading tests on human ISJ samples and this is the only published biomechanical measurement based on our knowledge. Their results demonstrated that the ISJ shows viscoelastic behavior with nonlinear stress–strain relationship under quasi-static loading. They used a FE model of ISJ to show that the behavior of the joint was closely related to the mechanical properties of the joint capsule, cartilage and synovial fluid. However, the human auditory frequency ranges from 20 Hz to 20 kHz which is the normal working frequency range of the ISJ. Thus, the dynamic properties of ISJ over the frequency range may provide a better understanding of the joint's transmission function and should be modeled more accurately to describe the joint behavior.

In this paper, we report the dynamic properties of human ISJ using a dynamic mechanical analyzer (DMA) with frequency–temperature superposition (FTS). DMA is a widely used system to measure dynamic properties of materials in the frequency domain.

---

* Corresponding author.
E-mail address: rgan@ou.edu (R.Z. Gan).

https://doi.org/10.1016/j.medengphy.2018.02.006
1350-4533/

However, the frequency range of current DMA has limited high frequency access and a method to expand the testing frequency to high frequency, the FTS principle, has been reported [20,21]. The FTS principle is an empirical method which relates the effect of temperature change on dynamic properties of some materials (e.g. polymers) to that of frequency change [22,23]. In the past two decades, researchers have applied FTS principle in dynamic tests of biological tissues such as the bovine brain and vocal-fold [24–26]. Recently, our lab has reported the mechanical properties of the human TM and stapedial annular ligament (SAL) and the chinchilla SAL measured using DMA with FTS to extend measured complex modulus data of tissues to higher frequencies [27–29].

In the present study, the DMA with FTS was used for measuring dynamic properties of the human ISJ. ISJ samples were measured in the frequency range of 1–80 Hz at three different temperatures (5, 25 and 37 °C). The average complex modulus of the joints was obtained directly from the experiments. A 3D FE model of the ISJ consisting of the articular cartilage, joint capsule and synovial fluid was then constructed to identify the mechanical properties of ISJ components by matching the modeling results to the experimental data. The model was used to investigate the effect of the mechanical properties of the ISJ (the capsule and synovial fluid) on the dynamic behavior of the joint.

2. Methods

2.1. Specimen preparation and experimental setup

Eight (four left and four right) fresh human temporal bones (TBs) with an average donor's age of 69 years were involved in this study. All TBs were provided by Life Legacy Foundation, a certified human tissue supply source for medical and military research. The experiments were conducted within one week after the TB samples were received. The TB samples were covered by wet paper soaked in a prepared solution made of 0.9% saline and 15% povidone at 5 °C to maintain the physiological condition before the experiment. Each TB was examined using a light microscope to ensure that the middle ear appeared normal. The middle ear ossicles were then accessed by opening the tegmen tympani and removing the TM together with the malleus. The scala vestibule of the cochlea was opened and the stapes footplate was exposed through the medial side. The TB was then trimmed to a cube with a size of 1.5 cm × 1.5 cm × 1.5 cm to expose the ISJ with incus and stapes. A #11 scalpel was used to cut along the SAL to separate the footplate from the oval window. Note that special care was applied to keep the ISJ unstretched during the separation of the footplate from the bony wall. Finally, the stapedial tendon was removed to assure the ISJ was the only stress-bearing soft tissue in the test.

The schematic diagram of the experimental setup is shown in Fig. 1A. The ISJ specimen was fixed onto a sample holder using copper wire and melted paraffin. The load cell (5 lb, WMC-5-455 Bose, Eden Prairie, MN) of the DMA (ElectroForce 3200, Bose, Eden Prairie, MN) was placed between the sample holder and the *X*–*Y* translational stage. The translational stage was used for aligning the ISJ with the load cell in the *Z* axis under a surgical microscope (Zeiss, OPMI 1-FC), viewing from the front and lateral directions. The long process of the incus was fixed to the middle ear bony wall using cyanoacrylate gel glue. This type of glue had been validated by previous studies to provide stable fixation on the surface of biological tissues [19,27]. After the glue dried, a sharp-tip tweezer was used to assure the incus was completely immovable. The specimen was then raised up to a position where the stapes footplate was directly in contact with the lower end of the adapter. Cyanoacrylate gel glue was applied between the stapes footplate and the wooden adapter connected to the upper grip of the DMA (Fig. 1B). During this process, the ISJ stayed straight as shown in Fig. 1B indicating the structure was intact before the experiment. After the glue dried, a preload of 0.02 N compression was applied on the ISJ specimen before the experiment was started to assure all samples were tested under the same initial conditions. The preload was zeroed out before the start of the dynamic tests. The specimen was placed in a temperature-controlled chamber with a size of 25 cm × 25 cm × 10 cm (Fig. 1A). The fluctuation of the temperature inside the chamber during the test was controlled within ±1 °C by a system consisting of a thermal couple, a negative feedback circuit and a fan delivering hot or cold air.

For the dynamic measurements, sinusoidal displacements with an amplitude of 0.1 mm at the frequencies of 1, 2, 5, 10, 20, 40, 60 and 80 Hz were applied on the stapes footplate, and the force was measured by the load cell. Each measurement was performed at three temperatures: 5, 25 and 37 °C. The moisture of the specimen was maintained by adding 0.9% saline solution every five minutes onto the specimen using a syringe. At each frequency and temperature, results recorded in the first five seconds of the test were abandoned to serve as the preconditioning process. Therefore, each dynamic test itself included the preconditioning process with exactly the same testing conditions.

2.2. Dimensions and viscoelastic material model of ISJ specimen

The ISJ was separated after the completion of the dynamic test. The lenticular process of the incus and the head of the stapes were examined under a microscope. Images of the lenticular process of the incus were captured by a digital camera through the microscope (Fig. 2). The stapes head was assumed to share the same geometry with the lenticular process of the incus based on the histological images provided by Zhang and Gan [19]. Under the assumption that the cross section of the ISJ was elliptical [19], the lengths of the long axis a and short axis b were measured by image analysis software (ImageJ). The measurement was based on calculation of the pixels with a scale calibrated by a standard 1 mm scale bar next to the specimen as shown in Fig. 2. The largest values of a and b in perpendicular directions were accepted and the cross-sectional area of the ISJ was calculated by $A = \pi ab/4$. Table 1 lists the geometry data from eight ISJ specimens with the mean and standard deviation. The length of the ISJ could not be measured by direct observation. Therefore, we used the value of 0.28 mm, which was the length of the ISJ capsule measured from a histology section reported by Zhang and Gan [19].

Based on the dimensions of each specimen, the ISJ was initially assumed as an isotropic viscoelastic body to derive its complex modulus. Even though the quasi-static test of the ISJ reported the nonlinear behavior of the ISJ, the material model of the joint can still be considered as linear viscoelastic in this study because the deformation is small. Both the displacement d applied on the stapes footplate and the force F measured with the load cell were sinusoid signals for each frequency f, defined as

$$d = d_0 e^{i2\pi ft} \tag{1}$$

$$F = F_0 e^{i(2\pi ft+\delta)} \tag{2}$$

where d_0 and F_0 are the amplitude of the displacement and force, respectively, and δ is the phase delay between the displacement and force. The complex modulus at frequency f is calculated by

$$|E^*| = \frac{\sigma_0}{E_0} = \frac{F_0/A}{d_0/L} \tag{3}$$

$$E' = |E^*|\cos\delta \tag{4}$$

$$E'' = |E^*|\sin\delta \tag{5}$$

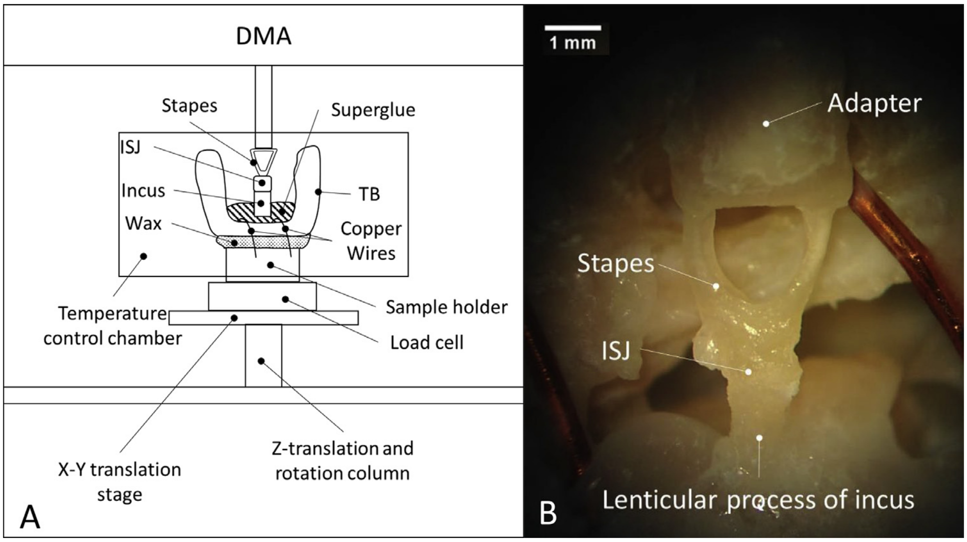

Fig. 1. (A) Schematic diagram of the experiment setup. (B) ISJ specimen mounted on the machine observed under a microscope.

Table 1
Dimensions of the ISJ specimens.

ISJ specimen ($N = 8$)	ISJ-1	ISJ-2	ISJ-3	ISJ-4	ISJ-5	ISJ-6	ISJ-7	ISJ-8	Mean	SD
Length: a (mm)	0.95	0.80	0.87	0.86	1.01	0.93	0.91	1.02	0.92	0.07
Width: b (mm)	0.65	0.57	0.65	0.60	0.71	0.68	0.75	0.70	0.66	0.06
Cross sectional area: A (mm^2)	0.485	0.358	0.444	0.405	0.563	0.496	0.536	0.560	0.481	0.074

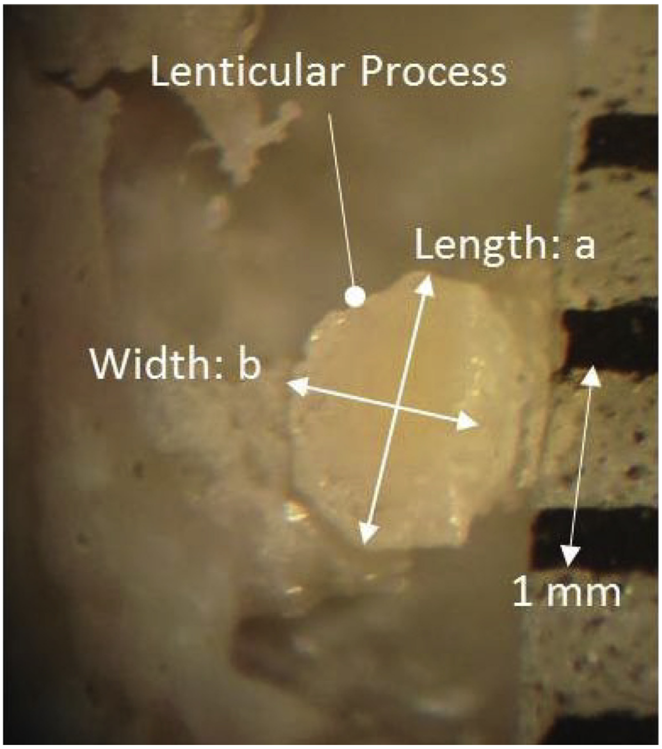

Fig. 2. Microscopic image of the lenticular process of the incus after the dynamic test for geometric measurement.

where σ_0, E_0, A, L, E^*, E' and E'' are the stress amplitude, strain amplitude, cross sectional area, length, complex modulus, storage modulus, and loss modulus of the ISJ, respectively. The inner structure and the mechanical properties of joint components were not taken into consideration at this step.

2.3. FTS principle

The FTS principle was employed to expand the frequency range of the experimental results. The FTS principle states that the curves of the complex modulus E^* obtained at a reference temperature T_0 (37 °C) can be expressed by

$$E^*(T_0,\ f) = E^*(T,\ f/\alpha_T) \tag{6}$$

where T is a lower temperature (5 or 25 °C), α_T is the shift factor quantifying the temperature's effect on a material's dynamic properties. The shift factor α_T must comply with the WLF equation which was first introduced by Williams et al. and widely used for the FTS principle [21,25]:

$$\log_{10}^{\alpha_T} = \frac{C_1(T - T_0)}{C_2 + T - T_0} \tag{7}$$

where T and T_0 are the absolute temperatures in Kelvin. c_1 is a dimensionless constant and c_2 is a constant with a unit of Kelvin.

In order to use the FTS principle, the complex moduli measured from ISJ specimens at 5, 25 and 37 °C were first plotted as a function of frequency in a logarithmic coordinate system. Then the 25 °C curves were shifted together horizontally toward higher frequencies to align with the curves obtained from 37 °C (reference temperature). Subsequently, curves from 5 °C were shifted in the same way further horizontally to connect with the points belonging to the shifted 25 °C curves. In adjacent areas, the high-frequency results obtained from the higher temperature tests were connected with the low-frequency results obtained from the lower temperature tests. Note that the shapes of the curves were horizontally stretched (37 °C) and shrunken (25 °C) in the shifting process. Finally, the master curves of complex moduli at the reference temperature were obtained. The values of α_T, c_1 and c_2 could be determined by Eqs. (6) and (7). There are three requirements in this shifting process for the FTS principle to hold: (1) the shifted curves in adjacent areas have to be matched perfectly with the curves from the lower temperature; (2) the shift factors for both

Table 2
Components and mechanical parameters of the ISJ FE model.

Components	Young's modulus (Pa)	Poisson's ratio	Viscosity (cp)
Incus	1.41×10^{10}	0.3	
Stapes head	1.41×10^{10}	0.3	
Cartilage	1.00×10^{7}	0.3	
Capsule	$E_0 = 2.9$ MPa, $E_1 = 1.25$ MPa, $E_2 = 1.9$ MPa $E_3 = 0.12$ MPa, $\tau_1 = 2.6$ ms, $\tau_2 = 0.14$ ms $\tau_3 = 0.13$ ms	0.3	
Synovial fluid	2.20×10^{9} (Bulk modulus)		4×10^{2}

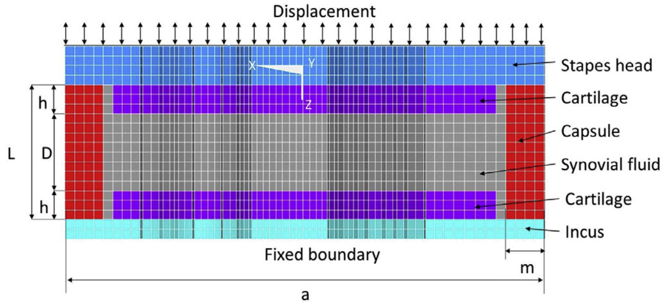

Fig. 3. Axial cross section (*X–Z* plane) of the 3D FE model of the ISJ with boundary conditions.

loss and storage modulus curves are the same; (3) the shift factors have to obey the WLF equation, or in other words, values of c_1 and c_2 should have a small standard deviation among all specimens [22,23,27–29].

2.4. Finite element modeling of ISJ

ISJ is a synovial joint with a complex inner structure. The relationship between the measured mechanical properties of the joint as an isotropic body and the mechanical properties of the components inside the joint requires further investigation. In this study, a 3D FE model of the ISJ was developed to attempt to identify the properties of the joint component. The structure of the FE model was similar to the one built in our previous study [19]. Fig. 3 shows the longitudinal cross sectional (*X–Z* plane) view of the model with boundary conditions. The *X–Y* plane cross section of the model was elliptical and *X*-axis represented the long axis. The length of the long and short axis was 0.92 and 0.66 mm, respectively, which were the mean values listed in Table 1. The thickness of the incus and stapes in this model were assumed to be 0.04 and 0.08 mm, respectively. The distance between the incus and stapes was $L = 0.28$ mm and the thickness of the capsule was $m = 0.08$ mm. The thickness of the cartilage covering the lenticular process and stapes head was set as $h = 0.08$ mm. The distance between the two cartilage layers was $D = 0.12$ mm. The FE model was meshed with hexahedral elements in ANSYS 15.0 (ANSYS Inc., Canonsburg, PA). The lenticular process, stapes, and cartilage were assigned as linear elastic Solid 45 elements. The capsule was modeled by nonlinear Solid 185 elements of viscoelastic material and the synovial fluid was modeled as Fluid 80 elements with a constant viscosity. The mechanical properties used in the model are listed in Table 2. The Young's modulus of 14.1 GPa was used for the bony structures, incus and stapes [16]. The cartilage was considered as a linear elastic material with Young's modulus of 10 MPa, the same value as that used by Funnell et al. [1] and Zhang and Gan [19]. The bulk modulus and the viscosity of the synovial fluid were obtained from Gan and Wang [16] and Zhang and Gan [19].

Our previous studies reported that the function of the ISJ largely depended on the properties of the joint capsule [19], and the viscoelastic properties of the joint capsule significantly affected the behavior of the ISJ over a frequency range of 600–6000 Hz [4]. Therefore, the capsule was assumed to be viscoelastic and the values listed in Table 2 were determined by fitting the FE model-derived force-displacement curves with the experimental results. The generalized Maxwell model was used to represent the viscoelastic behavior of the capsule as

$$E'(\omega) = E_0 + \sum\nolimits_{i=1}^{n} E_i {\tau_i}^2 \omega^2 / \left[1 + {\tau_i}^2 \omega^2\right] \tag{8}$$

$$E''(\omega) = \sum\nolimits_{i=1}^{n} E_i \tau_i \omega / \left[1 + {\tau_i}^2 \omega^2\right] \tag{9}$$

where ω is the circular frequency ($\omega = 2\pi f$) and n equals 3 (giving seven parameters E_0, E_1, E_2, E_3, τ_1, τ_2, τ_3) [27–30]. A harmonic analysis with the same boundary conditions and frequency was conducted to simulate the dynamic test. An iteration process was conducted to determine mechanical properties of the joint capsule by comparing the model-derived curves with the experimental data.

3. Results

3.1. Complex modulus obtained from dynamic tests

Dynamic tests were conducted on eight ISJ specimens to obtain their storage modulus E' and loss modulus E''. Two typical results obtained from specimens ISJ-6 and ISJ-8 are shown in Fig. 4. The storage and loss modulus measured at each frequency point at different temperatures were plotted in logarithmic coordinate system. Generally, the storage and loss modulus increased with increasing frequency or decreasing temperature. The loss modulus changed rapidly at frequencies below 5 Hz at 37 °C tests. Relatively large slopes were observed at high frequencies ($f > 10$ Hz) in both storage and loss modulus at all three temperatures. The complex modulus of other ISJ specimens showed similar curves to those in Fig. 4.

The curves of the complex moduli at 5 and 25 °C were shifted to high frequencies following the FTS principles. The master curves of samples ISJ-6 and ISJ-8 are displayed in Fig. 5A and B, respectively. For specimen ISJ-6, the storage modulus was 1.63 MPa at 1 Hz and increased to 5.97 MPa at 15 kHz, while the loss modulus increased from 0.10 MPa to 1.23 MPa. For specimen ISJ-8, the storage modulus was 1.58 MPa at 1 Hz and increased to 4.15 MPa at 15 kHz, while the loss modulus increased from 0.10 MPa to 0.85 MPa. In Fig. 5, the complex modulus-frequency curves were smoothly connected at the adjacent area without discernible discontinuities. Therefore, the master curves were generally well-matched which satisfied the first requirement of the FTS principle. Occasional fluctuations of the loss modulus curves were caused by the instability of the DMA machine at 80 Hz tests. Both storage and loss modulus were shifted by the same α_T for each specimen, which satisfied the second requirement of the FTS. The shift factors, maximum frequencies and constants c_1 and c_2 obtained from eight samples were listed in Table 3. The mean value with SD of the shift factor from 5 to 37 °C (α_5) was 183 ± 13.4. The mean value with SD of the shift factor from 25 to 37 °C (α_{25}) was 15.5 ± 4.0. The maximum frequency ranged from 12.8 to 16.0 kHz, which could cover most of the human hearing frequency range.

Table 3
The shift factors, c1 and c2 of WLF equation, and maximum frequency of human ISJ samples.

Specimen	ISJ-1	ISJ-2	ISJ-3	ISJ-4	ISJ-5	ISJ-6	ISJ-7	ISJ-8	Mean ± SD
α_{25}	12	15	23	11	18	14	18	13	15.5 ± 4.0
α_5	195	190	177	160	170	184	189	200	183 ± 13.4
ln α_5	5.27	5.24	5.17	5.07	5.13	5.21	5.24	5.29	5.20 ± 0.07
ln α_{25}	2.48	2.70	3.13	2.39	2.89	2.63	2.89	2.56	2.71 ± 0.24
c_1	16.1	11.9	8.4	15.3	9.6	12.5	10.2	14.6	12.4 ± 2.8
c_2 (K)	−65	−41	−20	−64	−27	−45	−30	−56	−44.1 ± 17.2
Maximum frequency (kHz)	15.6	15.2	14.1	12.8	13.6	14.7	15.1	16.0	14.6 ± 1.0

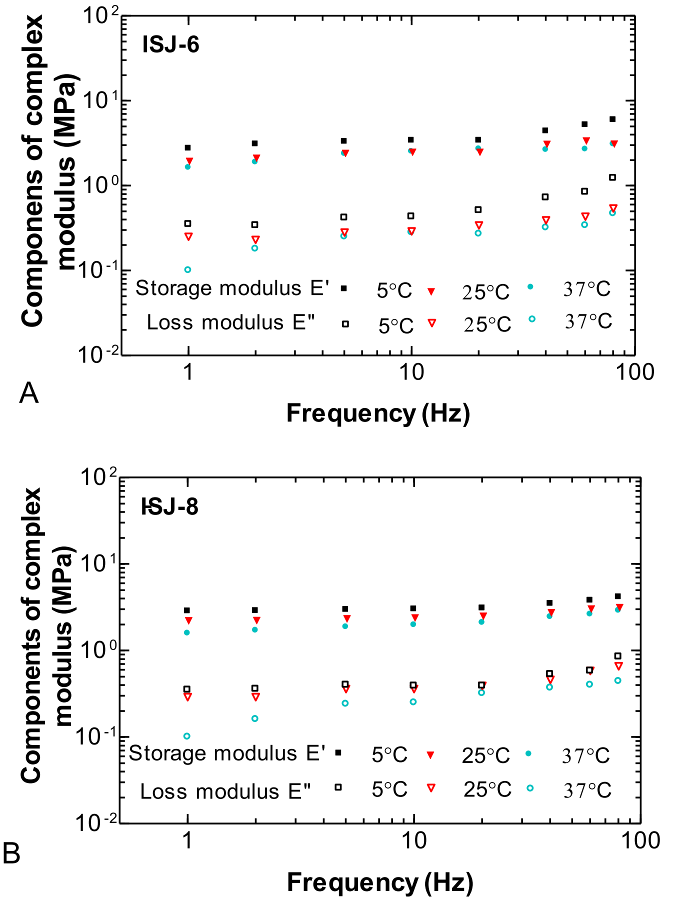

Fig. 4. The components of complex modulus curves obtained from the dynamic tests of ISJ specimens. (A) Data acquired from ISJ-6. (B) Data acquired from ISJ-8.

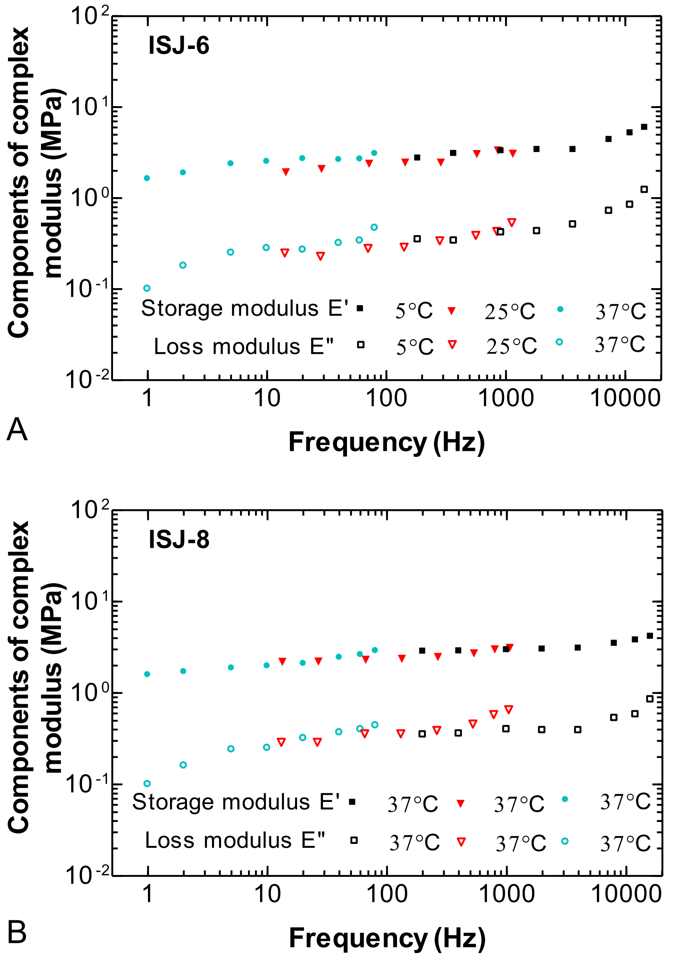

Fig. 5. Two representative master curves of the components of complex modulus at a reference temperature (37 °C) obtained by FTS principle. (A) Data acquired from specimen ISJ-6. (B) Data acquired from specimen ISJ-8.

The SD of c_1 and c_2 were 2.8 and 17.2 K, respectively, which were smaller than the values in published literature [28]. Therefore, the third requirement of the FTS is satisfied.

The master curves of the complex modulus of all eight ISJ samples were shown in Fig. 6. The mean complex modulus was calculated over the frequency range from 1 Hz to 8 kHz, the common frequency range for the eight ISJ samples. Frequencies below 8 kHz is a common range of interest in research on middle ear mechanics [4,5,14,16,17]. At 1 Hz, the mean storage modulus with SD was 1.14 ± 0.53 MPa and the loss modulus was 0.07 ± 0.04 MPa. At 8 kHz, the storage modulus was 3.01 ± 1.06 MPa, and the loss modulus was 0.47 ± 0.17 MPa. The mean curves in Fig. 6 indicate that the storage and loss modulus gradually increased with the frequency and the loss modulus had a larger slope than the storage modulus, especially at frequencies below 20 Hz. This trend shared some similarities with the viscoelastic behavior of other middle ear soft tissues reported in the previous studies [27,28].

3.2. FE model-derived data

The magnitude and phase of the force on the incus can be calculated by the complex modulus curves in Fig. 6 and the geometry data of the ISJ in Table 1 using Eqs. (1)–(5). By matching the FE model-predicted results to the experimental data, the mechanical properties of the joint capsule were determined and listed in Table 2. The seven viscoelastic parameters for the ISJ capsule solved from the FE model were $E_0 = 2.9$ MPa, $E_1 = 1.25$ MPa, $E_2 = 1.9$ MPa, $E_3 = 0.12$ MPa, $\tau_1 = 2.6$ ms, $\tau_2 = 0.14$ ms, and $\tau_3 = 0.13$ ms. The black solid line in Fig. 7A represents the mean (with SD) magnitude of force on the incus measured from eight ISJ samples and the red broken line represents the result obtained from the FE model. The black solid and red broken lines in Fig. 7B represent the mean phase shift (with SD) between the

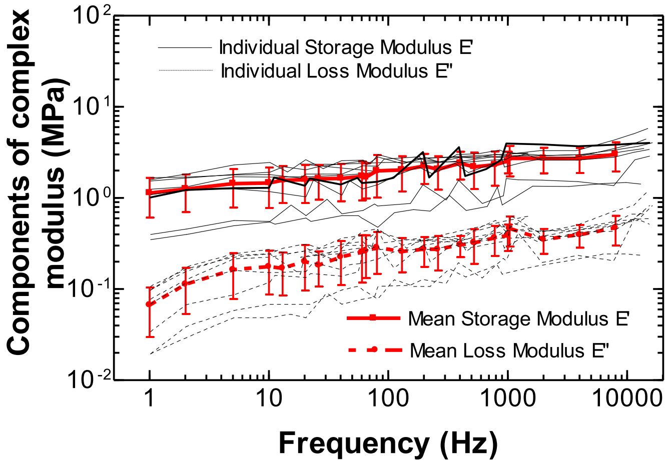

Fig. 6. The master curves of the components of complex modulus at 37 °C from 8 ISJ samples and the mean master curves of the storage and loss modulus with SD.

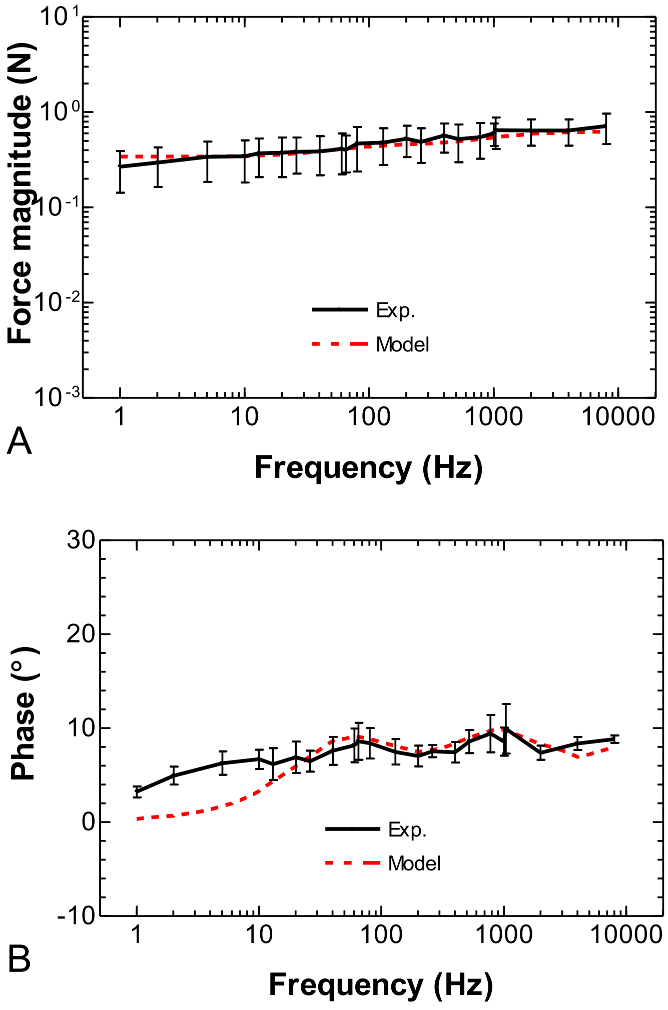

Fig. 7. Comparison between the forces on the lenticular process of the incus obtained from experimental-derived master curves and the FE model simulation. (A) The force magnitude–frequency curves. (B) The phase–frequency curves. (For interpretation of the references to color in the text, the reader is referred to the web version of this article.)

displacement and the force obtained from the experiment and FE model, respectively. Overall, the model predicted results matched the experimental data except for phase values at frequencies below 10 Hz. Since 10 Hz is lower than the normal auditory frequency range, the deviations are acceptable. Note that in the frequency range of 10–80 Hz where the results were directly obtained from the experimental data without any extrapolation by the FTS principle, the experimental data and model prediction still matched well. The good matching between the experimental and model-derived data suggested that the generalized Maxwell model ($n = 3$) was able to characterize the viscoelastic behavior of the joint capsule over the auditory frequency range.

4. Discussion

4.1. Comparison with published data

To the best of our knowledge, though the mechanical properties of human ISJ under quasi-static loading conditions were reported [19], there was no published data on dynamic properties of the ISJ in human or experimental animals by the time this paper was composed. Results from tension, compression, and stress relaxation tests by Zhang and Gan [19] demonstrated that the human ISJ exhibited typical viscoelastic behavior. Considering the displacement amplitude used in the present dynamic test was 0.1 mm, the average elastic modulus obtained from the 0.1 mm quasi-static tension and compression reported by Zhang and Gan was used for comparison. The mean storage modulus at 1 Hz (lowest testing frequency) in current experiment is 1.14 MPa (Fig. 6) and the result from quasi-static tests was approximately 1.17 MPa. Considering the strain rate of the sample in 1 Hz dynamic test was comparable to the condition of the quasi-static test, the mechanical properties of ISJ obtained in this study matched well to that reported in the previous study.

4.2. Contribution of the FE model of ISJ

Even though the quasi-static properties of the ISJ [19] and the analysis of ISJ structural effect on middle ear transfer function [4] have been reported, the dynamic properties of the joint remain unknown. In this study, the complex modulus of ISJ was obtained experimentally, and the mechanical properties of the joint capsule were predicted through the FE model of ISJ. To compare the ISJ mechanical properties obtained in this study with those used in the published FE models of the human ear, the ISJ model in Fig. 3 was replaced by two solid models of ISJ: linear elastic and viscoelastic replaced by two solid models of the ISJ, linear elastic [16] and viscoelastic [18], respectively. The linear elastic model of ISJ was based on the material properties used by Gan and Wang [16] with a Young's modulus of 0.6 MPa. The viscoelastic ISJ model was based on the material properties reported by Zhang and Gan [18] as the standard linear viscoelastic material with $E_0 = 0.4$ MPa, $E_1 = 20$ MPa, and $\tau_1 = 20\ \mu$s. Fig. 8 shows the results of two material models of the ISJ in comparison with the experimental data and FE model results of this study. As shown in Fig. 8A, the linear elastic ISJ is unable to simulate frequency-dependent behavior of the joint, and there is no phase shift for the linear elastic ISJ in Fig. 8B. The force magnitude derived from the viscoelastic ISJ is lower than the experimental results at low frequencies and higher at high frequencies ($f > 800$ Hz). The phase angle of the derived force on the joint shown in Fig. 8B displays a huge increase at $f > 30$ Hz when the ISJ was molded as viscoelastic material. This indicates that the absence of the synovial fluid, cartilage, and viscoelastic joint capsule may not represent the dynamic behavior of the ISJ over a broad frequency range. However, future study on using dynamic properties of the ISJ in the human

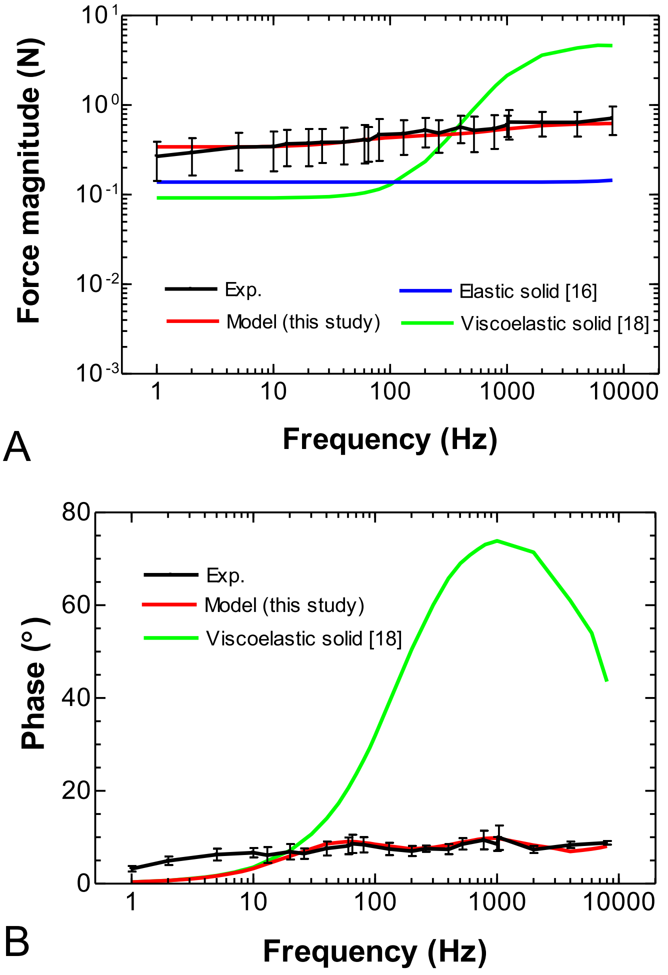

Fig. 8. Comparison between the forces on the lenticular process of the incus obtained from experimental-derived master curves and the FE models based on different material properties. (A) The force magnitude–frequency curves. (B) The phase–frequency curves.

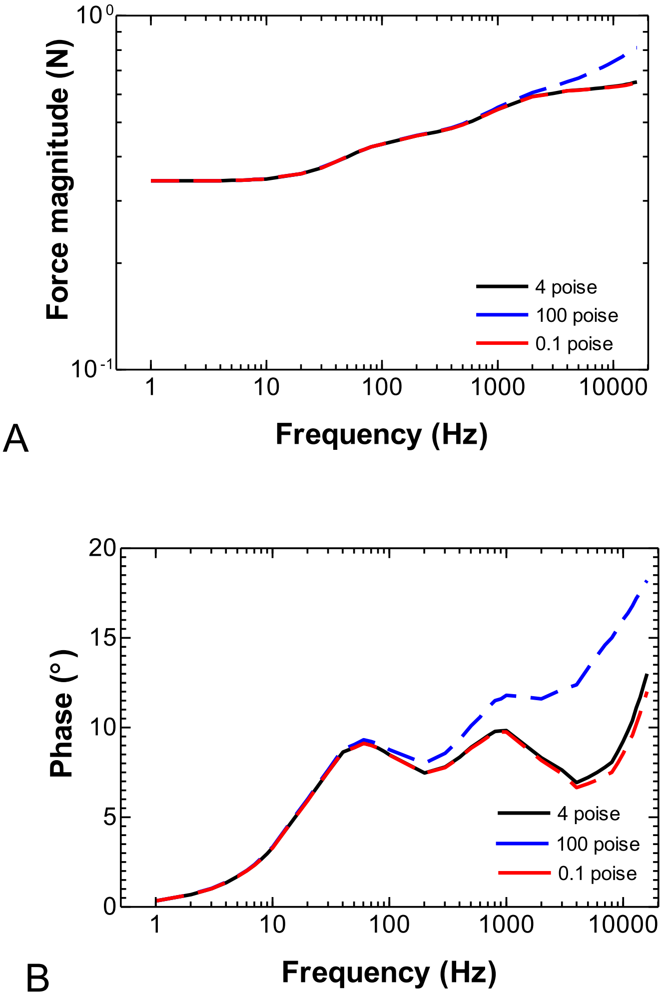

Fig. 9. Curves describing the force on the lenticular process of incus derived from the FE model simulation with different levels of synovial fluid viscosity. (A) The force magnitude–frequency curves. (B) The phase–frequency curves.

ear model may provide more insights for ISJ mechanical function for sound transmission. Fig. 8 demonstrates that the model results can be used to simulate the ISJ in the human middle ear model with higher accuracy comparing to previous models over the auditory frequency range.

In addition to providing the values of mechanical properties of the joint components, the FE model of the ISJ may also be used to evaluate the contribution of each component to the overall stiffness of the joint over the frequency range. The previous ISJ modeling suggested that the behavior of the joint was sensitive to the viscosity of the synovial fluid [4,19]. To confirm this observation, we conducted an analysis in the current ISJ model by varying the viscosity of the synovial fluid from 100 to 0.1 poise and calculating the force induced on the incus over frequencies of 1 Hz to 8 kHz as shown in Fig. 9. The model-derived force magnitude in relation to frequency is shown in Fig. 9A, and the phase shift between the displacement and force is shown in Fig. 9B. Note that the viscosity of the synovial fluid inside the articular joint changed from 100 to 0.1 poise when the shear rate increased from 0 to 5000/s due to the shear-thinning effect of the synovial fluid [31]. During the deformation process of the ISJ, the synovial fluid experienced shearing. Based on a broad frequency range of the results in Fig. 9 (1–8 kHz), the shear rate of the synovial fluid would increase with the testing frequency which might make the shear-thinning effect unneglectable. Considering that the frequency of the results in Fig. 9 was obtained by extrapolation, the values of the shear rate of the synovial fluid was difficult to be determined quantitatively from the frequency values. Therefore, values between 0 and 5000/s were used to make a qualitative estimation on the shear rate of the synovial fluid in the ISJs in this study to illustrate how the thinning effect of the synovial fluid will affect the behavior of the joint. Viscosity of 4 poise was used as the normal value for synovial fluid used in this study. As shown in Fig. 9, there was no significant difference in magnitude or phase of the force at low frequencies. The fluid viscosity started showing effects on the force magnitude at 1 kHz (Fig. 9A) and on the phase at 60 Hz (Fig. 9B). It can be said that the synovial fluid is a typical bioviscoelastic fluid whose storage and loss shear modulus increase with the shear rate [31]. In this study, the shear rate of the fluid is proportional to frequency in dynamic tests. Higher testing frequency results in higher storage and loss modulus of the synovial fluid, which increase the stiffness and energy dissipation of the entire ISJ structure. The change of mechanical properties of the ISJ was demonstrated by the increased force magnitude and phase of the incus in the FE model. Conclusively, the viscosity of the synovial fluid contributes to dynamic behavior of the ISJ mostly at high frequencies.

This study is the first report on dynamic properties of the human ISJ and we attempt to describe the properties of ISJ components based on a FE model of the joint. However, the measurement of the ISJ geometry was relatively coarse, especially the parameters which are unable to be measured directly in this study, such as the *m, L, h* and *D* as shown in the model of Fig. 3. Zhang and Gan [19] reported that the thinner cartilage (*h* decreased) would result in a reduced compressive stiffness of the ISJ. Therefore, if the h value used in the FE model is lower than the value in the experiment, the viscoelastic parameters of the joint capsule (E_0, E_1) obtained from the simulation would be higher than the true values. Moreover, the thickness of the capsule *m* is not directly measured either. Given the displacement-force relationship obtained from the FE model unchanged, the stiffness of the joint capsule would be negatively correlated with the value of *m*. In our future studies, we will explore the optic coherence tomography technique for measuring the ISJ structure. The accurate morphological data of ISJ will improve not only the experimental results, but also the FE model of the joint [32]. In addition to the ISJ's geometry parameters, the material properties of some components such as the cartilage are simplified as linear elastic in FE simulation. The frequent-dependent behavior of the cartilage was not involved in modeling analysis. The results provided by Zhang and Gan [19] indicated that the stiffness of the ISJ increased with the elastic modulus of cartilage, but the effect was less significant than that of cartilage thickness. Gan and Wang [4] suggested that the effect of the elastic modulus of the cartilage on the mobility of the incus was decreased with frequency if the cartilage was linear elastic. Another recent study indicated that the transfer function of the middle ear was closely related to the pretension inside the ossicular chain [33]. In this study, the pretension of the ossicular chain was released during the specimen preparation process and the initial status of the ISJ tested in the experiments was different from the physiological condition. In future studies, we may consider conducting the mechanical measurement with an intact ossicular chain.

5. Conclusion

Dynamic properties of human ISJ samples at 1–80 Hz were measured by DMA and the frequency range of the results was extrapolated by FTS principle to 8 kHz. The experimental data has been analyzed with a FE model of the joint. The mean value of storage modulus increased from 1.14 MPa at 1 Hz to 3.01 MPa at 8 kHz and the loss modulus increased from 0.07 MPa at 1 Hz to 0.47 MPa at 8 kHz. The 3D FE model of the human ISJ was used for identifying mechanical properties of the joint components by matching the model-derived data to the experimental results. The viscoelastic properties of the joint capsule were determined by using a 7-term generalized Maxwell model. The FE analysis indicated that the mechanical properties of the ISJ capsule and the viscosity of the synovial fluid affect the dynamic behavior of the joint. The results reported in this paper provide useful data for improving the accuracy of FE models of the human middle ear and contribute to a better understanding of the structure–function relationship of the ISJ.

Acknowledgments

We thank Don Nakmali for his help in sample preparation. This study was supported by National Institutes of Health (NIH) under grant R01DC011585 and Department of Defense (DOD) under grant W81XWH-14-1-0228.

References

[1] Funnell WRJ, Siah TH, McKee MD, Daniel SJ, Decraemer WF. On the coupling between the incus and the stapes in the cat. J Assoc Res Otolaryngol 2005;6(1):9–18.
[2] Karmody CS, Northrop CC, Levine SR. The incudostapedial articulation: new concepts. Otolo Neurotol 2009;30(7):990–7.
[3] Ortug G, Ortug C, Aydar Y. Configurations of incudostapedial joint surface, an SEM Study. FASEB J 2006;20(4):A442.
[4] Gan RZ, Wang X. Modeling microstructure of incudostapedial joint and the effect on cochlear input. Mechanics of hearing: protein to perception. Karavitaki KD, Corey DP, editors. Melville, NY: AIP; 2015.
[5] Gan RZ, Wood MW, Dormer KJ. Human middle ear transfer function measured by double laser interferometry system. Otol Neurotol 2004;25(4):423–35.
[6] Vishwakarma R, More YI, Joseph ST, Patel KB, Ramani MK, More RI. Incudostapedial joint arthroplasty using temporalis fascia/perichondrium ties. Am J Otolaryngol 2009;30(3):171–5.
[7] Maducdoc MM, Ghavami Y, Shamouelian D, Mahboubi H, Djalilian HR. Congenital anomalies of the incudostapedial joint. Int J Pediatr Otorhinolaryngol 2015;79(12):2277–80.
[8] Suzuki M, Kanebayashi H, Kawano A, Hagiwara A, Furuse H, Yamaguchi T, Shimizu M. Involvement of the incudostapedial joint anomaly in conductive deafness. Acta Otolaryngol 2008;128(5):515–19.
[9] Sim RJ, Chang P. Incudostapedial ankylosis from temporomandibular joint disruption. Otolaryngol Head Neck Surg 2008;139(1):166–7.
[10] Celik H, Aslan Felek S, Islam A, Demirci M, Samim E, Oztuna D. The impact of fixated glass ionomer cement and springy cortical bone incudostapedial joint reconstruction on hearing results. Acta Otolaryngol 2009;129(12):1368–73.
[11] Alian W, Majdalawieh O, Kiefte M, Ejnell H, Bance M. The effect of increased stiffness of the incudostapedial joint on the transmission of air-conducted sound by the human middle ear. Otol Neurotol 2013;34(8):1503–9.
[12] Szymanski M, Rusinek R, Zadrozniak M, Morshed K, Warminski J. The influence of incudostapedial joint separation on the middle ear transfer function. Clin Exp Otorhinolaryngol 2014;7(4):250–3.
[13] Prendergast PJ, Ferris P, Rice HJ, Blayney AW. Vibro-acoustic modelling of the outer and middle ear using the finite-element method. Audiol Neurotol 1999;4(3–4):185–91.
[14] Gan RZ, Feng B, Sun Q. Three-dimensional finite element modeling of human ear for sound transmission. Ann Biomed Eng 2004;32(6):847–59.
[15] Wada H, Koike T, Kobayashi T. Three-dimensional finite-element method (FEM) analysis of the human middle ear. In: Middle ear mechanics in research and otosurgery; 1997. p. 76–80.
[16] Gan RZ, Wang X. Multifield coupled finite element analysis for sound transmission in otitis media with effusion. J Acoust Soc Am 2007;122(6):3527–38.
[17] Gan RZ, Zhang X, Guan X. Modeling analysis of biomechanical changes of middle ear and cochlea in otitis media. In: Shera CA, Olson ES, editors. AIP conference proceedings; 2011. p. 539–44.
[18] Zhang X, Gan RZ. Finite element modeling of energy absorbance in normal and disordered human ears. Hear Res 2013;301:146–55.
[19] Zhang X, Gan RZ. Experimental measurement and modeling analysis on mechanical properties of incudostapedial joint. Biomech Model Mechanobiol 2011;10(5):713–26.
[20] Ferry JD. Mechanical properties of substances of high molecular weight: VI. Dispersion in concentrated polymer solutions and its dependence on temperature and concentration. J Am Chem Soc 1950;72(8):3746–52.
[21] Williams ML, Landel RF, Ferry JD. The temperature dependence of relaxation mechanisms in amorphous polymers and other glass-forming liquids. J Am Chem Soc 1955;77(14):3701–7.
[22] Ferry JD. Viscoelastic properties of polymers. John Wiley & Sons; 1980.
[23] Nielsen LE, Landel RF. Mechanical properties of polymers and composites. second ed. New York: Marcel Dekker; 1994.
[24] Peters GW, Meulman JH, Sauren AA. The applicability of the time/temperature superposition principle to brain tissue. Biorheology 1997;34(2):127–38.
[25] Chan RW. Estimation of viscoelastic shear properties of vocal-fold tissues based on time-temperature superposition. J Acoust Soc Am 2001;110:1548–61.
[26] Miri AK. Mechanical characterization of vocal fold tissue: a review study. J Voice 2014;28(6):657–67.
[27] Zhang X, Gan RZ. Dynamic properties of human tympanic membrane based on frequency-temperature superposition. Ann Biomed Eng 2012;41:205–14.
[28] Zhang X, Gan RZ. Dynamic properties of human stapedial annular ligament measured with frequency–temperature superposition. J Biomech Eng 2014;136:0810041–7.
[29] Hitt BM, Wang X, Gan RZ. Dynamic property changes in stapedial annular ligament associated with acute otitis media in the chinchilla. Med Eng Phys 2017;40:65–74.
[30] Oskui IZ, Hashemi A. Dynamic tensile properties of bovine periodontal ligament: a nonlinear viscoelastic model. J Biomech 2016;49(5):756–64.
[31] Fung YC. Biomechanics: mechanical properties of living tissues. second ed. New York: Springer Science & Business Media; 1993.
[32] Park J, Cheng JT, Ferguson D, Maguluri G, Chang EW, Clancy C, Lee DJ, Iftimia N. Investigation of middle ear anatomy and function with combined video otoscopy-phase sensitive OCT. Opt Express 2016;7(2):238–50.
[33] Koch M, Eßinger TM, Stoppe T, Lasurashvili N, Bornitz M, Zahnert T. Fully implantable hearing aid in the incudostapedial joint gap. Hear Res 2016;340:169–178.

SEM 2018 conference proceeding paper

Measurement of the Viscoelastic Properties of the Chinchilla Tympanic Membrane

Junfeng Liang[a], Rong Z. Gan[b] and Hongbing Lu[a]
[a] Dept. of Mechanical Engineering, University of Texas at Dallas, Richardson, TX
[b] School of Aerospace and Mechanical Engineering, University of Oklahoma, Norman, OK

Abstract

Tympanic membrane (TM) is transmits the sound pressure in the outer ear into mechanical vibration in the middle ear. Quantitate study on the middle ear sound transfer function requires accurate measurements of the TM mechanical properties. In this paper, a dynamic micro-fringe projection technique is developed to measure the viscoelastic properties of the chinchilla TM. An intact TM in the bulla is inflated with a time-varying air pressure. Micro-fringes are projected onto the TM surface during the inflation process and the surface image of the TM is captured with a digital video camera connected to a microscope. The pressure-volume displacement relationship is calculated with a phrase-shift algorithm. Finite element method with the implementation of a viscoelastic model is employed with the pressure history as input. A viscoelastic model is used to model material properties. By solving an inverse problem with the model, the viscoelastic properties of the TM are determined.

Key Words: Tympanic membrane, Viscoelastic, Micro-fringe projection, Finite element method, Inverse method

1. Introduction

Studies of the mechanical behavior of the tympanic membrane (TM) are of a great interest since TM is the first and an important organ that transmits sound pressure to mechanical vibration into the inner ear. Recently, various high fidelity finite-element method (FEM) models of the middle ear have been developed to study the sound transmission and to simulate different types of auditory tests [1-3]. For these FEM models, the mechanical properties of the middle ear structures are the key impacts that control the accuracy of the simulation results. However, TM as a soft tissue has a highly complex laminate structure with nonlinear, anisotropic, time, and rate dependent behavior and is very sensitive to the testing condition. The mechanical properties of TM are difficult to measure and simulate. Many researchers have been actively developed techniques to measure the mechanical properties of TM. The existing measurement techniques, according to the sample preparation, generally fall into two categories: ex situ and in situ. In the former category, the TM was usually cut into strips or dissected from the middle ear and tested with various mechanical measurement settings such as tensile test [4], dynamic analysis [5], acoustic driving test [6], split Hipkinson tension bar [7], and nano-indentation[8]. With the help of imaging techniques, such as projection moiré [9], digital image correlation [4], and fringe projection [10, 11], moiré [12-15], in situ measurement of the mechanical properties of TM also became feasible by combing with indentation or pressure as loading.

In the most previous study, to simplify the measurement, TM was simplified as an elastic membrane. In recent years, viscoelastic and hyperelastic characteristics of TM were measured. However, so far there are no results reported on the mechanical properties of the TM with the consideration of both viscoelastic and hyperelastic characteristic. In this paper, we report our results on the visco-hyperelastic properties of TM using a dynamic micro-fringe projection technique. In this method, dynamic pressures was applied to the TM in situ and the images of the TM were acquired by a micro-fringe projection technique. FEM simulation results were used to solve an inverse problem to determine the visco-hyperelasic properties of the TM.

2. Method

2.1 Visco-Hyperelastic Model

A large-strain visco-hyperelastic model was used to describe the mechanical behavior of the TM. This model is based on the formulation proposed by Simo, et. al [16], amended to take into account the viscous shear response. The constitutive equations for hyperelastic material with strain-energy function Φ is given by:

$$\mathrm{S}^{2d} = 2\frac{\partial \Phi}{\partial \mathrm{C}} \tag{1}$$

where S^{2d} is the second Piola-Kirchhoff stress tensor and C is the Cauchy-Green deformation tensor. The true stress can be obtained as:

$$\sigma = \frac{1}{\mathrm{J}}\mathrm{F}\mathrm{S}^{2d}\mathrm{F}^{T} \tag{2}$$

Where F is the deformation gradient tensor and J is the determinant of F. Following Simo, et. al [12] and Holzapfel, et. al [17], assuming the material is isotropic, the viscoelastic constitutive equations, in terms of the second piola-kirchhoff stress, is given by

$$\mathrm{S}^{2d} = \int_{0}^{t} \left[\alpha_{\infty}^{K} + \sum_{i=1}^{n} \alpha_{i}^{K} \exp\left(-\frac{t-\tau}{\tau_{i}^{K}}\right)\right]\left(2\frac{d}{d\tau}\frac{d\mathrm{U}}{d\mathrm{J}}\right) \mathrm{d}\tau \tag{3}$$

where α_i^K are the bulk relative moduli and τ_i^K are the bulk relaxation time to be determined. U is the isotropic part of the strain energy. To simplify the parameter fitting, n was chosen as 1 in this study.

The constitutive model here chosen for the description of the hyperelastic behavior of the rubber is the 2nd order Ogden model, as has been used in our previous work on the static measurement for guinea pig, chinchilla and human TMs. The Ogden formulation of the strain energy function U is expressed by:

$$\mathrm{U} = \sum_{i=1}^{2} \frac{2\mu_i}{\alpha_i}\left(\lambda_1^{\alpha_i} + \lambda_2^{\alpha_i} + \lambda_3^{\alpha_i}\right), i = 1,2 \tag{4}$$

where λ_j (j=1, 2, 3) are the principle stretch ratios; μ_i and α_i are constants describing the hyperelastic properties of the material.

2.2 Experimental Setup

The schematics of experimental setup of the dynamic micro-fringe projection system is plotted in Fig. 1. The system consists of the loading section and the acquiring section. In the loading section, a syringe pump that consists of an actuator (Progressive Automation PA-15-411) and a pressure cylinder was used to apply pressure to the sample. In the acquiring section, a micro-fringe projector with camera was used to capture the deformation of the sample and a pressure sensor (Omega Engineering, PX309) was used to record the history of the applied pressure. To synchronize the loading and the acquire system during the measurement, an electrical controlled shutter was also configured into the system. All the electrical driven components shared the same DC power supply (Topward, 6306D).

Before the test, the sample was connect to the syringe pump and the pressure sensor, and mounted on a sample holder that allowed a 6 degrees of freedom motion. The sample was positioned at the location with an angle so that the sample was covered with the fringes from the projector and could be acquired by the camera free from shadow. The camera was turned on to continuously record. The shutter was then manually set to close mode to mark the initial stage for image acquisition. When the power supply was turned on, the pressure sensor began to record the pressure. At the same time, the shutter open to allow the camera to acquire the fringe pattern on the sample. It also simultaneously triggered a snap-acting switch that turned on the syringe pump. Therefore, the recorded data on pressure and the deformation were synchronized.

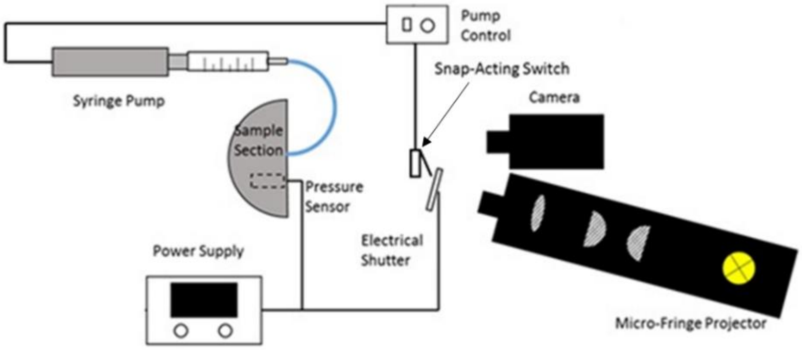

Figure 1 Schematic of the Dynamic micro-fringe projection system. For illustration purpose, the components are not plotted with actual scale.

2.3 Inverse Problem Solving

The distorted micro-fringe patterns projected on a deformed surface contains the geometrical information of the surface. By comparing this pattern with that on a planar reference, with a five phase-shifted algorithm, the surface profile of the deformed surface of the sample under the pressure at each time step can be reconstructed. The volume displacement of the TM can be calculated by summation of the height over the surface as described with following formula:

$$\Delta V = \iint_{\Omega} [z(x,y) - z_0(x,y)]\mathrm{d}x\mathrm{d}y \tag{5}$$

where, $z(x,y)$ and $z_0(x,y)$ are the height profiles under a finite pressure and the zero pressure, respectively, Ω is the area enclosed by the annulus.

To determine the mechanical properties of the sample, an inverse problem solving procedure was used. The 3-demesional surface reconstruction of the sample at zero-pressure state was used to build a corresponding FEM model. Simulation for the experiment was carried out by applying recorded pressure onto the model. Volume displacement from the simulation was compared with the experimental results to adjust the mechanical properties used in the simulation. This iteration continued until simulated volume displacement agreed well with the experimental one. The detail about the inverse problem can be found in our previous work [10, 11].

2.4. Materials and Sample Preparation

Latex rubber membrane (SensiCare, MD8085) was first used as a standard material to validate the method. Since there is no existed mechanical properties reported on the latex. The membrane material was measured with a dynamic tensile test to evaluate the viscoelastic properties. The data were then used to compare with that measured with the present dynamic micro-fringe projection measurement.

Fig. 2 shows the configuration that used to hold the latex rubber membrane. The membrane was secured in a two part holder with a hole with 12.5 mm diameter that clamps the boundary of the membrane with a rubber o-ring. Such an arrangement allows the full sealant between the membrane and the hole in the holder and protects the membrane from being damaged by the shearing force from the holder. Pressure was applied to the hole of the holder through an outlet that connected to the syringe pump.

Figure 2 Sample holder for testing rubber membrane using a dynamic micro-fringe projection system.

After validation of the method. Nine chinchilla TMs inside the bulla were tested using the dynamic micro-fringe projection system. The information of the samples was given in Table 1.The nine chinchilla bullas were harvest freshly from five adult chinchillas following the protocol approved by the institutional Animal Care and Use Committee (IACUC) of the University of Oklahoma and met the guidelines of the National Institutes of Health. The TM was exposed for the projection and painted with a thin layer of titanium oxide to improve the reflectiveness. A polyvinyl chloride tubing was inserted and sealed on the ear canal. The TM and the ear canal formed a conceal chamber allowing the TM be inflated by the air pressure from the syringe pump. The total sample preparation time was about 45 minutes. A droplet of saline water was applied on the TM every 5 minutes to prevent the TM from dehydration. Before test, the sample was deflated and deflated several times at low pressure to allow the sample to reach steady state.

Table1. Dimensions of the chinchilla TM specimens

Sample #	Ear	Superior-Inferior (mm)	Anterior-Posterior (mm)
Ch17-2-6	R	8.16	9.15
Ch17-2-8L	L	7.89	9.32
Ch17-2-8R	R	8.06	8.18
Ch17-2-11	R	7.64	8.89
Ch17-2-13	L	8.08	8.67
Ch17-4-2L	L	8.13	9.06
Ch17-4-3	L	8.07	8.90
Ch17-4-4	L	7.99	8.91
Ch17-4-13	L	8.02	9.03

3. Result

3.3 Latex Rubber

Fig. 3 shows the typical pictures of the latex rubber acquire by the camera. These pictures were extracted from a video on the deformation of the sample with ~3 second. To illustrate the deformation process, latex rubber under four different pressures at four different instance are plotted, which corresponding to the pressure history plot shown in Fig. 4.

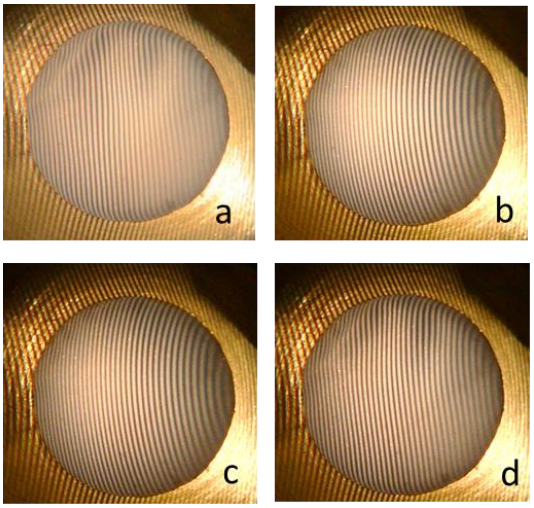

Figure 3. Typical images of deformed latex rubber under air pressure at different time: (a). t=0 s, p=0 kPa; (b). t=1 s, p= 2.3 kPa; (c) t=2 s, p=2.8 kPa; (d) t=3 s, p=0.7 kPa.

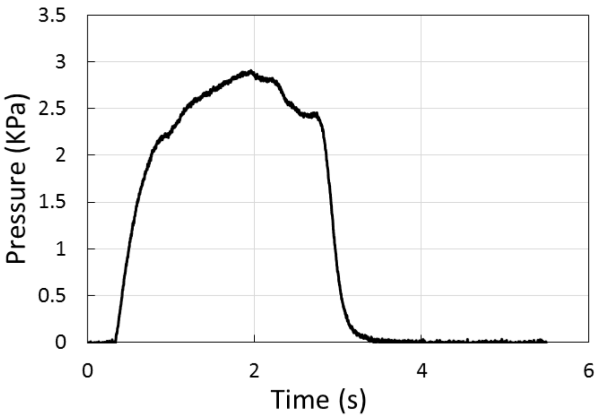

Figure 4. History of pressure applied on the latex rubber

3-dimensional surface reconstruction was then applied on the images of the fringe patterns on the deformed membrane. Fig. 5 demonstrates the surface profiles corresponding to the images in Fig. 3. Following Eqn. 5, volume displacements over time were calculated with these surface profiles, which is shown in Fig. 6. Note that due the intensity of the data, only the first 0.6 second was used to determine the mechanical properties. Therefore, only 10 points of volume displacement were shown in the figure. FEM simulation of a membrane with the same dimension was run to determine the mechanical properties of the latex rubber using the iteration mentioned in the method section. The simulation results are also plotted in Fig. 6. The parameters used in the FEM simulation were: μ_1=0.4, α_1=3.0, μ_2=4.3, α_2=-0.9, γ=0.15, and τ=950. To validate the mechanical properties measured, the results are compare with that measured with a tensile test. Fig.7 shows the comparison between results from micro-fringe projection measurement and the tensile test on the latex rubber membrane.

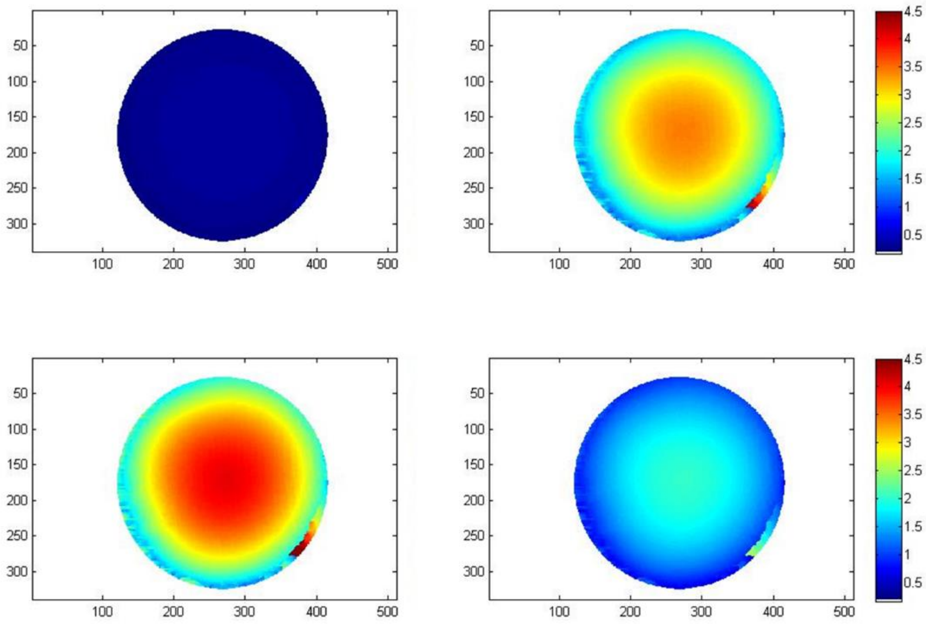

Figure 5 Three-dimensional surface tomography of the deformed latex rubber: (a). t=0 s, p=0 kPa; (b). t=1 s, p= 2.3 kPa; (c) t=2 s, p=2.8 kPa; (d) t=3 s, p=0.7 kPa. All the numbers in the figure are all in the unit of millimeter.

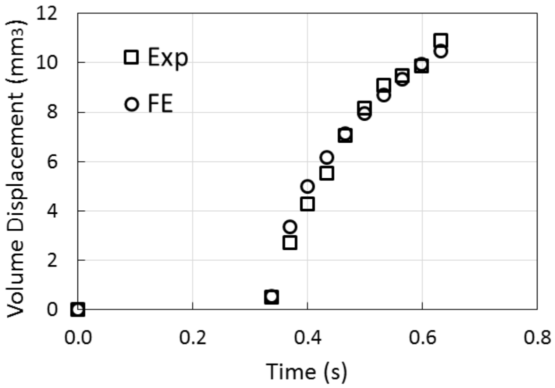

Figure 6 Curve-fitting for the volume displacement of the latex rubber versus time: Exp (Experimental results) and FE (Finite element results)

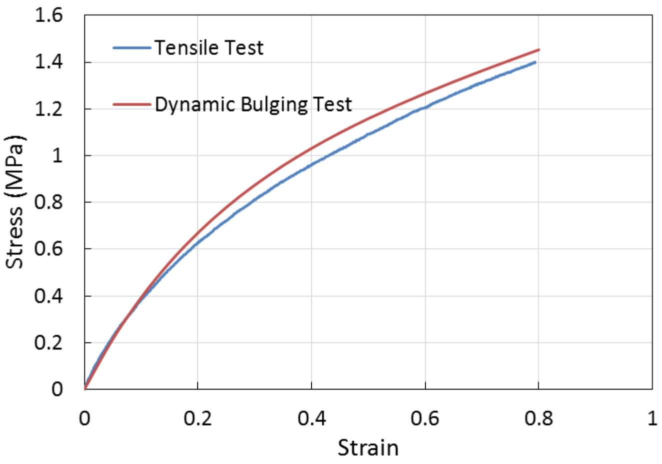

Figure 7. Mechanical properties of latex rubber measurement by tensile test and dynamic bulging test micro-fringe projection system.

Following the same procedure, dynamic micro-fringe measurements were applied on the chinchilla TM specimens. The history of the pressures applied on the nine chinchilla TM specimens were plotted in Fig. 8. The magnitude of the pressures and the time span were currently randomly controlled manually. The actually pressure histories were used in the FEM simulation. Fig. 9 shows the specimen under different pressures projected with micro-fringes and their corresponding 3-dimensional surface reconstruction. Using the surface profile, the volume displacements of the five chinchilla TMs were calculated and were shown in Fig. 10. Note that volume displacements of at only 10 different pressures were shown in the figure. FEM simulation was run for the inverse problem on each specimen to determine the mechanical properties using the constitutive law in Eqn. (3). The curve fitting in the inverse problem were plotted in Fig. 10 in dash lines. The mechanical determined properties were listed in Table 2. The first four parameters describe the hyperelastic behavior of the TM materials as shown in Eqn. (4). The last two parameters describe the viscoelastic behavior of the TM, where γ is the relative modulus and τ is the relaxation time.

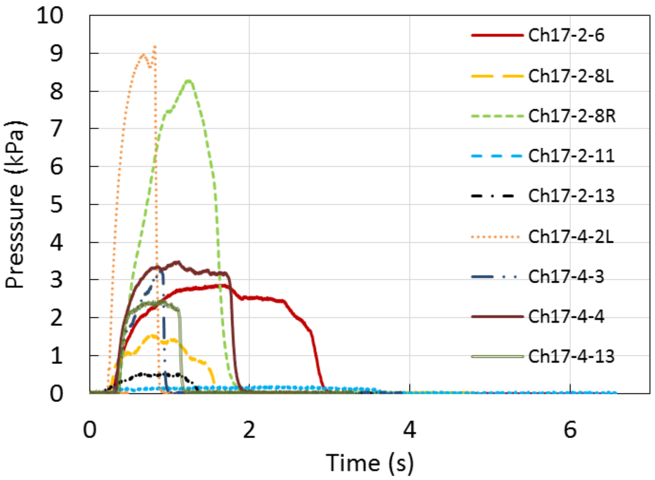

Figure. 8 The histories of the pressures applied on the five chinchilla TM specimens.

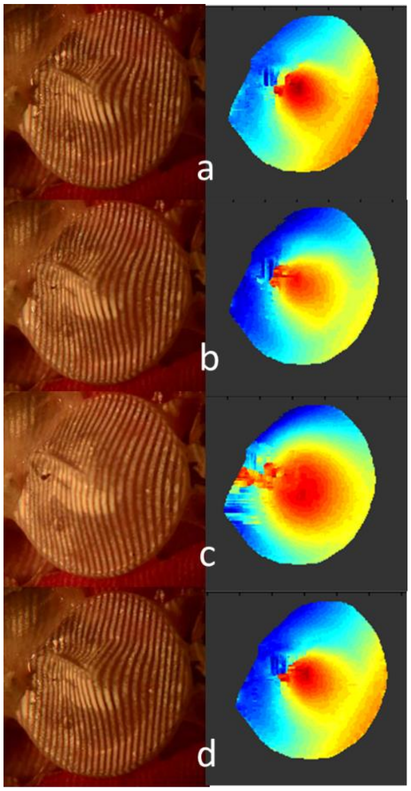

Figure. 9 Typical images of deformed chinchilla TM under air pressure at different time: (a). t=0 s, p=0 kPa; (b). t=0.5 s, p= 1.03 kPa; (c) t=1 s, p=1.38 kPa; (d) t=1.5 s, p=0.61 kPa. The color maps demonstrate the 3D-reconstruction of the chinchilla TM.

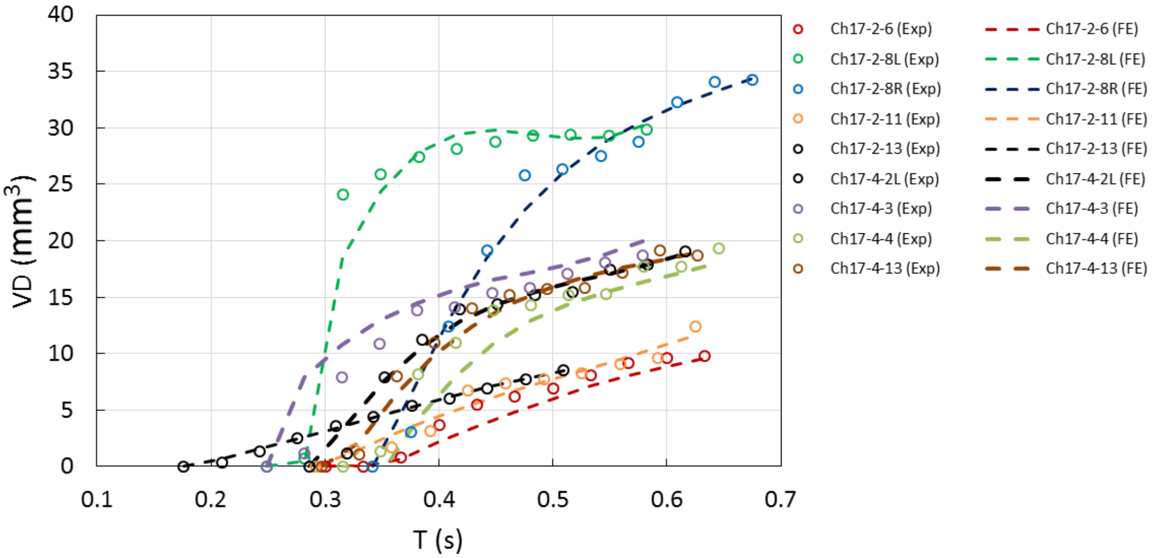

Figure. 10 Volume displacements of the five chinchilla TM specimen over time. The circle plots are the experimental data while the dash lines are the FEM simulation results.

Table 2. Visco-hyperelastic properties of chinchilla TMs.

Sample #	μ_1	$\alpha_{1\ (\mathrm{MPa})}$	μ_2	$\alpha_{2\ (\mathrm{MPa})}$	γ	τ (s)
Ch17-2-6	2.7	7.0	1.8	-3.6	0.85	140
Ch17-2-8L	3.0	9.2	1.6	-5.8	1.02	220
Ch17-2-8R	2.4	8.1	2.1	-2.2	1.05	170
Ch17-2-11	1.4	6.1	1.9	-4.4	0.64	220
Ch17-2-13	3.7	4.8	1.6	-4.7	0.89	190
Ch17-4-2L	3.4	7.8	1.9	-5.8	0.89	260
Ch17-4-3	3.2	6.6	2.1	-2.7	1.07	210
Ch17-4-4	2.8	5.4	2.1	-3.5	1.04	90
Ch17-4-13	2.8	8.4	2.1	-4.1	0.96	190

4. Discussion

In this paper, we present a new method, dynamic micro-fringe projection, to simultaneously determine the viscoelastic and hyperelastic properties of TM. Latex Rubber was used as a standard material to validate the setup. In Fig. 7 it's shown that the mechanical properties determined by the dynamic micro-fringe were slightly higher than that measured from a standard tensile test. At the maximum strain 0.8, the stress determined by dynamic micro-fringe was approximately 7% higher than that measured from tensile test. The difference of the mechanical responses measured from the two method could stem from the difference of the strain rate: in dynamic micro-fringe projection measurement. The loading in the dynamic micro-fringe was applied as pulse within 3 s time span. The strain rate was higher than the tensile test. Despite this difference, the results from the two measurements were nearly identical.

Dynamic micro-fringe projection was also used to measure five chinchilla TMs. It can be noted that, the loadings on the TMs appeared random, though they were all in forms of pulses. In the current setup, the pressures were only applied on the TM without a precise control. The TM under such a forms of pressure were usually ruptured. Thus the pressures dropped down when the leakage occurred. The TM material did exhibit viscoelastic behavior to certain extend. However, the overall mechanical performance of TM was dominated by the hyperelastic effect in such a short period. In this case, even a two-term Prony series was able to describe the viscoelasticity behavior for the TM. The current loading is similar to the blast overpressure applied on the TM but with a relatively longer time span. In the future, more precise control of the pressure (such as creep or periodic pressure loading) will be included in the system to measure the long term effect from the viscoelasticity of the TM.

5. Acknowledgement

We acknowledge the support of DoD W8lXWH-14-1-0228 and NSF CMMI1661246.

6. Reference

[1]. Gan, R.Z., Feng, B., Sun, Q., "Three-dimensional finite element modeling of human ear for sound transmission", Annals of Biomedical Engineering, Vol. 32(6), pp 847-859, 2004.

[2]. Gan, R.Z., Cheng, T., Dai, C., Yang, F., "Finite element modeling of sound transmission with perforations of tympanic membrane", Journal of the Acoustical Society of America, Vol. 126(1), pp 243-353, 2009.

[3]. Daniel, S.J., Funnell, W.R.J., Zeitouni, A.G., Melvin, D., Schloss, M.D, "Clinical application of finite element model of the human middle ear" Journal of Otolaryngology, Vol. 30(6), pp 340-346 , 2001.

[4]. Cheng, T., Dai, C., Gan, R.Z., "Viscoelastic properties of human tympanic membrane", Annals of Biomedical Engineering, Vol. 35(2), pp 305-314, 2006.

[5]. Zhang, X., Gan, R.Z., "Dynamic properties of human tympanic membrane based on frequency-temperature superposition", Annals of Biomedical Engineering, Vol. 41(1), pp 205-214, 2012.

[6]. Yokell, Z., Wang, X., Gan, R.Z., "Dynamic properties of tympanic membrane in a chinchilla otitis media model measured with acoustic loading", Journal of Biomechanical Engineering, Vol. 137(8), pp 61-69, 2015.

[7]. Luo, H., Dai, C., Gan, R.Z., Lu, H., "Measurement of young's modulus of human tympanic membrane at high strain rates", Journal of Biomechanical Engineering, Vol. 131(6), pp 064501, 2009.

[8]. Daphalapurkar, N.P., Dai, C., Gan, R.Z., Lu, H., "Characterization of the linearly viscoelastic behavior of human tympanic membrane by nanoindentation", Journal of Mechanical Behavior of Biomedical Material, Vol. 2(1), pp 82-092, 2009.

[9]. Rohani, S.A., Ghomashchi, S., Agrawal, S.K., Ladak, H.M., "Estimation of the young's modulus of the human pars tensa using in-situ pressurization and inverse finite-element analysis", Hearing Research, Vol. 345, pp 69-78, 2017.

[10]. Liang, J., Fu, B., Luo, H., Nakmali, D., Gan, R.Z., Lu, H. “Characterization the nonlinear elastic behavior of guinea pig tympanic membrane using micro-fringe projection”, International Journal of Experimental and Computational Biomechanics Vol. 3(4), pp 319-344, 2015.
[11]. Liang, J., Luo, H., Yokell, Z., Nakmali. D., Gan, R.Z., Lu, H. “Characterization of the nonlinear elastic behavior of chinchilla tympanic membrane using micro-fringe projection”, Hearing Research,Vol. 339, pp 1-11, 2016.
[12]. Aernouts, J., Dirckx, J.J.J. Static versus dynamic gerbil tympanic membrane elasticity: derivation of the complex modulus. Biomech Model Mechan 11, 829-840, 2012.
[13]. Aernouts, J., Dirckx, J.J.J. Viscoelastic properties of gerbil tympanic membrane at very low frequencies. J Biomech 45, 919-924, 2012.
[14]. Aernouts, J., Aerts, J.R.M., Dirckx, J.J.J. Mechanical properties of human tympanic membrane in the quasi-static regime from in situ point indentation measurements. Hearing Res 290, 45-54, 2012.
[15]. Ghadarghadar, N., Agrawal, S.K., Samani, A., Ladak, H.M. Estimation of the quasi-static Young's modulus of the eardrum using a pressurization technique. Comput Meth Prog Bio 110, 231-239, 2013.
[16]. Simo, J.C., “On fully three-dimensional finite strain viscoelastic damage model: Formulation and computational aspects”, Computer Methods in Applied Mechanical Engineering, Vol. 60(2), pp 153-173,1987.
[17]. Holzpfel, G.A., “On large strain viscoelasticity: continuum formulation and finite element applications to elastomeric structures”, Vol. 39(22), pp 3903-3926, 1996.

Therapeutic Function of Glucagon-like Peptide-1 (GLP-1) for Hearing Restoration after Blast Exposure

Rong Gan[1], Tao Chen[1], Kyle Smith[1], and Shangyuan Jiang[1]
[1]University of Oklahoma, Norman, OK

Introduction: Blast overpressure (BOP) is a high intensity disturbance in the ambient air pressure. When exposed to blast, the human auditory system is vulnerable to both peripheral (middle ear and cochlea) and central damage (brainstem and brain) from the BOP. Repetitive blast exposures, even at a low overpressure level (below mild traumatic brain injury (mTBI)) without rupture of the eardrum, frequently result in permanent hearing damage in Service members. Recent studies have assessed Incretin glucagon-like peptide-1 (GLP-1) receptor agonist (Liraglutide) as a potential treatment strategy for mild to moderate TBI [1, 2]. Published data further indicate that GLP-1R and GLP-1R agonist have functions to mitigate the process of auditory system damage. However, there is no report about the therapeutic function of GLP-1 for blast-induced progressive hearing damage. This paper reports our preliminary study on possible therapeutic function of GLP-1 agonist to the acute and progressive hearing damage in both peripheral and central auditory systems after blast exposure in animal model of chinchilla.

Materials and Methods: Healthy young adult chinchillas were used in this study and divided into three groups (7 animals for each): Exp. Groups 1 and 2 and Control Group. GLP-1R agonist (Liraglutide) was delivered to animals with subcutaneous injection at 48 hours before (named as "pre-treatment") or 2 hours after the blast exposure (named as "post-treatment") within 7 consecutive days in Exp. Groups 1 and 2, respectively. Each animal was exposed to 3 consecutive blast exposures at the BOP level causing mTBI (15-20 psi or 103-138 kPa) on Day 1 after pre-blast function measurements, including the wideband tympanometry (WBT) for middle ear function, auditory brainstem response (ABR) for healing threshold, distortion product otoacoustic emission (DPOAE) for cochlear function, and middle latency responses (MLRs). The MLRs and ABR were measured to reflect the cortex and subcortical hearing function, respectively. All the central auditory function tests were conducted on Days 1 (4 hours after blast), 4, 7, and 14 for both experiment groups. On the final day of completing all the tests, the animals were euthanized and the brain and cochlea were harvested for histology study to determine the neurophysiology and biomarker changes due to the GLP-1R treatment.

Results and Discussion: To verify the GLP-1R expression in auditory system of chinchilla, we did an initial study for the project by using immunohistochemistry technology on the cochlea harvested from a control animal. The results show that GLP-1R (#188605, Abcam) was wildly expressed in chinchilla's cochlea, especially in the spiral ganglion neurons. Then, we further explored that GLP-1R expression was found in the central auditory system. The function tests in two Exp. Groups show that the hearing restoration induced by GLP-1 agonist (Liraglutide) in pre- and post-treatment animals is clearly demonstrated in chinchilla model. For example, animals without GLP-1 treatment and exposure to three times of BOP at the level of equivalent to mTBI resulted in permanent hearing damage with the ABR threshold shift of 20–40 dB over frequencies of 500 Hz – 8 kHz after 14 days of post-blast. For animals with GLP-1 agonist injected at 48 hours before blast exposures, the ABR threshold shift was limited at 7-15 dB over frequencies of 500 Hz – 8 kHz after 14 days of post-blast.

Conclusions: Our preliminary study on therapeutic function of GLP-1R agonist (Liraglutide) for hearing restoration after blast exposure of mild TBI suggests that the repeated exposure-induced hearing damage can be mitigated gradually through 7-14 days of post-blast. However, more future studies on effects of GLP-1 on hearing restoration over time course following blast exposure are needed.

Acknowledgements: This work was supported by DOD W81XWH-14-1-0228.

References:

[1] Li Y, Bader M, Tamargo I, et al. Liraglutide is neurotrophic and neuroprotective in neuronal cultures and mitigates mild traumatic brain injury in mice. J. Neurochemistry, Vol. 135(6): 1203-1217, 2015.
[2] Tweedie D, Rachmany L, Rubovitch V, et al. Blast traumatic brain injury–induced cognitive deficits are attenuated by preinjury or postinjury treatment with the glucagon-like peptide-1 receptor agonist, exendin-4. Alzheimer's & Dementia, Vol. 12(1): 34-48, 2016.

A 3D Printed Ear Model for Standardized Testing of Hearing Protection Devices to Blast Exposure

Marcus Brown[1], Shangyuan Jiang[1], and Rong Gan[1]
[1]University of Oklahoma, Norman, OK

Introduction: Noisy work environments and an increased risk of blast overpressure exposure have caused hearing loss to be a leading disability for veterans [1]. While hearing protection devices (HPDs) are available to military personnel, some troops feel HPDs reduce awareness on the battlefield, and explosive events can happen unexpectedly [1]. This stresses the need for development of HPDs that protect from blast overpressures while allowing the soldier to communicate effectively; however, the lack of a standardized model impedes the development and evaluation of HPDs. While being anatomically accurate, human cadaver ear testing introduces variance among samples due to different ear canal sizes. Dummy models provide a more standard testing platform but lack the accuracy needed to effectively develop HPDs. 3D printing is a method that allows for the repeatable production of highly customizable testing tools. In this study, we utilized 3D printing to create a standardized testing model that was both anatomically accurate and mechanically representative of the ear canal and middle ear. The 3D printed model was validated through experimental tests that exposed the model to blasts and compared the results to tests utilizing human cadaver ears under the same conditions.

Materials and Methods: The 3D printed model included the major structural components of the human outer and middle ear including the ear canal, tympanic membrane (TM), ossicular chain, middle ear suspensory ligaments/muscle tendons, and middle ear cavity. The model was printed using the Stratasys Objet350 Connex3 (Eden Prairie, MN), which has the capability to print multiple acrylic-based polymers with varying mechanical properties. The flexible polymers were used to print the soft tissues of the ear (TM, ligaments, tendons, and canal) and the more rigid materials were used to print the hard tissues of the ear (ossicles and cavity bony wall). The model was then fitted into the same holder used for testing human cadaver ears, placed into a blast chamber, and had a Lyric earplug (Phonak, LLC) inserted into its ear canal. The movement of the earplug was measured using a single-point laser vibrometer (LDV), and pressures were measured at three locations: the entrance of the ear canal (P0), in front of the TM (P1), and in the middle ear cavity. These measurements were recorded as the model was exposed to blasts from an exploding polycarbonate film under pressure from nitrogen gas. The same procedure was repeated with a human cadaver ear in place of the 3D printed model. The results from the two groups was then compared.

Results and Discussion: Table 1 below summarizes the results obtained from blast exposure tests of the 3D printed ear and human cadaver ears. The earplug's movement was similar in both the cadaveric and 3D printed ear canals at 0.25 mm and 0.24 mm, respectively. Both groups also showed a reduction in pressure transmission from the entrance of the ear canal (P0) to in front of the TM (P1). However, earplugs that were inserted into human cadaver ears exhibited a greater attenuation of the blast pressure from P0 to P1 than the earplugs inserted into the 3D printed model. The results showed an average of 16.72 dB drop for the human cadaver ear group while the 3D printed model showed a 9.70 dB drop in sound pressure.

Table 1. Behavior of earplugs in human and 3D printed ears

Sample	P0 (psi)	P1 (psi)	P1/P0	P0-P1 (dB)	ΔD (mm)
4R	10	1.5	0.15	16.48	0.29
5L	7.1	0.8	0.11	18.96	0.16
6R	8.3	1.5	0.18	14.86	0.15
9L	9.5	1.4	0.15	16.63	0.35
10R	8.2	1.2	0.15	16.69	0.28
Mean ± SD	8.6 ±1.15	1.3 ± 0.29	0.15 ± 0.02	16.72 ± 1.46	0.25 ± 0.09
3D Print	5.6	0.6	0.11	9.70	0.24

Conclusions: A standardized 3D printed model was created to mechanically and anatomically represent the human ear for experimental tests. Results showed the 3D printed ear responded similarly to blast overpressures when compared to human cadaver ears verifying that the model can be effective in the improvement of HPDs. Future developments of the 3D printed ear model will further expand its experimental use and its potential as a surgical practice model.

Acknowledgements: Research funded by DOD W81XWH-14-1-0228.

References: [1] Dougherty, A. L. et al., Blast-related ear injuries among U.S. military personnel, J Rehabil Res Dev., 2013, Vol 50: 893-904

Hearing Damage Induced by Blast Overpressure at the Mild TBI Level in a Chinchilla Model

Rong Z. Gan, Tao Chen, and Kyle Smith
School of Aerospace and Mechanical Engineering, University of Oklahoma, Norman, Oklahoma

Background:

Hearing damage is one of the most prevalent injuries in Service members in the battle field. Both the peripheral auditory system (PAS) and various structures within the central auditory system are vulnerable to blast injuries, even blast overpressure (BOP) is at relatively mild TBI level. These injuries could cause long-term hearing disabilities. However, the extent of hearing loss in relation to the number of blast exposure and the time course, and the protective mechanisms of hearing protection devices (HPDs, e.g. earplug) are not well understood. This paper reports our recent study on hearing damage in chinchillas after multiple exposures at the mild TBI level with different number of blasts and post-blast time course. The aim of this study is to determine the auditory system damage due to multiple blast exposures and the protective effects of HPDs on hearing at different BOP levels in a chinchilla model. Knowledge of the hearing damage related to repetitive blast exposure can be used to guide clinical evaluation, rehabilitation, and future research in blast-induced auditory dysfunction.

Methods:

Sixteen chinchillas were included in this study (two controls for histology study). The animals were divided into two groups to expose blast at an average peak pressure of 15-20 psi or 103-138 kPa measured by a pressure sensor positioned at the entrance of the ear canal. The animal was placed inside the test chamber with a compressed nitrogen-driven blast apparatus to create blast overpressure. In all tests, both ears were plugged with a foam earplug to prevent the tympanic membrane from rupturing.

The first group (N=7) were exposed to two consecutive blasts on Day 0, named as 2-Blast group. The second group (N=7) were exposed to three consecutive blasts on Day 0, named as 3-Blast group. The middle ear function, hearing level, and cochlea function were measured using wideband tympanometry (WBT), auditory brainstem response (ABR), and distortion product otoacoustic emission (DPOAE), respectively. Animals of both groups were conducted in all function tests before and after multiple exposures on Day 0 (D0). Then, 2-Blast group were resting for 7 days with function tests on D1, D4 and D7, while the animals in 3-Blast group were resting for 14 days with function tests on D4, D7, and D14. In addition of hearing function tests, the preliminary study on detecting CAS damage in animals were conducted using biochemistry methodologies, such as the immunohistochemically (IHC) staining and the immunofluorescence staining on chinchilla brain sections.

Results:

● Hearing damage in relation to number of blast exposure: In 2-Blast group, there was a huge increase of ABR threshold on D0, particularly at higher frequencies (f>2 kHz). Following this greatest threshold increase, the ABR threshold decreased on each tested day. On D7, the threshold was almost the same as the pre-blast on D0. The results of ABR threshold shift during the time course from D0 to D7 indicate a large shift decrease on D4, and an insignificant shift on D7. In 3-Blast group, there was a greater increase of post-blast on D0 than that of 2-Blast group. Following the greatest threshold increase on D0, the ABR threshold decreased on each tested day, but it was almost stable after the large decrease on D4. The ABR threshold shift during the time course from D0 to D14 shows that after the large shift decrease on D4, each subsequent shift decreased less and there was little difference in threshold shifts between D4, D7, and D14. On Day14, there were an ABR threshold shift of 20 dB at 500 Hz and 40 dB at 8 kHz, which reflects the permanent hearing damage after 14 days in 3-Blast group.

● DPOAE decrease in relation to number of blast exposure: DPOAE decrease represents the cochlear outer hair cell function change. In 2-Blast group, the DPOAE level was decreased from pre- to post-blast on D0, then the level had a big increase on D1 across the frequencies and a continual increase on D4 at high frequencies. On D4 and D7, the DPOAE level came back to the pre-blast. The greatest DPOAE level shift occurred on D0 after blast and an insignificant shift appeared on D4 and D7. In 3-Blast group, the DPOAE level was greatly decreased from pre- to post-blast on D0, then the level had an obvious increase on D4 across the frequencies. There was no much difference between D4 and D7 and the level had a continual increase on D14. The DPOAE level shift did not come to the normal after 14 days and there was 14 dB shift at 1 kHz and 28 dB at 11-12 kHz. There was no obvious difference on DPOAE recovery between 4D, 7D, and 14D.

● <u>CAS damage in relation to number of blast exposure</u>: Both Hoechst staining and immunofluorescence staining of PI3K protein were perform in chinchilla auditory cortex in control, 2-Blast, and 3-Blast animals. The preliminary results demonstrate that the auditory cortex neurons are damaged after multiple blast exposures and result in neuron cells apoptosis through reducing the expression of PI3K. We will work on more biomarkers of the PI3K/AKT signal pathway in future studies.

Conclusions:

Two groups of chinchillas' hearing damage in relation to the number of blast exposure at the mild TBI level (15-20 psi BOP) were tested in animals with both ears protected (foam earplugs). After the initial blasts, both groups had elevated ABR thresholds and decreased DPOAE levels, which translated into large threshold and level shifts. During the time course, the ABR and DPOAE shifts both decreased. After 7 days, the 2-Blast group's threshold shifts had almost reached zero, indicating the ABR and DPOAE levels had returned to normal. The return to the baseline indicates no permanent damage was sustained to either the auditory system (ABR) nor the cochlear response (DPOAE). After 14 days, the 3-Blast group's ABR and DPOAE shifts remained elevated by 26 and 23 dB, respectively. The greatest recovery of ABR threshold and DPOAE shift was on the Day 4 and after D4, each day only had minimal improvement. Even if a longer time course was chosen to evaluate the ABR and DPOAE levels, the rate of improvement after D4 suggests the shifts would remain similar to those found on D4. The auditory response and cochlear response have been permanently damaged. (Supported by DOD W81XWH-14-1-0228)

Learning Objectives:

1) Describe a blast model in chinchillas to measure hearing damage induced by blast exposure at the mild TBI level

2) Define the methods for measuring hearing threshold change (ABR) and cochlear outer hair cell damage (DPOAE)

3) Introduce the time course study to determine whether the hearing damage is permanent or temporary

----

Introduce the HPDs (e.g. earplugs) testing in animals under blast exposure at the mild TBI level

**** Use action verbs such as Describe, Define, Analyze to begin the description of each learning objective. A learning objective is one sentence. ****

Central and Peripheral Auditory Abnormalities in Animal Models of Blast-Injury

Namas Chandra[1], Ningning Shao[1], Kakulavarapu V. Rama Rao[1], Shangyuan Jiang[2], Tao Chen[2], Marcus Brown[2], and Rong Z. Gan[2]
[1]Center for Injury Biomechanics, Materials, and Medicine, Department of Biomedical Engineering, New Jersey Institute of Technology, Newark, NJ

[2]School of Aerospace & Mechanical Engineering, University of Oklahoma, Norman, OK

Background

Blast-related injuries are the most common occurrences in soldiers in combat operations that not only cause traumatic brain injury, but also induce auditory damage including tinnitus and hearing loss. These auditory abnormalities following blast result from extremely loud noises generated due to wild explosions created by the blast. About 67% of blast-exposed individuals develop mild to moderate hearing impairments as well as 56% of combat veterans develop tinnitus. Tinnitus, a ringing in the ear or head without an external sound source, is a prevalent health problem and it is often associated with inability cope up with irritable reactions of constant ringing in the ear which frequently leads to a number of limbic disorders such as anxiety, sleep disturbance, and emotional distress. Several studies investigated middle and inner ear injuries including perforation of tympanic membrane, dislocation or fracture of ossicular chain, and gross trauma in cochlea such as rupture of basilar membrane and permanent loss of hair cells in blast-induced hearing loss.

While peripheral auditory abnormalities have been largely investigated to understand the mechanism of hearing loss in blast-related traumatic injuries, the central nervous system associated derangements that functionally contribute to hearing loss have not been well studied. There are two main central auditory pathways that regulate the hearing process namely the auditory cortex and the inferior colliculus. The dorsal cochlear nucleus (DCN), a cortex-like structure present in dorsal side of the brain stem area is where the auditory nerve fibers from the cochlear area form synapses and conduct the neuronal impulses from the inner ear to the central nervous system. Any derangement in the central auditory pathways involving auditory cortex and inferior colliculus results in an excessive firing of sensory neurons in these regions which not only leads to disturbances in the relay of hearing process but also incur secondary manifestations including changes in mood and behavior. We therefore hypothesize that hearing impairments associated with blast injury alter the CNS auditory pathways involving auditory cortex and inferior colliculus areas of the brain.

Studies on noise-induced hearing loss models that experimentally induce high intensity noise for a prolonged period of time revealed significant aberrations in excitatory and inhibitory neurotransmission ratio (E/I ratio) in animals subjected to the high intensity noise. The present study, therefore investigated potential alterations in glutamate and GABA receptor ratio as a measure of excitatory and inhibitory neuronal outputs that contribute to neuronal excitability in blast-induced hearing impairments.

Methods:

Adult 10-week old Sprague-Dawley rats and adult chinchillas (2 years old**)** were subjected to mild and moderate shock wave of (25 and 35 psi). The Neurological Severity Score (NSS) was assessed five minutes post exposure and none of the animals included in this study displayed scores that differed from control animals. **4h and 24 h** (4h for chinchilla) following blast exposure animals were euthanized and transcardially perfused (with PBS) and fixed with 4% paraformaldehyde. In order to evaluate changes in neurotransmitter receptor densities immunofluorescence studies were conducted for NMDA-R1 (excitatory glutamate receptor) and GABA$_A$ (inhibitory neurotransmitter receptor) in auditory cortex and inferior colliculus regions of the brain. Briefly, tissue sections (20 μm thick) were fixed in ice-cold methanol

(100%) solution for 10 minutes at –20 °C, blocked in 10% Donkey serum at room temperature for 1 hour in PBS containing 0.03% Triton X-100. Fixed tissues were incubated overnight at 4 °C with respective primary antibodies to NMDA-R1 (Rabbit polyclonal, Sigma-Aldrich, 1:400) and GABAA (Mouse monoclonal, Abcam, 1:100). Immunofluorescence was performed using Alexafluor 488 for both NMDA and GABAA receptors separately. Following immunostaining, slides were digitized (20x magnification) using Leica Aperio Versa 200 fluorescent microscope and slide scanner. Fluorescence intensities in auditory cortex and inferior colliculus were quantitated using AreaQuant software (Leica Biosystems) and expressed as average fluorescence intensity/unit area.

In both rats and chinchillas, one ear was inserted with a foam earplug and another ear was left open. The tympanic membrane (TM) in each ear was examined with a surgical microscope before and after the blast exposure. In chinchillas, the middle ear function, hearing level, and cochlea function were measured using wideband tympanometry (WBT), auditory brainstem response (ABR), and distortion product otoacoustic emissions (DPOAEs), respectively before and after blast exposure. Upon the completion of all function tests, the animal was euthanized and the brain and cochlea were harvested for immunohistochemistry and scanning electron microscopy (SEM) studies, respectively. Standard SEM preparation of cochlear hair cells' images were performed and samples were imaged using scanning electron microscope (JEOL 840a and Zeiss NEON).

Results

Based on immunofluorescence studies of NMDA-R1 and GABAA receptor protein levels we observed that the levels of GABAA receptor were significantly increased in both auditory cortex and inferior colliculus in both rat and chinchilla brain, while we also observed a subsequent decrease in NMDA-R1 receptor densities.

Otoscopic photographs of TM showed that the TM was ruptured in all open ears after blast exposure, but remained intact in the protected ears. This indicated the protective function of the earplug from mechanical damage on the TM. The SEM images of cochlear hair cells after blast showed the damage to the hair cells including the hair cell loss and the stereocilia disrupted. The hearing damage (e.g. ABR threshold elevation and DPOAE reduction) was found in both open and protected ears with a correlation to blast intensity. The blast-induced peripheral auditory changes were consistent with the findings observed from immunofluorescence studies in central auditory system.

Conclusions

Our studies strongly indicate that both peripheral and central mechanisms contribute to the blast-induced hearing loss and among these, an imbalance of the excitatory and inhibitory neurotransmitter mechanisms play a major role in the propagation and contribute to the pathophysiology of blast-induced hearing loss. This study indicates that the effects of blast wave can affect central and peripheral system independently and collectively and need to be studied as a comprehensive system to understand and treat hearing loss in service members during training and in combat.

Dual-Laser Measurement and Finite Element Modeling of Human Tympanic Membrane Motion under Blast Exposure

Rong Z. Gan, Shangyuan Jiang, and Kyle Smith
School of Aerospace and Mechanical Engineering, University of Oklahoma, Norman, Oklahoma

Introduction: Hearing damage is one of most prevalent injuries in military personnel and civilians when exposed to blast exposure or high intensity noise. Perforation of the tympanic membrane (TM) is the most noticeable injury observed after a blast exposure. However, the mechanism of how the blast overpressure wave interact the TM and impair the peripheral auditory system is not well understood. This paper reports the first ever approach using two laser Doppler vibrometers (LDVs) to measure the motion of the TM when the ear was exposed to blast. Realtime movement of the TM under blast was captured and calculated from the finite element (FE) model of the human ear developed in our lab for simulation of blast overpressure transduction.

Methods: Five fresh human temporal bones (TBs) were involved in this study. The TB was mounted to a "head block" with a pressure sensor P1 fixed near the TM in the canal. The head block was then placed under a compressed nitrogen-driven blast apparatus inside the anechoic chamber in our lab. Another pressure sensor P0 was placed at the entrance of the ear canal to monitor the pressure reaching the ear. A scanning LDV and a single beam LDV were focused on the TM and the head block, respectively. The velocities of the TM and head block were recorded simultaneously as the blast wave was recorded by the pressure sensors. The exact motion of the TM under blast was calculated by subtracting the head block movement from the membrane movement. The TM motion was then compared with that calculated from the 3D FE model of the human ear.

Results: Experimental results include the measured P0, P1, and velocity or displacement (converted from velocity) data. The mean and SD values measured from five TBs with two LDVs at P0 level around 34 kPa or 5 psi include: the velocity difference ΔV of 12.62 ± 3.63 m/s and displacement difference ΔD of 0.78 ± 0.26 mm. The peak-to-peak displacement normalized by peak P0 pressure was 22.9 ± 6.6 μm/kPa. The frequency domain analysis indicated that the spectrum peak was located at 2-3 kHz and velocity amplitude varied from 0.51 to 1.4 m/s. The FE model-derived TM displacements under blast overpressure were consistent with the experimental results.

Conclusions: The TM movement under blast overpressure has been successfully measured using dual-LDV setup. The experimental data show the response of human TM to blast waves and provide a better understanding of acoustic damage in the TM or middle ear by blast. The consistency between experimental data and FE model-predicted results has validated the model for future study on mechanisms of the tearing or rupturing process of the TM in response to blast overpressure.

Acknowledgements: This work was supported by the US DOD grant W81XWH-14-1-0228.

Central and Peripheral Auditory Injuries in Animal Models after Blast Exposure

Namas Chandra[1], Ningning Shao[1], Kakulavarapu V. Rama Rao[1], Shangyuan Jiang[2], Tao Chen[2], Marcus Brown[2], and Rong Z. Gan[2]
[1]Center for Injury Biomechanics, Materials, and Medicine, Department of Biomedical Engineering, New Jersey Institute of Technology, Newark, NJ

[2]School of Aerospace & Mechanical Engineering, University of Oklahoma, Norman, OK

Introduction:

Blast-related injuries are commonly encountered by soldiers in combat operations leading to traumatic brain injury; further, they also induce auditory damage including tinnitus and hearing loss. About 67% of blast-exposed soldiers develop mild to moderate hearing impairments and about 56% of combat veterans develop tinnitus. Tinnitus, a ringing in the ear or head without an external sound source is a prevalent health problem which frequently leads to a number of limbic disorders such as anxiety, sleep disturbance, and emotional distress. Several studies investigated middle and inner ear injuries including perforation of tympanic membrane, dislocation or fracture of ossicular chain, and gross trauma in cochlea such as rupture of basilar membrane and permanent loss of hair cells. While peripheral auditory abnormalities have been largely investigated to understand the mechanism of hearing loss in blast-related traumatic injuries, the central nervous system associated derangements that functionally contribute to hearing loss have not been well studied. The main circuitry pathway for central auditory perception includes the dorsal cochlear nucleus (DCN), a cortex-like structure present in dorsal side of the brain stem area where the auditory nerve fibers from the cochlear area form synapses and convey the neuronal impulses from the inner ear to the central nervous system. Several studies using high intensity noise-induced hearing loss in rat and chinchilla models revealed oxidative stress and an imbalance of excitatory and inhibitory neurotransmission in in central auditory areas. We hypothesize that blast induced hearing loss/tinnitus involves both peripheral and central auditory disturbances; they not only contribute to hearing loss but also initiate secondary effects leading to changes in mood and behavior.

Methods and Results:

Both adult male 10 week old Sparague Dawley rats and chinchillas (2 year old) were exposed to blast loading at mild and moderate blast over pressures (15-25 psi). During the blast exposure one ear of the animal was inserted with a foam earplug and another ear was left open. 24 h and 7 days following blast exposure animals were euthanized and the brain and cochlea were harvested for immunohistochemistry and cochlear hair cells' images were collected using scanning electron microscope. Thin sections (25 µm) of different brain regions were prepared using vibratome and sections were probed for the protein levels of NMDA-R1 a glutamate receptor and GABAA an inhibitory neurotransmitter receptor in both auditory cortex and inferior colliculus by immunofluorescent staining. Otoscopic photographs of tympanic membrane (TM) showed that the TM was ruptured in all open ears after blast exposure but remained intact in the protected ears indicating that earplug protects from mechanical damage of the TM. The SEM images of cochlear hair cells after blast showed the damage to the hair cells including the hair cell loss and the stereocilia disrupted. The hearing damage (e.g. ABR threshold elevation and DPOAE reduction) was found in both open and protected ears with a correlation to blast intensity. The blast-induced peripheral auditory changes were consistent with the findings observed from immunofluorescence studies in central auditory system. Immunofluorescence analysis of neurotransmitter receptors densities showed a significant decrease in GABAA receptor and a subsequent increase in NMDA-R1 receptors in these animals.

Conclusions:

Our studies indicate that the effects of blast wave can affect central and peripheral system independently and collectively and the central auditory defects arise due to an imbalance of the excitatory and inhibitory neurotransmitter mechanisms.

Progressive Hearing Damage after Repeated Exposure to Low Level of Blast Overpressure in Chinchillas

[1,2] Tao Chen, [1]Kyle Smith, [1]Shangyuan Jiang,[2] Tianyu Zhang, and [1]Rong Z. Gan
[1]*University of Oklahoma, OK*
[2]*Eye & ENT Hospital of Fudan University, Shanghai*

Introduction

Hearing damage caused by blast waves is a frequent and common injury for Service members. However, most studies have focused on acute hearing damage caused by blast overpressure (BOP) at high levels equivalent to the mild or moderate traumatic brain injury (TBI). Fewer animal studies have investigated the progressive hearing loss after repeated exposure to the BOP blow the mild TBI. In this paper, we report our recent study in chinchillas to measure the changes of middle ear function, hearing threshold, and central auditory system response during the time course under repeated low intensity blast exposures. Our goal is to determine whether repeated low BOP exposures are the cause of progressive hearing damage and to evaluate the protective mechanism of hearing protection devices (e.g. earplug).

Methods

Two groups of chinchillas (N=7 each) were used in this study. Animals in Group 1 and 2 were tested at low blast overpressure (21-35 kPa or 3-5 psi). The pressure at the entrance of the ear canal (P0) and the pressure in the ear canal near the TM (P1) in the ears with and without earplug were measured in Group 1. The animals in Group 2 were blasted three times on Day 1 with 10 minutes interval between blasts. One ear was left open and another ear was protected with an earplug. Before and after blasts, the middle ear function, hearing level, and central auditory function were measured using wideband tympanometry, auditory brainstem response (ABR), and middle latency responses (MLRs) . Animals survived for 7 days, and their hearing functions were measured on Day 4 and Day 7, respectively.

Results and Discussion

In Group 1, the blast pressure was attenuated from 30 kPa or 4.5 psi (P0) to 3 kPa or 0.45 psi (P1) in the ears with earplug. The blast pressure increased from 35 kPa or 5 psi (P0) to 48 kPa or 7 psi (P1) in the open ears without earplug. In Group 2, hearing damage in open ears after blast exposures were observed by the ABR shifts, the decrease of average value of MLR Pa wave amplitude, and the increase of Pa latency. For protected ears, hearing damage after blasts was also observed, but at a much low level. On Day 4, there was an improvement of ABR and MLR values in the protected ears. On Day 7, the protected ears were recovered and the hearing damage in open ears remained.

Conclusion

Repeated exposures at low BOP level can damage the peripheral and central auditory system. ABR thresholds were significantly elevated and Pa amplitude of the MLR was largely reduced in open ears on Day 7 after repeated low blast exposures. The difference of the hearing level restored in the protected ears from that of the open ears shows the significance of hearing protection and recovery process. (Supported by US DOD W81XWH-14-1-0228)

SEM Imaging of Cochlear Hair Cell Damage Caused by Blast Exposure

Marcus Brown, Tao Chen, Rong Z. Gan
School of Aerospace and Mechanical Engineering
University of Oklahoma, Norman, Oklahoma

Introduction: Exposure to blast overpressure (BOP) causes hearing loss by applying intense sound pressure to the ear, which can rupture the tympanic membrane and reduce the number of viable cochlear hair cells. While damaged hair cells can self-repair, studies have shown that stereocilia of mammalian hair cells do not easily self-repair or regenerate after experiencing acoustic trauma, which can lead to prolonged hearing loss (S. Jia et al., 2009). Scanning electron microscopy (SEM) has been used as a powerful tool to image hair cell damage induced by noise exposure. However, there is a lack of reports on the hair cell damage caused at different BOP levels, and how the BOP exposure relates to the damage variation from the basal turn to the apex of the cochlea. In this study, we utilized SEM to observe the damage to chinchilla's hair cell stereocilia after the animal was exposed to one of three BOP levels ranging from below mild traumatic brain injury (TBI), mild and moderate TBI levels. We aim to understand the extent of auditory injury at different TBI levels and the resulting degree of cochlear hair cell damage.

Materials and Methods: Four groups of chinchillas (two for each) were used in this study with one group as control and three groups being exposed to blast (one ear plugged) at three BOP levels: 1.2–3.6 psi, 6–9 psi, and 22–35 psi. The animal was euthanized after the exposure and the cochlea was immediately harvested. The cochlea sample was then fixated overnight in 4% paraformaldehyde with 0.1M phosphate buffer saline (PBS) solution containing 5% sucrose, decalcified with 0.5M ethylenediaminetetraacetic acid in PBS for seven days, and microdissected for a post-fixation with 1% OsO_4 for 30 min. Samples were then dehydrated in ethanol, critical point dried with CO_2, sputter coated with gold/palladium, and examined with an electron microscope.

Results and Discussion: Results from SEM images showed that stereocilia of the outer hair cells were significantly damaged from the blast waves experienced. Most of the damage was observed in the basal turn of the cochlea. Higher BOP levels showed an increased disruption and damage to the stereocilia (Figure 1). The damage observed in cochlear hair cells was in agreement with the hearing function tests in chinchillas that were exposed to the same BOP levels. (Supported by DOD W81XWH-14-1-0228)

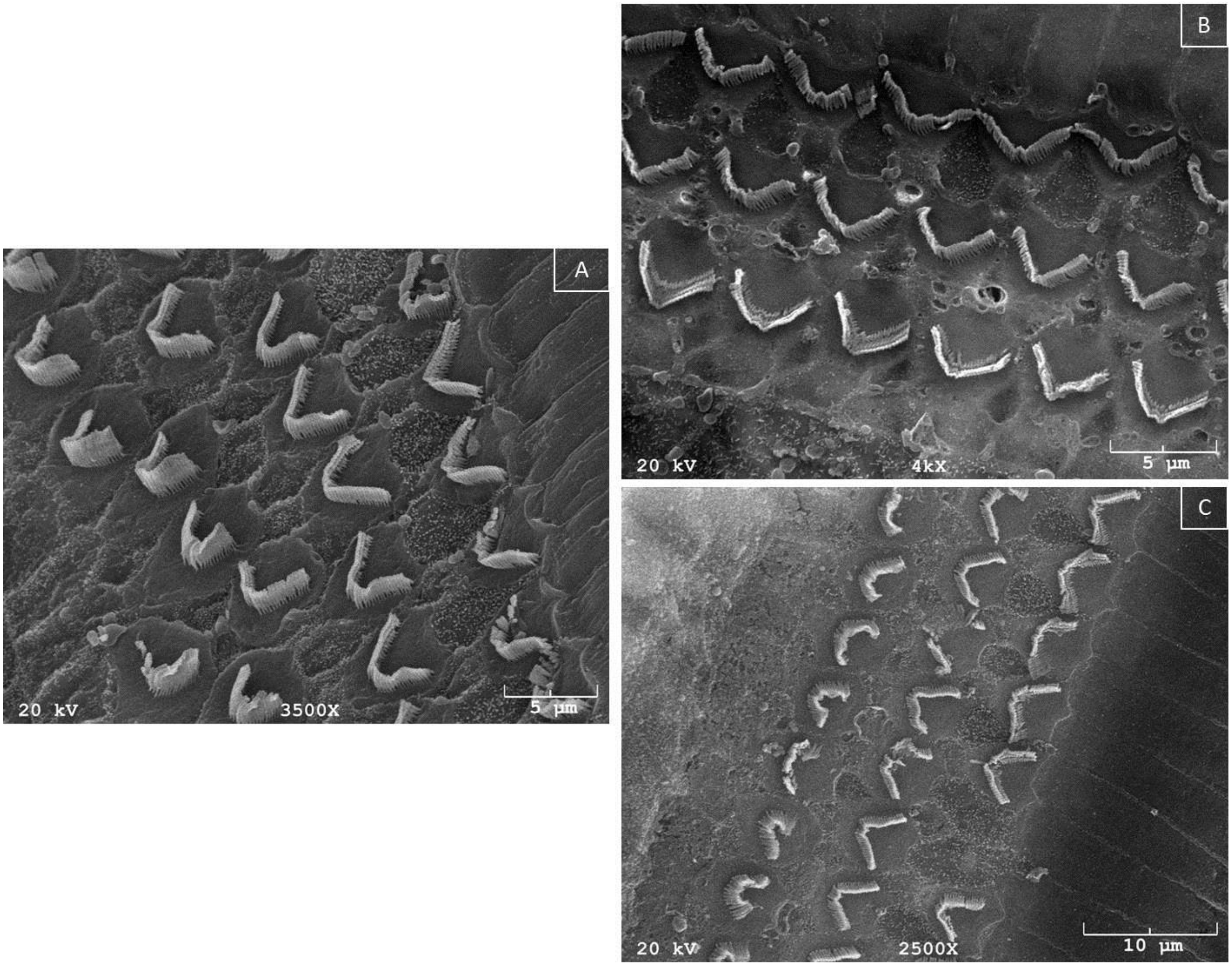

Figure 1: SEM images of the outer hair cells' stereocilia in the basal turn after blast exposure. The lowest pressure range of 1.8–3.6 psi (A) exhibited the least amount of damage and disturbance to the stereocilia bundles. The middle pressure range of 6–9 psi (B) showed an increase of damage while the highest pressure range of 22–35 psi (C) had the highest amount of damage to the stereocilia.

Progressive Hearing Damage after Exposure to Multiple Blasts in Chinchillas

Tao Chen, Kyle Smith, and Rong Gan
University of Oklahoma

Introduction

Hearing damage caused by blast waves is a frequent and common injury for Service members. A significant fraction of veterans suffers from long-term hearing disabilities. However, the extent of hearing loss or permanent hearing damage in relation to the number of blasts and the time interval between each blast has not been investigated. In this paper, we report our recent study in chinchillas to evaluate the middle ear function, hearing threshold, and cochlear response during the time course of hearing damage. Our goal is to determine whether multiple exposures to blast waves is the cause of progressive hearing damage and to evaluate the protective mechanism of hearing protection devices (e.g. earplug) for multiple exposures.

Methods

Two groups of chinchillas (N=10 each) were used in this study. One ear was left open and another ear was protected with an earplug. Animals in Group 1 and Group 2 were tested at low blast overpressure (3-5 psi) and the mild blast overpressure (12-15 psi), respectively. The animals were blasted twice on Day 1 with one hour interval between blasts. Before the first and after each blast, the cochlea and middle ear functions were measured using ABR, DPOAE, and wideband tympanometry. Animals recovered until Day 7, and their hearing functions were measured on Day 4 and Day 7, respectively.

Results and Discussion

In Group 1, for open ears, hearing damage accumulated after the first and second blast was observed by the ABR and DPOAE shifts. For protected ears, hearing damage after each blast was still accumulated, but at a much low level. On Day 4, there was some improvement in both ears. On Day 7 the protected ears fully recovered and the open ears almost recovered. In Group 2, the hearing damage after each blast was greater than that of Group 1. On Day 4 there was slight improvement in hearing and on Day 7 the hearing was further improved.

Conclusion

Multiple blast exposures can aggravate hearing loss. ABR thresholds were significantly elevated and DPOAE levels were largely reduced after the first and second blast. The ABR threshold and DPOAE level shift values were reduced in protected ears, especially at low frequencies. The difference of the hearing level restored in the protected ears from that of the open ears shows the significance of hearing protection and recovery process. (Supported by DOD W81XWH-14-1-0228)

Biomechanical Modeling and Measurement of Blast Injury and Hearing Protection Mechanisms

ERMS# 13063031 Task Title: Measuring and modeling of blast wave transduction through the ear canal
Award Number: W81XWH-14-1-0228
PI: Rong Z. Gan, Ph.D. **Org:** University of Oklahoma **Award Amount:** $2,521,486

Study/Product Aim(s)

- Quantify middle ear injury in relation to blast pressure level and wave direction and overpressure transduction through the ear
- Identify middle ear protection mechanisms by detecting middle ear muscle reflex and measuring mechanical changes of ear tissues
- Develop the FE model of human ear to predict unwarned and warned responses of the middle ear to blast exposure

Approach

- Identify blast-induced eardrum and middle ear damage and the blast pressure transmission through the ear with multiple sensors inserted in cadaver ears
- Detect the acoustic reflex on EMG of middle ear stapedius muscle
- Measure mechanical properties of ear tissues after blast exposure
- Conduct nonlinear FE analysis on 3D FE model of the human ear – passive and active ear models in CFX/ANSYS
- Simulate the HPDs in FE model to derive prevention mechanisms

SEM Images of Cochlear Hair Cells after Blast Exposure

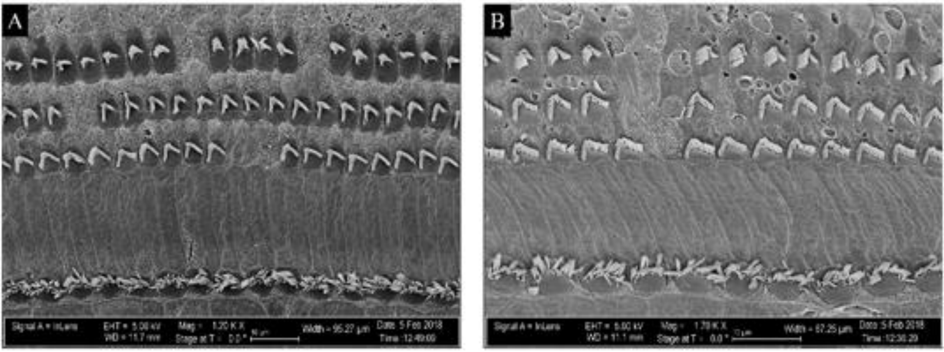

SEM images of outer (top 3 lines) and inner (bottom line) hair cells. ***A.*** *Apex;* ***B.*** *Middle turn.*

Accomplishment: 1) Dual-laser measurement and FE modeling of human eardrum motion under blast exposure; 2) hearing damage in relation to repeated blast exposure over the time course in chinchillas; 3) correlation of central and peripheral auditory system damages induced by blast; 4) 3D FE model of the ear for modeling blast waves transduction from the ear canal to cochlea; 5) 3D printed human ear for testing of HPDs to blast exposure.

Timeline and Cost

Activities CY	**15**	**16**	**17**	**18**
Tasks 1-1 and 1-2 (Blast injury)	🟪	🟪	🟪	
Task 2-1 (Acoustic reflex-EMG)	🟪	🟪	🟪	
Task 2-2 (Tissue mechanics)	🟩	🟩	🟩	🟩
Tasks 3-1, 3-2, and 3-3 (FE modeling of blast injury)	🟩	🟩	🟩	🟩
Estimated Budget ($K)	**$619**	**$623**	**$641**	**$638**

Updated: October 29, 2018

Goals/Milestones

CY15 Goals – Establish measurement and modeling of blast overpressure

☑ Identify eardrum/middle ear damage thresholds and setup EMG measurement and tissue mechanical testing

☑ Building passive FE model of the ear for analysis of blast wave

CY16 Goals – Characterization of middle ear function

☐ Investigate ear canal/middle ear transfer function and muscle function

☐ Continue tissue mechanical testing and validate the passive FE model

CY17 Goals – Middle ear protection mechanisms and active model

☐ Complete muscle function test and continue tissue mechanical tests

☐ Develop active FE model of the model for blast wave analysis

CY18 Goals – Validate active FE model with applications

☐ Complete nonlinear active model and ear tissue testing

☐ Evaluate HPDs in FE model of the ear for hearing protection

Comments/Challenges/Issues/Concerns

- EMG measurement in animals and blast test in cadaver ears began.

Budget Expenditure to Date

Projected Expenditure: $2,521,486.30
Actual Expenditure: $1,754,779.41 (approximate)